Nour-el-hana Abbassi

Biochemical and structural characterizations of the catalytic subunit of Elongator complex

Supervisor: Dr hab. Sebastian Glatt

Doctoral Thesis

Max Planck Laboratory

Malopolska Centre of Biotechnology

Jagiellonian University Krakow

Krakow, 2023

"Without the spirit's inquiry, where would we be?

Such is the beauty and nobleness of science:

a boundless desire to push back the frontiers of knowledge,

to pursue the secrets of matter and life with no preconceptions of the potential consequences"

Marie Salomea Skłodowska–Curie

Abstract in English

Transfer RNAs (tRNA) are essential elements for cellular protein synthesis. It is an adaptor that decodes mRNA codons and forms the nascent poly-peptide chain in the ribosome during translation. tRNA, like every RNA, consists of four simple nucleotides, namely adenosine, uridine, cytosine, and guanine. These building blocks can be further decorated with various modifications to either maintain structure plasticity or expand the decoding ability. Nucleotides of the anticodon stem loop, which recognize the mRNA codons, are heavily modified. The modification of uridines at position 34 involves multiple enzymes. The Elongator complex is responsible for the first step, which converts U_{34} to cm^5U_{34}. This macromolecular complex contains two copies of its six Elongator proteins (Elp) – Elp1, Elp2 and Elp3 (Elp123) form the enzymatically active subcomplex and Elp4, Elp5 and Elp6 constitute the second subcomplex. The interaction between the two subcomplexes is dynamic and their interplay still needs to be fully understood. All complex components are conserved in eukaryotes, while Elp3 is also found in archaea as well as in some bacteria and viruses. Elp3 is the catalytic center and contains two catalytic domains, namely a lysine-acetyltransferase domain (KAT) and a radical S-adenosyl-methionine domain (rSAM). Little is known about the Elp3-mediated catalytic reaction and its regulation in higher eukaryotes. The goal of this thesis is to comprehensively investigate the biophysical, biochemical, and structural features of the human ELP123 (*Hs*ELP123) subcomplex. First, I used a purified archaeal Elp3 protein as a model enzyme for characterizing basic features and activities. Second, I managed to purify the *Hs*ELP123 subcomplex from an insect cell expression system and investigated its properties *in vitro*, including its tRNA binding, its tRNA-triggered acetyl-CoA (ACO) hydrolysis and its interaction with *Hs*ELP456. Third, I acquired several cryo-EM datasets for *Hs*ELP123-tRNA complexes in the presence of ACO analogues and reconstructed cryo-EM electron density map at high resolution. In summary, my results confirmed that the activities of Elongator are highly conserved from archaea to humans. The data provide solid evidence that the interaction between *Hs*ELP123 and substrate tRNAs is highly complex, involving several steps and conformational rearrangements of ELP1 and ELP3. More importantly, I show that the invariable tRNA position 33 (U_{33}), and not the modified U_{34} base, is the determinant to trigger ACO hydrolysis in ELP3. Finally, my detailed *in vitro* analyses explain the impacts of clinically relevant mutations in ELP1 and ELP3. In summary, my work presents a new layer of understanding the *Hs*ELP123 subcomplex in the related diseases, like neurodegenerative disorders or cancers.

Abstrakt po polsku

Transportujące RNA (tRNA) jest niezbędnym elementem podczas syntezy białek w komórce. Jest to cząsteczka, która jednocześnie dekoduje kodony mRNA i tworzy powstający łańcuch polipeptydowy w rybosomie podczas translacji. tRNA, jak każdy RNA, składa się z czterech prostych nukleotydów: adenozyny, urydyny, cytozyny i guaniny. Te elementy budulcowe mogą być dodatkowo ozdobione różnymi modyfikacjami, które zapewniają utrzymanie plastyczności struktury lub mogą rozszerzać zdolność dekodowania. Nukleotydy w pętli ramienia antykodonowego, które rozpoznaje kodony mRNA, są silnie zmodyfikowane. W modyfikację urydyn w pozycji 34 zaangażowanych jest wiele enzymów. Za pierwszy etap, który przekształca U_{34} w cm^5U_{34}, odpowiada kompleks Elongator. Ten wielkocząsteczkowy kompleks zawiera dwie kopie sześciu podjednostek Elongatora (Elp) - Elp1, Elp2 i Elp3 tworzą aktywny enzymatycznie podkompleks, a Elp4, Elp5 i Elp6 stanowią drugi podkompleks. Charakterystyka oddziaływań zachodzących pomiędzy powyższymi podkompleksami nie została jeszcze w pełni opisana, jednak wiadomo, że dochodzi tam do dynamicznych zmian. Wszystkie podjednostki kompleksu są zachowane u eukariontów, natomiast Elp3 występuje również u archeonów, a także u niektórych bakterii i wirusów. Podjednostka Elp3 jest centrum katalitycznym i zawiera dwie domeny katalityczne - domenę acetylotransferazy lizyny (KAT) i domenę rodnikową S-adenozylo-metioniny (rSAM). Niewiele wiadomo o katalizowanej przez Elp3 reakcji i jej regulacji u wyższych eukariontów. Celem tej pracy jest wszechstronne zbadanie biofizycznych, biochemicznych i strukturalnych cech ludzkiego podkompleksu ELP123 (*Hs*ELP123). Po pierwsze, wykorzystałam oczyszczone białko Elp3 pochodzenia archeowego do scharakteryzowania podstawowych cech i właściwości enzymu. Po drugie, udało mi się oczyścić podkompleks *Hs*ELP123 wyprodukowany wykorzystując ekspresję białek w komórkach owadzich i zbadać jego właściwości *in vitro*, w tym wiązanie tRNA, hydrolizę acetylo-CoA (ACO) wyzwalaną przez tRNA oraz interakcję z *Hs*ELP456. Po trzecie, pozyskałam kilka zestawów danych kriogenicznej mikroskopii elektronowej (cryo-EM) kompleksów *Hs*ELP123-tRNA w obecności analogów ACO. Z zebranych danych zrekonstruowałam mapę cryo-EM o wysokiej rozdzielczości. Podsumowując, moje wyniki potwierdziły, że aktywność kompleksu Elongator jest wysoce konserwatywna u archeonów i u ludzi. Otrzymane wyniki pokazują, że oddziaływanie pomiędzy *Hs*ELP123 a substratowym tRNA jest złożone, obejmujące kilka etapów i rearanżacje konformacyjne podjednostek ELP1 i ELP3. Co ważniejsze, pokazuję, że niezmienna pozycja tRNA 33 (U_{33}), a nie zmodyfikowana baza U34, jest czynnikiem decydującym o uruchomieniu hydrolizy ACO w Elp3. Na koniec, szczegółowe analizy *in vitro* wyjaśniają wpływ klinicznie istotnych mutacji w Elp1 i Elp3. Podsumowując, moja praca przedstawia nowy poziom zrozumienia działania podkompleksu *Hs*ELP123 w powiązanych z nim chorobach, takich jak zaburzenia neurodegeneracyjne czy nowotwory.

Table of contents

List of publications:

Partial results of the PhD Thesis are published in:

1. Lin TY, **Abbassi NEH**, Zakrzewski K, Chramiec-Głąbik A, Jemioła-Rzemińska M, Różycki J, Glatt S.; The Elongator subunit Elp3 is a non-canonical tRNA acetyltransferase. *Nat Commun. 2019.* DOI :10.3390/ijms21218209

2. Kojic M[#], **Abbassi NEH[#]**, Lin TY, Jones A, Wakeling EL, Clement E, Nakou V, Kaliakatsos M, Glatt S, Wainwright BJ. A novel ELP1 mutation impairs the function of the Elongator complex and causes a severe neurodevelopmental phenotype. *J Hum Genet. 2023.* ([#]these authors contributed equally). DOI: 10.1038/s10038-023-01135-3

Other publications:

1. Dauden MI, Jaciuk M, Weis F, Lin TY, Kleindienst C, **Abbassi NEH**, Khatter H, Krutyhołowa R, Breunig KD, Kosinski J, Müller CW, Glatt S.; Molecular basis of tRNA recognition by the Elongator complex. *Sci Adv 2019.* DOI: 10.1126/sciadv.aaw2326

2. **Abbassi NEH**, Biela A, Glatt S., Lin TY.; How Elongator Acetylates tRNA Bases. *Int J Mol Sci. 2020.* DOI: 10.1126/sciadv.aaw2326

3. Gaik M, Kojic M, Stegeman MR, Öncu-Öner T, Koscielniak A , Jones A , Mohamed A, Chau PYS, Sharmin S, Chramiec-Głazbik A, Indyka P, Rawski M, Biela A, Dobosz D, Millar A, Chau V, Unalp A , Piper M , Bellingham MC , Eichler EE, Nickerson DA , Handan Guleryuz H, **Abbassi NEH**, Jazgar K, Davis MJ, Mercimek-Andrews S , Cingöz S, Wainwright BJ & Glatt S.; Functional divergence of the two Elongator subcomplexes during neurodevelopment. *EMBO Mol Med. 2022.* DOI: 10.15252/emmm.202115608

4. Jaciuk M, Scherf D, Kaszuba K, Gaik M, Rau A, Koscielniak A, Krutyhołowa R, Rawski M, Indyka P, Graziadei A, Chramiec-Głąbik A, Biela A, Dobosz D, Lin TY, **Abbassi NEH**, Hammermeister A, Rappsilber J, Kosinski J, Schaffrath R and Glatt S.; Cryo-EM structure of the fully assembled Elongator complex. *Nucleic Acid Research 2023.* DOI: 10.1126/sciadv.aaw2326

Publication in preparation (containing results presented in this thesis):

Abbassi NEH[#], Jaciuk M[#], Scherf D, Doborsz D, Jazgar K, Schaffrath R, Lin TL, and Glatt S; Atomic resolution of tRNA bound human Elongator complex and ligands, [#]These authors contributed equally. *Manuscript in preparation.*

Abbreviations

Code	Full name
Å	Angstrom
ACC1	acetyl coenzyme A carboxylase 1
ACO	Acetyl-Coenzyme A
ATPase	Adenosine triphosphatase
ASL	Anticodon stem and loop
CL	Central linker
Cryo-EM	Cryogenic Electron Microscopy
Cy5	Cyanine 5
DCA	Desulfo-CoA
DD	Dimerization domain
Dmc	Dehalococcoides mccartyi
DNA	DesoxyriboNucleic Acid
Dph3	Diphthamide biosynthesis 3
ECA	S-Ethyl-CoA
Elp	Elongator protein
EMSA	Electrophoretic Mobility Shift Assay
EPR	Electron Paramagnetic Resonance
FD	Familial dysautonomia
GOI	Gene of interest
GCN5	General control non-depressible 5
GST	Glutathione-S-transferase
H3	Histone H3
H4	Histone H4
HPLC	High Pressure Liquid Chromatography
ITC	Isothermal titration calorimetry
KAT	Lysine acetyltransferase
K_D	Dissociation constant
KDa	kiloDalton
KTI	*Kluyveromyces lactis* toxin insensitive
LB	Lysogeny broth, Luria broth, Lennox Broth
Min	Methanocaldococcus infernus
Mm	Mus muculus
mRNA	messenger RNA
MST	MicroScale Thermophoresis
ND	Neuro-degenerative disease
NMR	Nuclear Magnetic Resonance
ORF	Open Reading Frame
PTM	Post-translational Modifications
RALS	Right Angle Light Scattering
RNA	RiboNucleic Acid
RT	Room temperature
Sc	Saccharomyces cerevisae
(r) SAM	(radical) S-Adenosyl-methionine
SPA	Single Particle Analysis
SOB	Super Optimal Broth

TEV	Tabacco Etch Virus protease
TK40	Tubuline Lysine 40
Tm	Melting temperature
TPR	Tetratricopeptide repeat
tRNA	transfer RNA
TST	Twin strep tag
U$_{34}$	Uridine 34
WD40	B-propeller domain
X-ray	radiation

Abbreviation of catalytic products

Code	Full name
5-dA•	5'-deoxyadenosyl radical
xm^{5}U	5-methyluridines
cm^{5}U	5-carboxymethyluridine
cmo^{5}U	5-oxyacetic acid uridine
ncm5U	5-carbamoylmethyluridine
mcm5U	5-methoxycarbonylmethyluridine
mcm^{5}s^{2}U	5-methoxycarbonylmethyl-2-thiouridine
ncm^{5}Um	5-carbamoylmethyl-2′-O-methyluridine
mcm^{5}Um	5-methoxycarbonylmethyl-2'-O-methyluridine
mchm^{5}U	5-(carboxyhydroxymethyl)uridine methyl ester

Introduction

Protein translation

Living beings rise from cells, which contain diverse macromolecules that are built to execute functions and can be redesigned to fulfil various purposes (Pukkila, 2001). Macromolecules are most often made from simpler units – e.g., nucleotides, including DNA and RNA. A nucleotide is composed of a sugar molecule (a deoxyribose in the case of DNA; a ribose in the case of RNA), a base and a phosphate group. The bases are adenosine (A), thymidine (T), cytosine (C) and guanine (G) in DNA while A, C, G, and uridine (U) in RNA. Nucleotides exist in the form of polymer strands. DNA forms a double-stranded helix, and the two strands are held together by hydrogen bonds between paired bases (A-T and C-G). RNA, on the other hand, exists as a single strand. It follows the same base pairing rule to facilitate intramolecular folding to form secondary structures, such as simple hairpin motif. These secondary structure elements can be further folded into complex tertiary structure via long-range interactions. As a
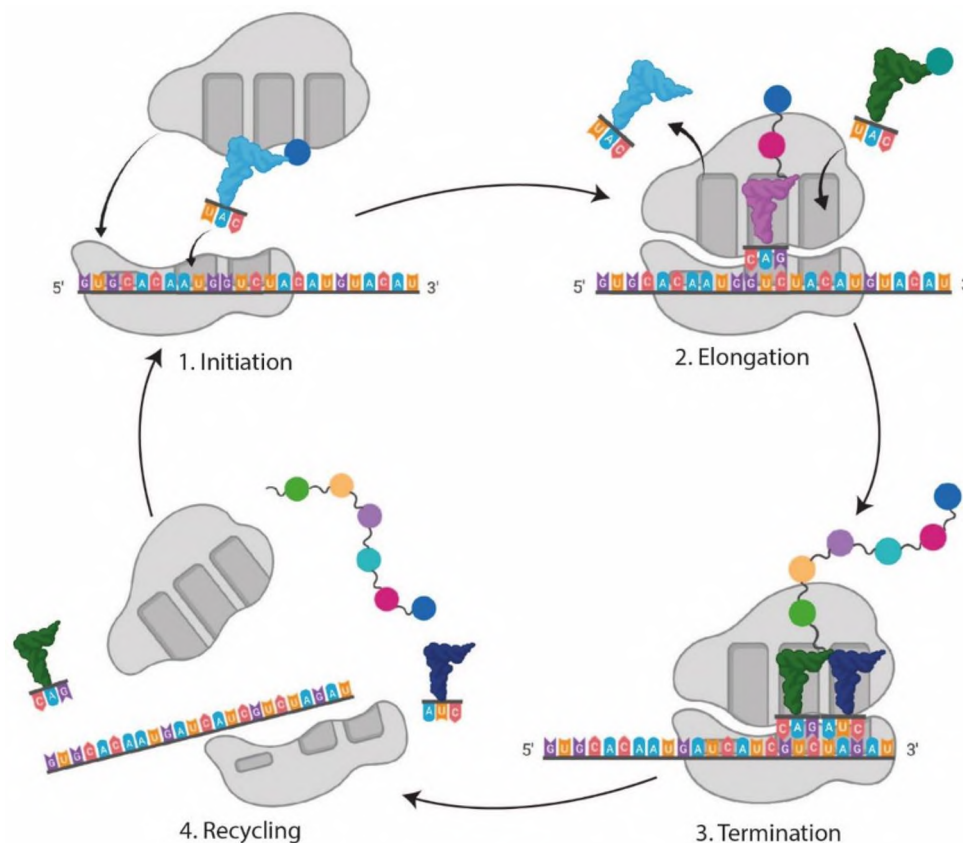
Figure 1. **Protein translation in eukaryotes**. 1. Initiation step requires the assembly of ribosome subunits around mRNA. Translation elongation steps bring amino-acylated tRNAs to match it with the exposed codon in ribosome to and adds the amino acid to the forming polypeptide chain. 3. Termination arises with the appearance of a stop codon in the mRNA sequence. 4. The Recycling starts with the disassembly of the protein from the ribosome, then the subunits disassemble and release the mRNA to get ready allow for a next translation event. (Figure created with Biorender.com)

result, RNA molecules have diverse and flexible structures which allow them to be able to catalyze reactions or interact with proteins, RNAs or other biomolecules.

The central dogma of molecular biology defines that DNA stores genetic information and transmits the information via RNA (transcription) to proteins (translation). The transcribed RNAs of a cell include coding RNAs as well as non-coding RNAs. Coding RNA, also termed as messenger RNA (mRNA), is further translated into a protein while the non-coding RNAs, such as ribosomal RNA (rRNA), small nucleolar RNA (snoRNAs) or transfer RNA (tRNA), execute their function directly.

In general, the process of translation is orchestrated by the ribosome, mRNA, tRNA and many accessory proteins that are involved in translation initiation (Merrick & Pavitt, 2018), elongation and recycling. Protein translation starts with the initiator tRNA and two ribosomal subunits (e.g., 40S and 60S in eukaryotes), which are recruited and assembled (initiation, see Figure 1). The mRNA serves as the template to pair with tRNAs via triplet pairing mechanism to select the correct amino acid-carrying tRNA to match the codons in the reading frame. This results in the proper amino acid incorporation in a correct sequence to form the nascent polypeptide chain (elongation) according to the genetic code. When the ribosome reaches a stop codon (UAG, UGA, and UAA) in its A-site, where no amino acid-carrying tRNA recognizes it, a release factor then enters the A site and releases the nascent peptidyl-tRNA in the P-site, which causes the termination of protein synthesis. Finally, additional proteins help ejecting the tRNA and mRNA and disassemble the ribosome into the subunits. The mRNA can be reused in the next round of translation which is called the recycling (Hellen, 2018).

As proteins are the workhorses in cells, stringent translation is an essential process to ensure the accuracy of the protein repertoire, also called the proteome. Achieving high translation fidelity requires multiple control steps. For instance, tRNAs must be charged only with correct amino acids at their 3'-end or the anti-codon of a tRNA must correctly pair with the mRNA codon in the A site of the ribosome. Besides faithfully transmitting codon messages in DNA to amino acid sequence in protein, ensuring the correct folding of the linear polypeptide chain (2D) to a biological active structure (3D) is equally important. The folding process of the polypeptide chain takes place co-translationally, meaning the nascent chain forms an extensive tertiary structure immediately when protruding from the ribosomal exit tunnel during protein synthesis. Moreover, the co-translational folding dynamics are connected with the synthesis rates of the polypeptide chain (Kaiser & Liu, 2018; Wruck et al., 2017). As the elongation rates are not constant during the synthesis (e.g., some codons are recognized and paired slower than

others), transient pauses result in a vectorial force to influence how the nascent polypeptide chain is folded. The regulation of ribosomes, mRNAs and tRNAs during translation determines the fate of protein folding and eventually affects proteome integrity (Nedialkova & Leidel, 2015; Pechmann et al., 2013).
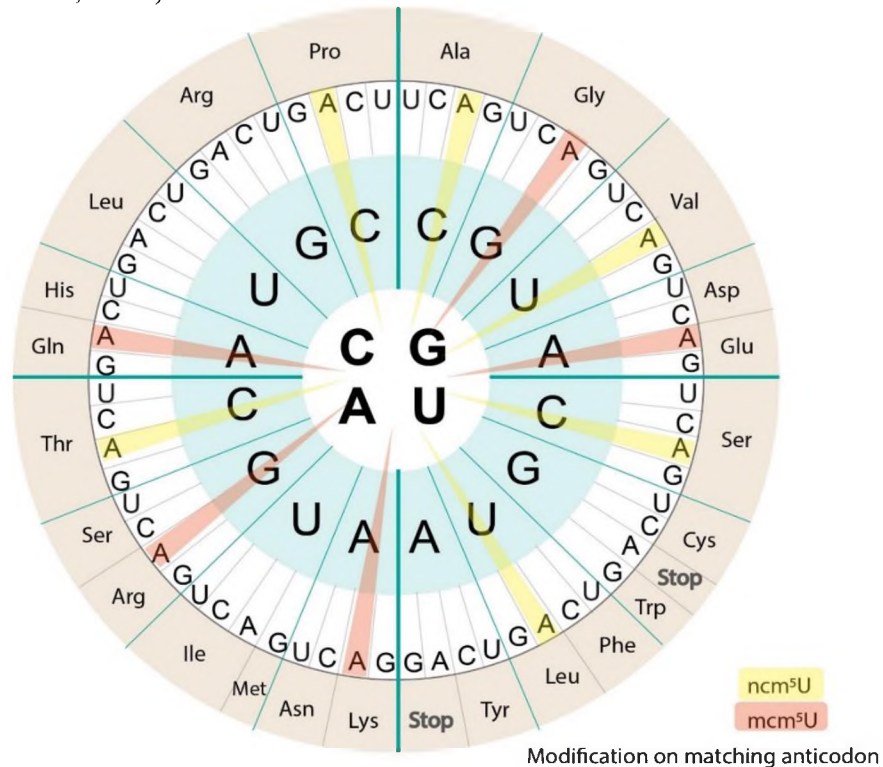

Figure 2. **Circular representation of the genetic code**. Codons are read from the center to the outside. The corresponding amino acids are written in the outer beige circle. Codons marked in light orange are recognized by the mcm5U34 modified anticodons and the codons marked in yellow are recognized by ncm5U34 anticodons. Figure inspired by E. Westhof and Johansson.

Deciphering a mRNA codon during translation involves Watson-Crick base pairing between mRNA and tRNA (Figure 2). During decoding the mRNA codons are interpreted in triplets, which results in $4^3=64$ possible combinations. However, only 20 amino acids are used (not counting selenocysteine, pyrrolysine or STOP codons) for protein synthesis. While almost all organisms use the same genetic code, some amino acids are encoded by more than one codon, which is called degeneracy of the genetic code (Mahlab et al., 2012).

The cells adapt their production of tRNAs depending on the stress they are exposed to and which step of the cell cycle they are at (Rak et al., 2021). In more complex organisms, it has been found that different cell types produce tRNAs for certain codons in different abundance, i.e. tRNA[Ala] is expressed at a significantly higher level in cells from the nervous system than the other cell types (Gao et al., 2022). It sometimes means that the species express a higher amount of proteins with codons that they can translate with their own selection of tRNAs. In molecular biology, we use this cell particularity and "codon optimize" the DNA

14

sequence of proteins, which we want to express in the organisms we use in the lab, to facilitate the expression.

Within the triplet interaction between tRNA and mRNA, the first two codon positions are restricted to Watson-Crick base pairing because they are highly restrained in the ribosome (Ye & Lehmann, 2022). In contrast, the pairing at the third position of the mRNA codon with the position 34 of tRNAs is most often non-canonical and more flexible in its geometry (Agris et al., 2017). In mitochondria and chloroplasts, a U at position 34 can pair with any nucleotides and is called a "super wobbling" position (Rogalski et al., 2008). As mentioned earlier, this extended wobbling is the result of reduced sets of available tRNAs.

tRNA structure and modifications

tRNA consists of 76-90 nucleotides and is best described in the simplified 2D cloverleaf structure (Figure 3) (Holley et al., 1965). The distinctive architecture consists of 5 basic elements, including T arm, D arm, accepter stem, anticodon stem loop (ASL), and the variable loop. In higher organisms, the 3′ end is further extended by the enzyme called tRNA nucleotidyltransferase which adds a single stranded CCA (Cytosine-Cytosine-Adenosine) sequence. The extended 3′ is used for subsequent aminoacylation to attach an amino acid via a covalent bond (Mörl et al., 2010; Sprinzl & Cramer, 1979). The crystal structure of yeast tRNA[Phe] reveals that D arm and T arm interact with each other to form an elbow, which then allows compaction of all other elements into a characteristic 3D L-shape architecture (H. Shi & Moore, 2000). Acting as an adaptor between mRNA and the elongated polypeptide chain, tRNA utilizes the anticodon (position 34, 35, and 36) within the ASL to base-pair with the corresponding mRNA codon and the acceptor stem, located at the opposite end of the L-shape,

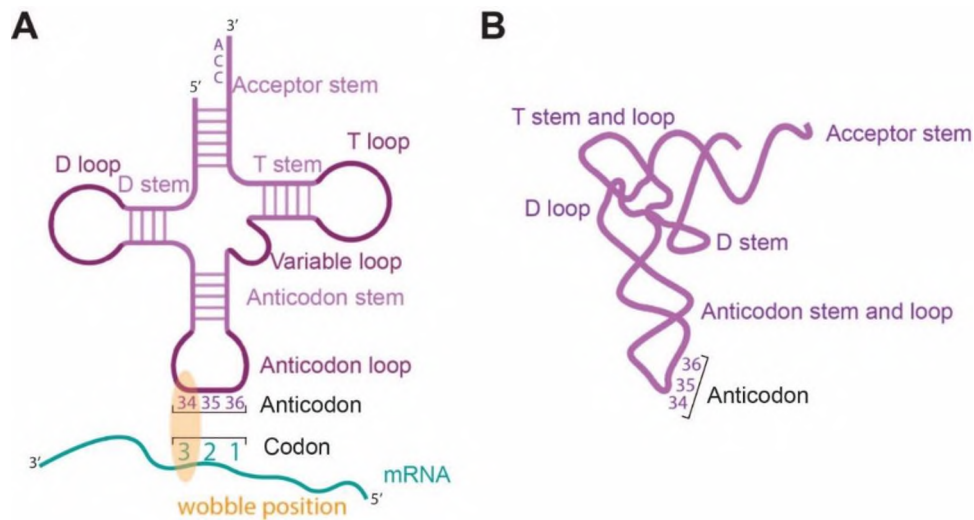delivers the amino acid for peptide chain formation.

Figure 5. **Description of a tRNA**. A. 2D structure of a tRNA with a CCA sequence on the acceptor stem, a T arm, a D arm, and an anticodon stem loop that pairs with the codon in mRNA via its anticodon. The wobble position, the 3rd position on the mRNA codon, is highlighted in orange. B. 3D structure of a L-shaped tRNA showing the interaction of T and D arm forms the characteristic elbow where the acceptor stem is at the opposite end to the acceptor stem. (Figure created with Biorender.com).

All tRNAs share the canonical L-shape structure and the different total length stems mostly from the varying number of nucleotides in the variable loop. The variable loop in the majority of tRNA has 4-5 nucleotides, whereas $tRNA^{Ser}$, $tRNA^{Leu}$, and $tRNA^{Tyr}$ have longer variable loops that consist of 10 or more nucleotides (Hanashima et al., 2016). Despite the highly conserved structure, the conservation of tRNA sequences is surprisingly low with only several invariable positions, including U_8, A_{14}, G_{18}, G_{19}, A_{21}, U_{33}, G_{53}, U_{54}, U_{55}, C_{56}, A_{58}, C_{61}, C_{74}, C_{75} and A_{76}. Therefore, poor sequence conservation can hamper the accuracy in identifying functional tRNA genes. To date, there are 429 bioinformatically predicted cytoplasmic tRNA genes in humans, but only approximately half of them were detected in cells (Tsutomu Suzuki, 2021).

To fulfill their role as adaptor, not only the conserved L-shape structure, but also chemical modifications on tRNA, are crucial for tRNA during the decoding process (tRNA epitranscriptome). The tRNA epitranscriptome is emerging as an important cellular modulator involved in multiple cellular events other than translation, such as regulation of stress responses caused by nutrient deprivation or xenobiotic exposures (Huber et al., 2019). During tRNA maturation, diverse and dense (>17% of all tRNA nucleotides are modified) decorations are installed (Ranjan & Leidel, 2019). The modifications are introduced either by default or in an inducible fashion, thereby controlling the structure stability or mRNA codon recognition. For instance, the invariant position U_{55} in all tRNAs is always a pseudouridine (Ψ), while m^1A58

in tRNAi^{Met} can be removed (Liu et al., 2016). Modifications of tRNA are heavily involved in regulating translation dynamically and therefore determine cell fate, cell survival and responses to external stimulations (Dyubankova et al., 2015; Ishida et al., 2011; T. Y. Lin et al., 2021; Tsutomu Suzuki, 2021; Taniguchi et al., 2018). Moreover, the modification profile can be tissue-, and cell type-specific (T. Y. Lin et al., 2021; Nau, 1976; Ohira et al., 2022; Taniguchi et al., 2018).

As they directly take part in protein translation, the modifications in the ASL are the most dense and structurally diverse in comparing to other domains of tRNAs (Agris et al., 2017). For instance, N6-threonylcarbamoyladenosine (t^{6}A) at position 37 is present in tRNAs that read ANN codons (A: adenosine, N: any nucleotide), which is required for maintaining the reading frame, preventing leaky scanning of initiation codons, and properly recognizing STOP codons (Agris et al., 2017). Some modification can be added independently (e.g. pseudouridine at position 39), while some require other priming modifications (Sokołowski et al., 2018). Some pre-requisite modifications serve as an additional recognition control for the second modifications. For example, 2'-O-methylation of C$_{32}$ and G$_{34}$ (Gm) are required for efficient wybutosine (yW) formation at m^{1}G$_{37}$ of tRNA^{Phe} in yeast and humans (Han & Phizicky, 2018). The modification of Cm34 or Um34 in *E. coli* tRNA^{Leu} is enhanced by the presence of i^{6}A$_{37}$.

In all domains of life, the wobble position is often modified by various chemical groups to enhance the pairing with mRNA codons. The adenosine at position 34 is converted to inosine via deamination which exists only in bacterial tRNA^{Arg} and 8 eukaryotic tRNAs (Rafels-Ybern et al., 2018). U$_{34}$ is decorated as xm5, where 5-oxyacetic acid (cmo^{5}U) modification exists in prokaryotes, while 5-carbamoylmethyl (ncm5) and 5-methoxycarbonylmethyl (mcm5) are present in eukaryotes. U$_{34}$ modifications have been demonstrated to facilitate proper protein translation speed, thus maintaining the proteome balance in cells (Ranjan & Rodnina, 2017). Depletion of U$_{34}$ modifications have been found to be lethal at the embryonic stage in some model organisms, including mice. In yeast, it renders cell tolerance to stress conditions (Nedialkova & Leidel, 2015). Furthermore, it has been linked to development, neuronal dysfunction in nematodes, and neurodegenerative diseases in humans (C. Chen et al., 2009; Tsutomu Suzuki, 2021). Although U$_{34}$ is always modified, a study in yeast revealed that there are 16 codons that contain the U$_{34}$ but only 11 of them are modified (Bjork et al., 2008) (Figure 2). Some tRNAs can be further thiolated (sulphur addition) in addition to mcm^5, forming mcm^{5}s^{2}U (5-methoxycarbonylmethyl-2-thiouridine) at position 34. The mcm and thiolation modifications pathways are catalyzed independently by different proteins, but when both

17

decorations are absent, the result in an exacerbated mutant phenotype in *Caenorhabditis elegans*, suggesting a functional cross-talk between the two modifications and their pathways (C. Chen et al., 2009).

Detection of RNA modifications can be achieved using various methods, including mass spectrometry or RNA deep sequencing (Carlile et al., 2014; Takeo Suzuki et al., 2020). The latter often requires chemical labeling of specific modifications to facilitate their identification (Dai et al., 2022). However, owing to direct RNA sequencing method, recently developed by Nanopore, RNA sequencing coupled detection of modifications can also be label-free (Tavakoli et al., 2023). Alternatively, in *Saccharomyces cerevisiae* cells the detection of U_{34} modification can also be performed *in vitro* by adding *Kluveromyces lactis* gamma-toxin (Glatt et al., 2016; Studte et al., 2008). This specific RNA endonuclease recognizes the mcm^5U and cleaves the tRNA target between position 34 and 35 (Lu et al., 2008). To complement the detection of U_{34} modification, a canavanine sensitivity assay, which is dependent on the presence of modified U_{34} in tRNA, in yeast can be used to observe a direct phenotypic output (Krutyhołowa et al., 2019).

tRNA modification enzymes and cofactors

In contrast to the vast number of different chemical modifications in tRNAs (including mitochondrial and cytosolic), only 48% of the tRNA-modifying enzymes have been validated in mammals, while 23% of the modifying genes are still completely unknown (De Crécy-Lagard et al., 2019). The expression levels of tRNA modifying enzymes seem to be correlated with cell proliferation rates and cellular responses to environmental changes. For instance, they seem to be upregulated in highly proliferative cells (e.g., testis) and downregulated in differentiated tissues (e.g., less dividing and proliferation cells). The prenylation of A_{37} of tRNAs in bacteria can be induced by the up-regulation of MiaA to control translational frameshifting and to alter the proteome in response to external stimuli (Fleming et al., 2022).

The catalytic mechanisms on tRNA modifications are as diverse as their chemical composition. They can be a simple isomerization reaction or complex catalytic reactions that involve several ligands, such as *S*-adenosyl-l-methionine (SAM) or acetyl-CoA (ACO). Pseudouridylation by pseudouridine synthases is a simple conversion reaction, not even requiring a cofactor, that exchanges the position of N1 and C5 in uridine bases to produce pseudouridine (T.-Y. Lin et al., 2022). Methylations of RNAs are introduced by a group of enzymes called radical *S*-adenosyl-L-methionine (rSAM) enzymes, which require iron-sulphur

clusters and SAM (Kimura & Suzuki, 2015). Depending on the catalytic reaction, rSAM domains harbor one or more iron-sulphur clusters in their active site. The iron-sulphur cluster is commonly coordinated in the enzymes via a CX3CX2C motif (C: Cysteine, X3: three other amino acids, X2: two other amino acids) and its presence can be detected by UV–vis absorption, Raman spectroscopy, Mössbauer spectroscopy or EPR analysis (Broderick et al., 2014). SAM is a versatile substrate that provides a methyl group and a 5'-deoxyadenosyl radicals (5-dA•) (Broderick et al., 2014). The methyl group is added to substrates like lipids, proteins, RNA, or DNA while the 5-dA• can even be the source for many catalytic reactions (Adami & Bottai, 2020). RlmN, a dual methyltransferase of tRNA and rRNA, has a distinct catalytic reaction compared to the canonical methyltransferase (Adami & Bottai, 2020). A "ping-pong" mechanism is employed by RlmN/Crf that does not use SAM for direct transfer of the methyl group to a substrate. Instead, the reaction starts with the transfer of one methyl

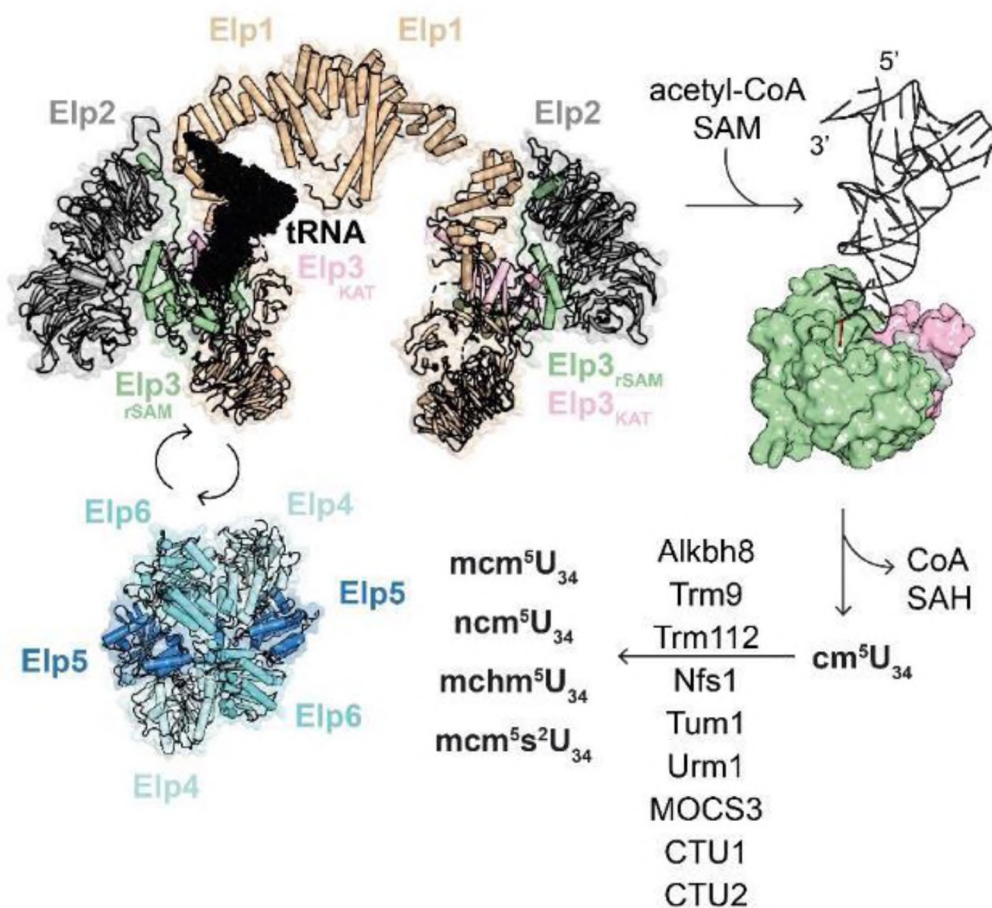Figure 6. **Elongator mediates tRNA modification.** Elp123 binds a tRNA molecule via Elp1 and Elp3. Upon tRNA binding, ACO is recruited and hydrolyzed while SAM is cleaved. The enzymatic reaction releases a cm⁵U₃₄-modified tRNA together with the Coenzyme A and SAH by-products. With the help of Elp456, the tRNA is released and then subsequently modified by other enzymes. (Figure adapted from Abbassi et al. 2020)

group from one SAM molecule onto an intermediate acceptor, which is followed by a radical-initiated methyl transfer from the second SAM molecule to substrate.

In contrast to the numerous SAM-involved methylation of tRNAs at various positions, ACO is known to be used for cm^5U_{34} and N4-acetylcytidine (ac^4C) modifications. The former is catalyzed by Elongator complex at U_{34} position of RNA (see details in next section) while the latter is executed by acetyltransferases, including TmcA (bacteria) and N-acetyltransferase 10 (NAT10 in human) (L. Chen et al., 2022; Ito et al., 2014). In addition, the ac^4C formation is dependent on the enzyme-mediated ATP hydrolysis. A co-crystal structure of bacterial TmcA revealed the unique RNA helicase module that employs ATP hydrolysis to drive and deliver the wobble base of elongator $tRNA^{Met}$ to the active site within its GCN5-related N-acetyltransferase domain (Chimnaronk et al., 2009).

Elongator complex - Elp123 subcomplex and structure of each subunit

In eukaryotes, U_{34} in several tRNAs is modified into various xm^5U nucleotides, including mcm^5U, ncm^5U and $mchm^5U$. Among those tRNAs, $tRNA^{Arg}$ and $tRNA^{Gly}$ harbor a $mchm^5U_{34}$. The formation of xm^5U requires a cascade reaction involving multiple enzymes (Figure 4) (N. Abbassi et al., 2020). First, U_{34} is converted to the cm^5U_{34} precursor by Elongator. The precursor then undergoes a methyl esterification by the methyltransferase Trm9/Trm112 to synthesize mcm^5U_{34} or by an unknown mechanism to form ncm^5U_{34} (C. Chen et al., 2011). The hydroxylation of mcm^5U_{34} by the ALKBH8 dioxygenase further generates $mchm^5U_{34}$ (Van Den Born et al., 2011). Recently, it was confirmed that the ribose of mcm^5U and ncm^5U can be methylated by FTSJ1 to form 5-methoxycarbonylmethyl-2'-O-methyluridine (mcm^5Um) and 5-carbamoylmethyl-2'-O-methyluridine (ncm^5Um), respectively (Nagayoshi et al., 2021). Apart from the cascades leading to xm^5U modifications, Urm1 is known to execute a thiolation of U_{34} in $tRNA^{Gln}$, $tRNA^{Glu}$ and $tRNA^{Lys}$, resulting in s^2U_{34} (Pedrioli et al., 2008). Together with the mcm^5U modification and s^2U_{34}, mcm^5s^2U is formed in certain tRNAs. Of note, the Urm1-mediated thiolation on U_{34} is introduced independently of mcm^5U formation and *vice versa*.

The Elongator complex is highly conserved in eukaryotes. It is composed of two copies of six subunits named Elp1, Elp2, Elp3, Elp4, Elp5, and Elp6. They form two subcomplexes, namely Elp123 and Elp456. The interaction of the two subcomplexes is intermittent and is influenced by salt concentration (Krogan & Greenblatt, 2001). Initially, Elongator was

identified as a histone acetyltransferase for two main reasons: i) it was co-purified with RNA polymerase II and ii) the sequence of the catalytic Elp3 harbors a lysine transferase (KAT) domain, which is homologous to canonical GCN5 domains in acetyltransferases (Otero et al., 1999). Several subsequent studies linked Elongator to transcriptional regulation and proposed that Elongator is involved in protein acetylation of histone and tubulin proteins, cell cycle and DNA damage repair. In contrast to these proposed roles, Huang and others demonstrated that yeast Elongator is responsible for U_{34} modification in tRNAs (Hoffmann et al., 2015; Huang et al., 2005; Krutyhołowa et al., 2019; Lu et al., 2005). Moreover, several Elongator-associated proteins, including Kti11-Kti13 and Kti12, were identified to participate in the U_{34} modification. Depletion of the U_{34} modification has been shown to alter ochre tRNA^{Tyr} suppression and to hamper the efficiency of decoding UAA ochre codons in yeast. The Elongator-dependent translation defects can be rescued by the overexpression of unmodified tRNAs (Fernández-Vázquez et al., 2013). This evidence distinguishes the Elongator-dependent U_{34} modification as the main role of Elongator, defining it as a modulator of protein translation. The modified U_{34} base participates in codon-anticodon pairing which in consequence controls the translation speed (Ranjan & Rodnina, 2016). Thereby, it is tightly coupled to stringent protein translation control mechanisms (Nedialkova & Leidel, 2015). Therefore, the inability to produce functional Elongator indirectly causes aberrant protein acetylation or cellular events by affecting protein synthesis and proteome imbalance.
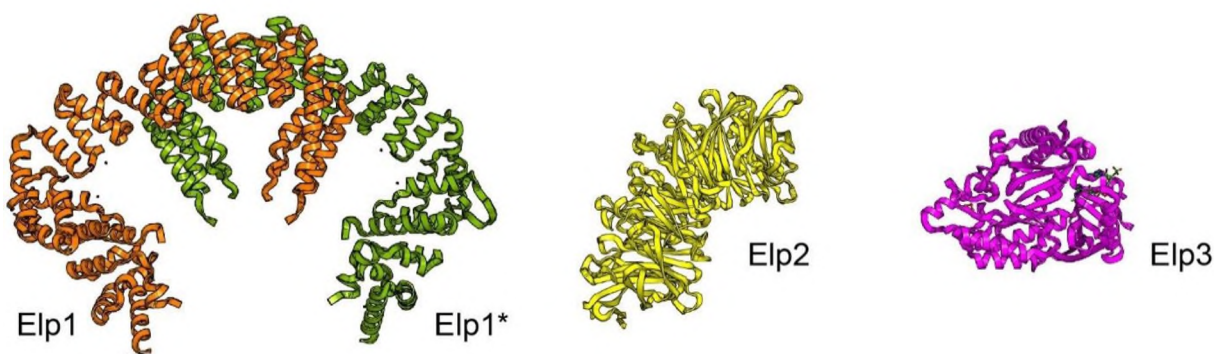
Figure 7. **Crystal structures of each Elp123 subunits**. Cartoon representitives of yeast Elp1 dimer (orange and green (Elp1*)) (PDB: 5QCR), yeast Elp2 (yellow) (PDB: 4XFV), and bacterial Elp3 (magenta) with the bound ACO is in green (PDB: 5L7J).

Elp1, also known as IkB kinase complex-associated protein (IKAB), is the largest Elongator subunit. It is composed of two N-terminal WD40 domains, followed by a tetratricopeptide repeat (TPR) and a dimerization domain in the C-terminus (Figure 5). Elp1 forms a homodimer via its dimerization domain and serves as the scaffold for Elongator

complex assembly. The C-terminus of Elp1 also binds to tRNA and interacts with Kti12 as well as a casein kinase 1, called Hrr25 kinase. The recruitment of Kti12 and Hrr25 is regulated by phosphorylation sites on a cluster of serine residues of Elp1. The phosphorylation status of Elp1 is linked to Elongator-dependent tRNA modification activity.

Elp2, known as Stip1 (STAT3-interacting protein), harbors two WD40 domains which obey a 7-bladded β-propeller topology (Dong et al., 2015; Fellows et al., 2000). Elp2 along with the WD40 domains of Elp1 act as a structural hub that clamps Elp3 in between to form the Elp123 subcomplex. The stability of Elp2 also influences Elongator complex integrity (Kojic et al., 2021).
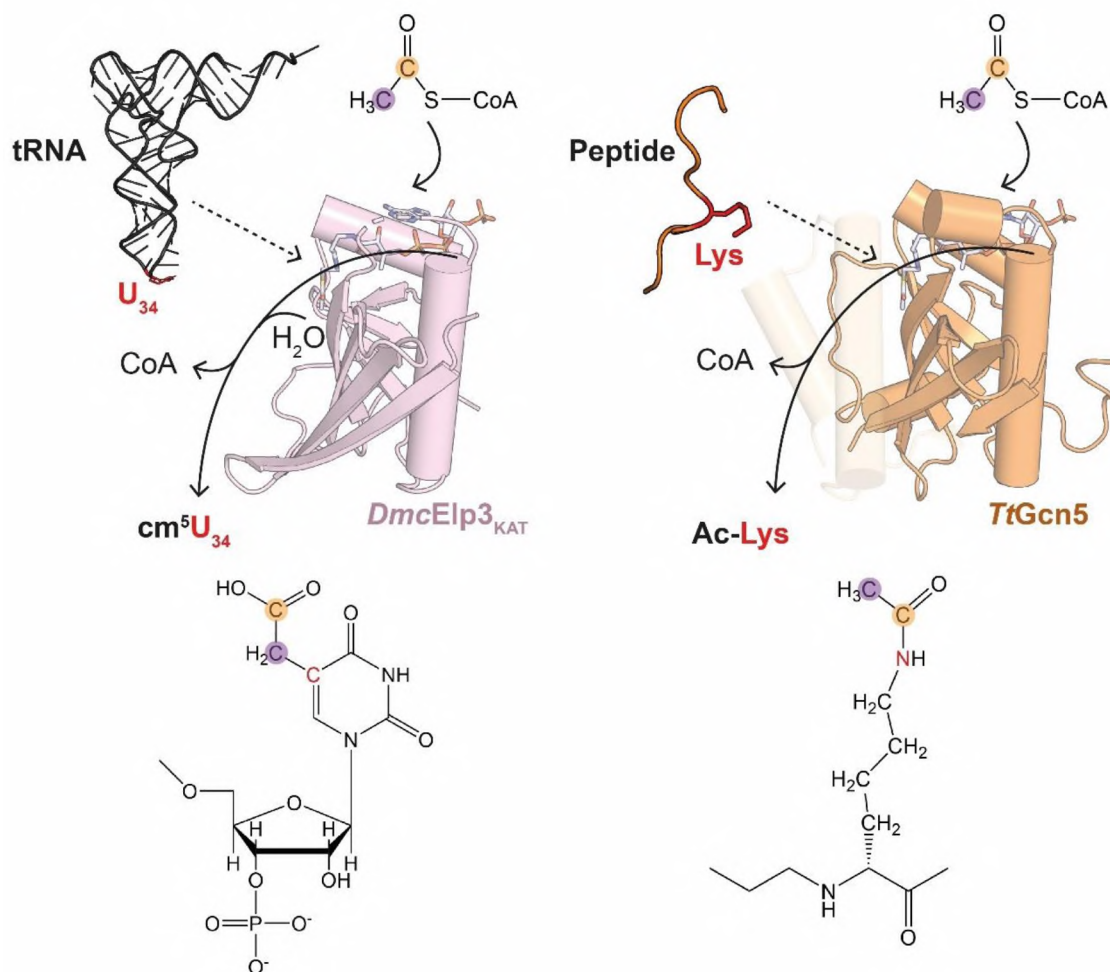
Figure 8. **Proposed ACO hydrolysis in Elp3 triggered by tRNA and in GCN5 triggered by histone**. The reactive carbons of ACO are highlighted in orange circle (acetyl radical for cm^5 modification) or purple circle (carbonyl group of the thioester of ACO) above each protein. The reactive sites of carbon on U_{34} and nitrogen on lysine are both colored in red and present the C-C bond for the cm5 addition and the C-N bond for the acetylation, respectively. (Adapted from Abbassi et al. 2020)

The Elp3 subunit catalyses the cm^5U_{34} modification reaction and consists of two functional domains, namely a *S*-Adenosyl-methionine (SAM) domain and a lysine

acetyltransferase (KAT) domain. Elp3 can also be found in non-eukaryotic domains of life, such as one specific bacteria clade (*Dehallococcoides app*), some viruses (e.g., *Kleusnovirus, or Pithovirus*) and archaea (e.g., *Methanocaldococcus app*). Interestingly, these non-eukaryotic Elp3s seem to be acting alone without other Elongator subunits present in these species. Sequence alignments of Elp3 proteins show high sequence similarity and identity (about 40%) in the functional domains among various species but very low conservation in their N-termini (T.-Y. Lin et al., 2019). A bacterial Elp3 was identified in *Dehalococcoides mccartyi* (Dmc), an anaerobic Dehalogenating bacterium isolated from toxic waste (Glatt et al. 2016). A high-resolution crystal structure of *Dmc*Elp3 revealed the details of KAT and SAM domains and their relative spatial arrangement. The two functional domains form a cleft to accommodate a tRNA molecule in the catalytic pocket. The KAT domain resembles the canonical acetyltransferase domain, but the potential protein substrate binding site is blocked by the presence of the SAM domain. An ACO binding pocket resides in the KAT domain, but the binding site is partially covered by a flexible loop, indicating a regulation mechanism of ACO binding. The SAM domain contains an iron-sulphur cluster bound by the CX3CX2C motif. Moreover, the biochemical characterizations provided evidence that *Dmc*Elp3 binding to tRNA is primarily mediated via interactions of the ASL and the D loop. Combining structural and biochemical studies led to the characterization of critical residues responsible for the catalytic activity (Glatt et al., 2016; Huang et al., 2005). However, culturing *D. mccartyi* bacteria in the lab is technically very challenging and it is still not clear whether this prokaryote carries any Elongator-dependent xm^5U34 modifications in tRNA. Meanwhile, Selvadurai and colleagues have reconstituted the chemical reaction of Elp3-mediated cm^5 addition on uridines, using purified Elp3 from the archaea *Methenalcaldococcus infernus* (*Min*Elp3) (Selvadurai et al., 2014). Upon tRNA binding to Elp3, two subsequent events take place: ACO hydrolysis and cleavage of SAM. Hydrolyzing ACO produces the necessary active acetyl group, while cleavage of SAM generates the 5′-dA• (Paraskevopoulou et al., 2006). The hydrolyzed acetyl group then reacts with the radical and forms an acetyl radical, which is attached to the C5 position of U_{34} to form a C-C bond and produce cm^5U (Figure 6). To date, this is the only *in vitro* study that reports an Elp3-mediated cm^5 addition of tRNAs. The activity of the eukaryotic Elongator complex requires further investigation.

The Elp456 subcomplex is a hetero hexamer consisting of two Elp456 trimers. It forms a ring-shaped helicase-like complex with the following circular arrangement of the subunits: Elp4-Elp5-Elp6-Elp4-Elp5-Elp6 (Glatt et al., 2012) (Figure 7). Elp456 has a basic ATPase activity, but unlike other known helicases its activity is not triggered by the presence of nucleic acid. Although, the crystal and cryo-EM structures of Elp456 have been reported (Gaik et al., 2022), parts of the terminal domains of Elp4 and Elp5 have still not been fully resolved. The functional role of Elp456 relates to the disassociation of tRNA upon ATP hydrolysis (Glatt et al., 2012). Moreover, Elp456 is found to act on a specific subset of tRNAs and is responsible for their release from the full Elongator complex (Gaik et al., 2022).
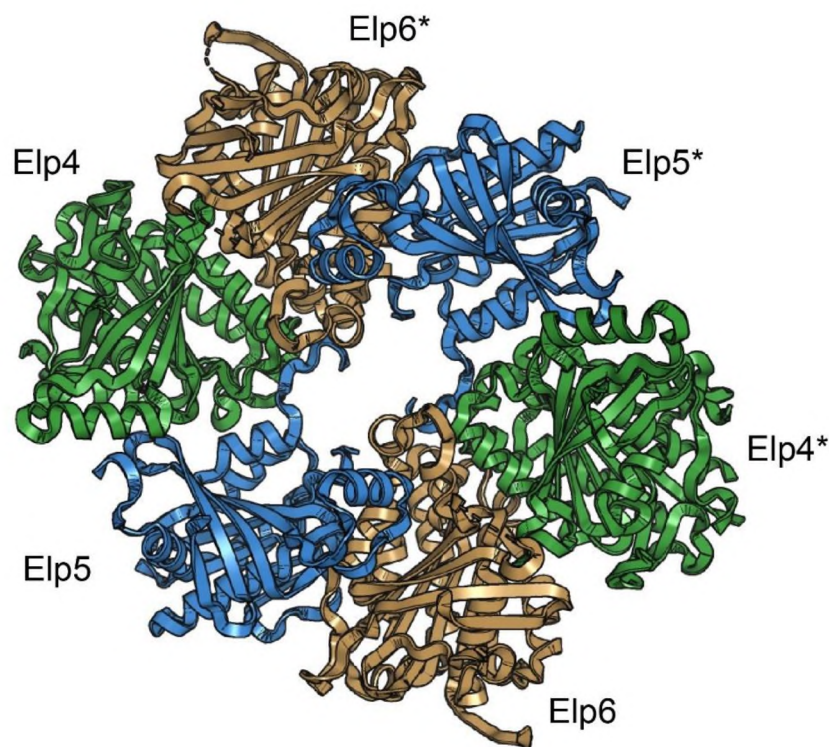
Figure 9. **Structure of Elongator subcomplex Elp456**. A cartoon representative of Elp456 ring structure which is present in two copies arranged. Elp4 (green) is interacting clockwise with Elp6 (sand) then Elp5 (blue) (PDB ID: 4EJS).

A single particle cryo-EM structure of the yeast holo-Elongator (Elp123-Elp456) revealed the complex architecture, where we show that only one Elp123 lobe is contacted by the Elp456 sub-complex (8ASV) (Figure 8). Via the DD of Elp1, the complex forms an "arch" domain and results in an architecture that contains two ELp123 lobes, presenting a "moth" shape. Each lobe accommodates Elp1, Elp2 and Elp3 (Dauden et al. 2019). Elp456 interacts

with one lobe asymmetrically (Séraphin et al., 2017), though it has been demonstrated that in principle one Elp123 dimer of trimers can accommodate Elp456 on both lobes simultaneously (Setiaputra et al., 2017). However, this seems only possible by elevated concentration of Elp456 added exogenously, and unlikely in the endogenous Elongator complex. Recently, high-resolution cryo-EM structures of holo-Elongator from yeast (3.96 Å) and mouse (4.01 Å) have confirmed that Elongator is highly conserved among species not only in sequences but also in complex assembly (Jaciuk et al., 2023). In addition, the C-terminus of Elp1 takes part in the interaction with Elp456 as well as with tRNA. This mutually exclusive interaction seems to determine the fate of tRNA association/disassociation.
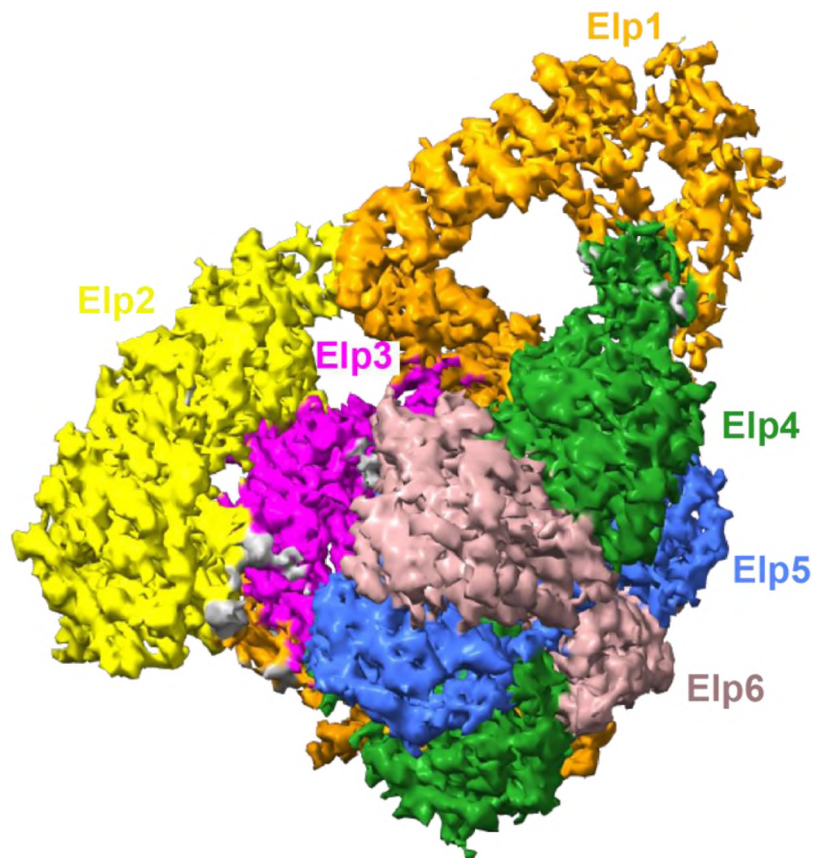

Figure 10. **Cryo-EM map of *Sc*Elp123456**. Front view of the yeast holo Elongator map obtained by cryo-EM (PDB: 8ASV). Each subunit is colored as Elp1 in orange, Elp2 in yellow, Elp3 in magenta, Elp4 in green, Elp5 in blue and Elp6 in sand.

Pathogenic mutations in Elp complex

Accumulating evidence links the Elongator complex to severe human pathologies, including neurodegenerative disorders and cancers. Several clinically relevant variants of the Elongator complex are reported and these mutations are located in all subunits, indicating that all subunits are required for the full activity of the complex in humans (N. Abbassi et al., 2020; Gaik et al., 2023).

Several mutations in the *Elp1* gene are linked to Familial dysautonomia (FD, also known as "Riley-Day syndrome"). The most common FD mutation is found at a splice site in intron 20, which results in skipping of exon 20 in the mature mRNA and loss of the Elp1 protein. Interestingly, the altered spliced mRNA product is only observed in the brain, whereas the full-length mRNA is still present in blood cells from patients, indicating a tissue-specific splicing defect (Slaugenhaupt et al., 2001). A tissue-specific illness from a pathogenic Elp1 variant is also found in retinal ganglion cells that leads to cell degeneration (Ueki et al., 2018). Another example is the R696P missense mutation in Elp1, which seems to be important for enzyme integrity by likely disrupting the interaction between Elp1 and Elp3 (H. Xu et al., 2015). Other missense mutations in Elp1 have also been identified, including P914L, C1072S and P1158L, but their detailed contribution to the formation of FD, as well as to bronchial asthma, is largely unknown (Dauden et al., 2018).
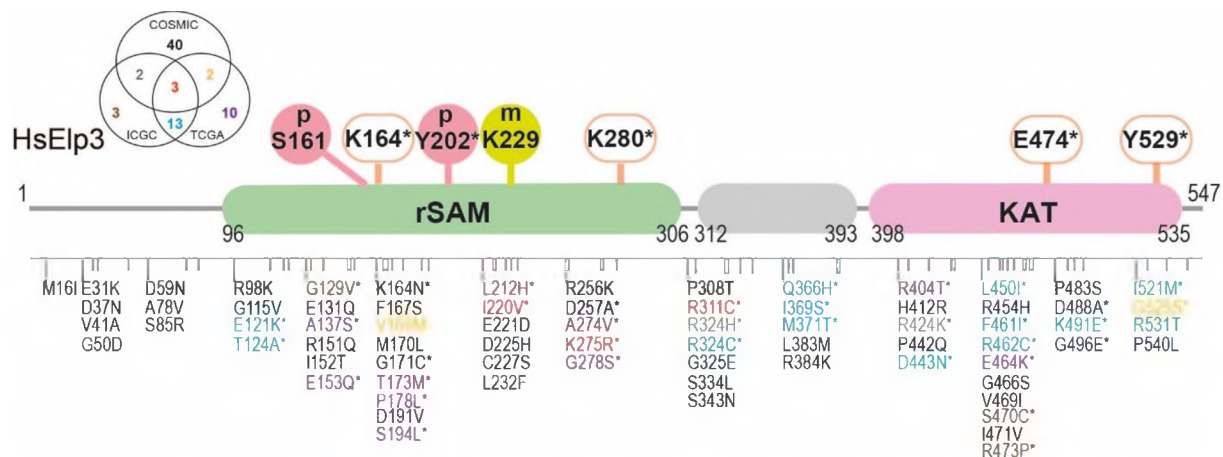
Figure 11. **Clinically relevant mutations of human ELP3**. The positions of the modifications in human ELP3 are shown graphically with a color-coding system representing the different databases they were deposited. The experimentally confirmed residues are marked with an asterisk, and the PTM sites (solid circles) as well as the ACO binding/hydrolysis catalytic residues (open squares) are also listed with their human ELP3 residue numbers and domains.

Although Elongator dysfunctions cause neurodegenerative disorders, mutations in different subunits affect different neuronal cells and thus lead to different phenotypes.

Mutations in the Elp2 gene are linked to intellectual disability and autism spectrum disorder (Cohen et al., 2015; Kojic et al., 2021). Experiments in mouse models using mutant variants resulted in aberrant brain development, recapitulating the patient phenotypes and clinical symptoms (Kojic et al., 2021). Mutations in Elp4 gene were found to associate with neurodegenerative disorders, autism and epilepsy (Addis et al., 2015). Moreover, mutations in Elp6 cause Purkinje neuron degeneration and are not linked with microcephaly, like the Elp2 mutants. It was further proposed that mutations in the catalytic Elp123 subcomplex compromise all Elongator-dependent tRNA modifications, whereas the mutations in Elp456 might only affect a subset of tRNAs that require Elp456 binding (Gaik et al., 2022).

In contrast to the loss of function of Elongator in neurodegenerative disorders, overexpression of Elp3 and Elp4 has been observed in cancer cells, including breast cancer and hepatocarcinoma (HCC). The high expression levels of Elp3 and Elp4 lead to tumor initiation and increased metastasis and invasion (Delaunay et al., 2016; Ladang et al., 2015). The overexpression of Elp3 or Elp4 has been further demonstrated to enhance the level of metalloprotease-2 (MMP-2) and MMP-9 (markers associated with cell invasion, metastasis and angiogenesis) in HCC tumors (Y. Xu et al., 2018). Furthermore, more mutant variants of Elp3 are reported (Figure 9) and a platform is urgently needed to study their impacts on the eukaryotic Elongator complex activity *in vitro* and *in vivo*.

Aim of this work

Previous work has demonstrated that Elp3 is the main protein mediating tRNA binding and catalyzing the modification reaction. However, the structural details of the tRNA bound structure with Elp3 or Elp3 in the context of other subunits (Elp123 or the fully assembled Elongator complex) are still under investigation.

This study aims to address the following main questions.

- How does Elp3 interact with tRNA?
- How does tRNA trigger Elp3-mediated ACO hydrolysis?
- Does the eukaryotic Elp3 catalyze the reaction like its archaea counterpart?
- Is the human Elongator complex structurally and functionally similar to its yeast counterpart?

Our Hypotheses are based on previous discoveries made in Elp3 and similar proteins:

- We expect the basic residues found in the pocket between the SAM and KAT domains to be involved in the tRNA interaction.
- Since the modifiable tRNAs and ACO can be found is similar ranges in the cell (the modifiable tRNAs concentration can be estimated around 6 to 14 µM (Frenkel-Morgenstern et al., 2012) and the ACO cytoplasmic concentration is estimated around 7 µM (Ronowska et al., 2018) we can hypothesize that Elongator binds to Acetyl-CoA first while waiting for a modifiable tRNA to bind and trigger the hydrolysis and the modification.
- The catalytic reaction in eukaryotic Elp3 might be less efficient than the archaeal one since eukaryotes have 11 more proteins to share the activity with.
- We expect both complexes to work in a similar fashion, as their protein sequences are well conserved.

To test these hypotheses, I planned to obtain a eukaryotic tRNA-Elongator-ligand structure (i.e., ACO analogs) and characterize the activity of the protein complex. In addition, understanding the structure-function relationship of the Elongator complex and its variants, as well as its interactions with other proteins and ligands, could provide valuable insight into the molecular basis of diseases that are associated with this complex. In the long run, this knowledge could be used to develop novel therapeutic strategies to target Elongator-associated diseases.

Methods

Cloning for non-eukaryotic Elp3

The sequence of MinElp3 was retrieved from UniProt and was synthesized using the GenScript service. The sequence was codon optimized for the bacterial expression systems. The open reading frame (ORF) was flanked by NcoI and XhoI in the pETM11 or pETM30 vectors, which allows the expression of the protein of interest fused with a GST tag and His6 tag. To generate point mutation versions of Elp3, the mutagenesis method was applied by using a pair of primers containing the mutation sites. The PCR was performed according to the manual using the plasmid with the wild-type as the DNA template, primers, dNTP, 5X reaction buffer, DMSO and Phusion polymerase. In detail, the PCR was run with 18-25 cycles, the annealing temperature was set to 50 °C and the extension time was dependent on the length of the target (15 sec/1k bp). The DNA templates were then digested by the treatment of DpnI (Thermo Fisher) at 37 °C for 30 minutes. The PCR product was then subjected to transformation into chemo competent cells (XL-1-Blue). The chemo competent cells were thawed slowly on ice and 1/10 v/v of the PCR product was added and incubated on ice for 10 minutes. The cells were then heated at 42 °C for 45 seconds and cooled on ice for 10 minutes. The mixture was then mixed with 300 µl of Super Optimal Broth (SOB) and further incubated at 37 °C for 90 minutes. The cell suspension was then applied to a lysogenic broth (LB) plate with suitable antibiotic for cultivation at 37 °C overnight. The colonies were further incubated in 2 ml LB broth for plasmid DNA extraction. The plasmid extraction was performed using the GeneJET™ Plasmid Miniprep Kit (ThermoFisher) and then sent for Sanger sequencing to confirm the mutation sites.

For generating a truncated version of MinElp3, a pair of primers were designed to contain the restriction enzyme cutting sites and the sequences that are complementary to the target sites. A PCR was performed, and the PCR products were resolved on an agarose gel (1%) at 100V for 30 minutes. The gel was stained using SYBRsafe and visualized under UV. The band of interest was cut from the gel and the DNA was eluted using the GeneJet gel extraction kit. The DNA was further subjected to restriction enzyme digestion with suitable restriction enzymes with incubation at 37 °C for 1 hour. The digested DNA (insert) was then cleaned up by a DNA extraction kit. Meanwhile, the vector, namely pETM11 or pETM30, were subjected to restriction digestion and followed by phosphatase treatment and the linear DNA was resolved on an agarose gel and extracted as mentioned above. The linear plasmid was then mixed with the DNA fragments (insert) using ratios 7:1 (insert: vector) in 10 µL reaction

volume containing the T4 ligase and 10x Ligation buffer. The mixture was incubated at room temperature for 2 hours and subjected to transformation in the XL-1-Blue competent cells. The obtained colonies were further cultivated to obtain plasmid DNA. The presence of the insertion in the plasmid was checked by restriction enzyme digestion and followed by resolving the product in an agarose gel. The clones with proper insert were then verified by sequencing.

Cloning for Eukaryotic Elp3

DNA constructs

Codon-optimized open reading frames of *Hs*ELP1 (O95163), *Hs*ELP2 (Q61A86) and *Hs*ELP3 (Q9H9T3) from *Homo sapiens* were cloned into the pFastBac1 HTa vector. ELP3 was cloned with an additional in-frame Twin-strep-Tag at its 3′ end. The *Hs*ELP123 construct was generated using Gibson assembly by amplifying all three genes in PCR with primers adding specific overhangs on the 5′ and 3′ sides of each expression cassette, allowing to determine the specific order of the ORFs. Subsequently, the amplified modules were assembled within the pBig1a plasmid using established protocols and primers. Mutations in ELP123 were introduced by QuikChange mutagenesis. The construct for production of the ELP456 complex from *Homo sapiens* in insect cells was previously described in (Gaik et al., 2022). The synthesized MinElp3 gene was amplified by PCR and inserted in the pETM30 vector within NcoI and XhoI restrictions sites. Single point mutations or truncations were generated using QuikChange PCR protocol. Sequences were checked by an external sequencing service.

Site-directed mutagenesis PCR for double mutants

Plasmid pBig1b_*Hs*ELP123 prepared previously in the lab was used as a template. First, point mutations were introduced with an optimized site-directed mutagenesis PCR protocol, where the forward and reverse strands were amplified separately with an initial denaturation at 98 °C for 30 seconds, denaturation at 98 °C for 10 seconds, annealing at 55 °C for 20 seconds, extension at 72 °C for 3 minutes, repeated in 25 cycles, finished by the final elongation at 72 °C for 10 minutes. Next, an annealing step in the decreasing temperature gradient was done at 98 °C for 5 minutes, 95 °C, and 90 °C for 1 minute each, then each following temperature for 30 seconds: 80 °C, 70 °C, 60 °C, 50 °C, 40 °C and stored at 20 °C. To remove the template DNA, a DpnI digestion for 30 minutes at 37 °C was performed with 10 units of enzyme/µg DNA.

Deletion PCR for truncations mutants

A similar strategy using a 2-step PCR was used for introducing deletions. PCR parameters consisted of initial denaturation at 98 °C for 30 seconds, annealing at 60 °C for 30 seconds, and extension at 72 °C for 6,5 minutes, repeated in 35 cycles, before final elongation for 13 minutes. Afterward, products were annealed and exposed to DpnI treatment in the same conditions as site-directed mutagenesis PCR.

Restriction-free cloning

Primers complementary to both, the GOI and the vector, were designed and a PCR in two steps was performed. First a mega primer is created with the designed primers and the GOI. The Mega-primer is then used for the second PCR with the vector of interest.

Gibson assembly

The genes were extracted from their pFastBac backbone by amplification in a PCR machine using the "Cassette" primers for Gibson assembly. The receiving plasmid (pBig1a or pBig1b depending on the sub-complex) can contain up to 5 genes, which are arranged from alpha to omega. The position of the genes is thus decided by using the corresponding cassette primers to amplify the correct connecting sequence at each end. After digesting 1 μg of pBig1a (for Elp123) with SwaI, all the inserts and the vector were heated at 50 °C for 60 min in a PCR machine while using a 5:1 ratio of insert to vector and the NEB Gibson mix. The resulting mixture was transformed into KCM cells, and the screening of colonies was performed in the following days/weeks.

Protein expression in bacterial expression system and purification

Plasmids were transformed into the protein expression bacterial strain (BL21(DE3) pLysS) using the electroporation method and colonies were further cultivated in 2 ml LB at 37 °C overnight as the start culture. The next day, 1 ml of culture was mixed with 1 L of Terrific Broth (TB) media for further culture at 37 °C. When the OD_{600} reached 1.2, IPTG (0.5 mM) was added to the culture to induce protein expression at 18 °C for further 16 h cultivation. Cells were collected by centrifugation at 6,000 rpm for 15 minutes at 4 °C and resuspended in lysis buffer (50 mM HEPES, pH7.5, 300 mM NaCl, 5 mM DTT, 5 mM $MgCl_2$, protease inhibitor and DNase) and lysed using a microfluidizer. The cell debris was spun by centrifugation at 20,000 g at 4 °C for 30 minutes. The supernatant was loaded to a GSTPrep affinity column at the speed of 0.5 ml/minute. The column was washed by lysis buffer and followed by high salt buffer (lysis buffer with 1 M NaCl) wash. The protein was eluted in the elution buffer (50 mM

HEPES, pH7.5, 300 mM NaCl, 5 mM DTT, and 18 mM GSH). The eluted protein was then mixed with a GST-TEV and dialyzed against the dialysis buffer (50 mM HEPES, pH7.5, 300 mM NaCl, 5 mM DTT) for overnight at 4 °C. The next day, the GST-TEV, cleaved GST tag and the uncut GST-*Min*Elp3 were separated from the *Min*Elp3 by passing the protein solution to a GSTPrep column. The flowthrough contains the *Min*Elp3 which was subjected to a gel filtration column (Superdex 200) which was pre-equilibrated with the protein storage buffer (20 mM HEPES, pH7.5, 150 mM NaCl, 5 mM DTT). The eluted protein was then aliquot, snap frozen and stored at -80 °C.

Protein expression in insect/baculovirus expression system and purification

DH10Bac E. coli transformation

For bacmid preparation, the DH10Bac *E. coli* strain was used. First, 4 ng of DNA template was added to 100 µL of DH10Bac, then incubated for 30 minutes on ice and afterward subjected to a heat shock at 42 °C for 45 seconds and put again on the ice for 2 minutes incubation. The subsequent step was to add 900 µL S.O.C media (Expo) and incubate bacteria for 4 hours at 37 °C, 200 rpm and then spin down the cells (3000 rpm, 2', RT), resuspend pellet in 100 µl remaining S.O.C and plate it on an agarose plate with the antibiotic mix (50 µg/ml kanamycin, 7 µg/ml gentamicin sulfate, 10 µg/ml tetracycline, 40 µg/ml IPTG (isopropyl β-D-1-thiogalactopyranoside), 100 µg/ml Bluo-Gal, 100 µg/ml ampicillin). Plates were incubated for two days at 37 °C, after which four white colonies were re-streaked on a quarter of the plate and incubated overnight at 37 °C on fresh plates.

Bacmid isolation

Plates were re-streaked, and the content of each was inoculated in 5 ml of LB medium with kanamycin (50 µg/ml), gentamicin sulfate (7 µg/ml), tetracycline (10 µg/ml) for the incubation at 37 °C overnight at 200 rpm. On the following day, cells were spun down (5 minutes, 4000 × g), and resuspended in 0.4 ml resuspension buffer. The cell suspension was then mixed with 0.4 ml lysis buffer and incubated for 5 minutes and followed by addition of 0.4 ml of neutralization buffer (GeneJET Plasmid Miniprep Kit). Next, the mix was incubated on ice for 10 minutes and spun down (14,000 rpm, 10 minutes), and the supernatant was transferred to the fresh and sterile tube with 0.9 ml isopropanol, which was placed on ice for 10 minutes and then at -20 °C for 2 hours. Then the mix was spun down (14,000 rpm, 15 minutes, RT). Next, centrifuged tubes were transferred to the laminar flow hood and washed with 70% ethanol.

Next, the tubes were spun (14000 rpm, 5 minutes, RT), and the supernatant was removed. Then, pellets were dried for 10 minutes under the laminar flow to remove ethanol. Next 40 µL sterile MiliQ water was added to the pellets, and bacmid DNA concentration was measured.

P1 generation – low titer virus

Sf9 (Expression Systems) insect cells were seeded onto six-well plates with 1 million cells per well and incubated for 1 hour at RT. In the meantime, the solutions of 3 µg of each bacmid per 100 µl ESF 921 Insect Cell Media (Expression Systems) and 3 µl FuGENE® HD Transfection Reagent (Promega) per 100 µl media were prepared separately and then mixed and incubated for 30 minutes at RT. After the incubation, the volume of the mix was filled up to 1 ml. Subsequently, 0.5 ml of the medium from the Sf9 cells was removed, and a prepared mix was added to the cells. For the next step, cells were incubated at 27 °C for 4 hours. Next, a fresh cocktail of penicillin and streptomycin (Gibco) was added to the media. The incubation continued for the next four days until the first signs of viral infection. Then the P1 viral medium was collected and filtered.

P2 generation – high titer virus

To increase the virus titer, P2 generation viruses were assembled. First, cells were seeded in T75 flasks in a 15 ml cell medium in the density of 0.4 mln cells/ml and incubated for 1 hour in RT. Then the 7.5 ml of medium was removed, and the transfection medium mix was added. The transfection mix was composed of 0.5 ml medium containing P1 viruses and 7 ml of fresh medium. After four days of incubation, viruses were harvested by collecting the medium from late transfection cells and transferred to the sterile 15 ml tubes, which were centrifuged ($500 \times g$, 7 minutes) and then filtered and stored at 4 °C.

Pull-Down of transfected cells

To check whether transfections were successful, a pull-down test was performed. First, cells were scratched and transferred into a new tube with medium remaining, then the tubes were centrifuged ($400 \times g$, 5 minutes), and the cell membrane was lysed with lysis buffer, after which they were frozen in liquid nitrogen and thawed twice. Next, the lysate was spun down ($14,000 \times g$, 10 minutes) and added to the StrepTrap beads, which were incubated for 1 hour on a spinning wheel at 4 °C. Then, the samples were centrifuged ($500 \times g$, 3 minutes, 4 °C) and washed with 1 ml lysis buffer (this step was repeated thrice). Afterward, a 2x SDS Sample buffer was added to the beads. During the whole procedure, samples from the lysate,

supernatant, and beads were taken and boiled for 5 minutes and then separated on the 12% polyacrylamide gel in SDS running buffer at 180 V for the first 20 minutes and then 220 V until complete gel separation.

Preparation of Baculovirus-infected insect cells (BIICs)

To produce one BIIC vial, 10 million cells in 10 ml were infected with viral particles, where the following formula defined the virus volume:

$$\text{Virus volume} = \frac{\text{Multiplicity of infection (MOI)} \times \text{ number of cells } \times \text{culture volume}}{\text{viral titer}}$$

SuperSf-9-3 (Expression Systems) were cultured at 27 °C for the next 24 hours at 100 rpm. Then they were spun down (5 minutes, 200 × g), and the supernatant was removed. Next, the cell pellet was resuspended in resuspension medium (8.5 ml old medium, 8.5 ml fresh medium, 1.75 ml DMSO (Dimethyl sulfoxide)), then the mix was aliquoted to the cryo-vials and slowly froze in isopropanol at -80 °C. After 2 hours, the vials were transferred to liquid nitrogen for long term storage.

Protein purification from insect cells expression system

For Elp123 protein expression, SuperSf9-3 cells were infected with multiplicity of infection (MOI) = 1 and grown for 3 days at 27 °C on a shaking platform. Subsequently, insect cells were lysed in Lysis Buffer (for Elp123: 50 mM HEPES pH 7.5, 100 mM NaCl, 2 mM DTT, 5% glycerol, DNase I, protease inhibitors; for ELP456: 50 mM HEPES pH 7.5, 150 mM NaCl, 2 mM $MgCl_2$, 2 mM DTT, 5% glycerol, 10 mM imidazole, DNase I, protease inhibitors) by 3 cycles of freezing and thawing in liquid nitrogen and sonication, followed by two-step centrifugation (4 °C; 1 h; 80,000 × g). ELP123 variants were purified using StrepTrap HP 5 ml column (GE Healthcare) eluted in Strep Elution Buffer (50 mM HEPES, 100 mM NaCl, 1 mM DTT, 5% glycerol, 10 mM d-desthiobiotin, pH 7.5), followed by affinity chromatography on HiTrap Heparin HP 5 ml column (GE Healthcare) eluted in a gradient of Heparin Elution Buffer (50 mM HEPES, 1 M KCl, 1 mM DTT, pH 7.5). Finally, eluates were run on Superose 6 Increase 10/300 GL column (GE Healthcare) in 20 mM HEPES pH 7.5, 100 mM NaCl, 5 mM DTT. ELP456 supernatants were purified on IgG agarose beads (Merck) followed by overnight Tobacco Etch Virus (TEV) protease cleavage in Cleavage Buffer (50 mM HEPES pH 7.5, 150 mM NaCl, 2 mM $MgCl_2$, 2 mM DTT). On the next day, the protein sample was applied to a S200 Increase 10/300 GL column (GE Healthcare) equilibrated in 20 mM HEPES pH 7.5, 100 mM NaCl, 2 mM $MgCl_2$, 5 mM DTT. Selected fractions were pooled and

concentrated with on an Amicon Ultra-0.5 (100 KDa cut-off) concentrator. Aliquots were frozen in liquid nitrogen and stored at −80 °C for further use.

tRNA production (In vitro transcription reaction)

The tRNA was produced using the T7 RNA polymerase-mediated run off protocol (T.-Y. Lin et al., 2019). The DNA template contained a T7-promoter sequence and followed by the tRNA sequence. The *in vitro* transcription reaction was performed in 500 μL containing DNA template, T7 RNA polymerase and reaction buffer (20 mM Tris, pH 8.0, 5 mM DTT, 150 mM NaCl, 8 mM $MgCl_2$, 2 mM spermidine, 20 mM NTPs, RNasin, and pyrophosphatase). The reaction was performed at 37 °C overnight and followed by DNaseI treatment to remove DNA templates. The product was then purified using a DEAE column and heat treatment at 80 °C for 2 minutes and followed by a slow cooling process to room temperature as the re-annealing process. To obtain a homogenous tRNA population, the samples were subjected to a S75 Increase gel filtration column and the tRNA containing fractions were pooled and stored at -80 °C. For MST assays, the internally Cy5-labelled *in vitro*-transcribed human tRNAs were produced as mentioned above, where 5% of Cy5-CTP was supplemented in the reaction.

Microscale Thermophoresis (MST)

The Cy5-labelled $tRNA^{Gln}_{UUG}$ (14 or 30 nM) was incubated with serial dilutions of purified *Min*Elp3 or *Hs*Elp123 variants (starting from 1.5 μM) in MST Buffer (20 mM HEPES, 100 mM NaCl, 5 mM DTT, pH 7.5, 0.05% Tween 20) at 4 °C for 30 minutes (T.-Y. Lin et al., 2019). The samples were applied to capillaries (MO-K025, Nanotemper Technologies) and the measurements were performed using Monolith Pico (Nanotemper Technologies) with 60% excitation power at 25 °C. The obtained data were analyzed, and dissociation constant values were calculated using MO.2 Affinity software (Nanotemper Technologies) from at least three independent repeats. The graphs were prepared using Prism v8.0.2 (GraphPad) software.

Electrophoretic Mobility Shift Assay (EMSA)

The reaction was performed as mentioned for the MST measurements. The reaction products were resolved on a 6% native gel at 100 V for 6 h in the cold room. The gel image was obtained using a Typhoon gel scanner and the image was analyzed by ImageQuant (T.-Y. Lin et al., 2019).

Acetyl-CoA hydrolysis assay

Purified *Min*Elp3 or *Hs*ELP123 (0.475 μM) was mixed with 10 μM *in vitro*-transcribed tRNA in presence of 500 μM acetyl-CoA in 1x acetyl-CoA Assay Buffer (MAK039, Sigma) and

incubated in a thermocycler for 30 minutes at 37 °C (T.-Y. Lin et al., 2019). To remove proteins and tRNAs, the samples were passed through a 3 KDa cut-off concentrator (EMD Millipore). The flow-through was collected and subjected to an acetyl-CoA assay kit (MAK039, Merck) for semi-quantitative determination. The reactions were performed according to the manufacturer's instructions. Fluorescence intensity was measured using a plate reader (TECAN) at the probe-specific excitation (535 nm) and emission (587 nm) wavelengths. The measurements for individual conditions were calculated from at least three independent experiments. The graphs were prepared using Prism v8.0.2 (GraphPad) software.

X-ray crystallography and structure refinement

The purified protein solution (15 g/l) was mixed with equal volume crystallization solution (100mM MES, pH 6.3 and 4% PEG 4000) in a hanging drop diffusion method in a 96-well plate. Crystals appeared within 3 days and were snapped frozen in liquid nitrogen.

Pull down assay.

For pull-down experiments, the ELP123WT subcomplexes were immobilized on the Dynabeads MyOne Streptavidin C1 resin (ThermoFischer) via the Twin-Strep-tagged Elp3 protein and incubated with the Elp456 variants for 30 minutes at 4 °C, washed 3 times in Wash Buffer (20 mM HEPES pH 7.5, 100 mM NaCl, 1 mM DTT, 0.05% Tween 20) (Gaik et al., 2022). The ELP456WT subcomplexes were immobilized on Anti-DYKDDDDK (PierceTM) resin via FLAG-tagged ELP6, incubated for 30 min at 4 °C and washed three times in Wash Buffer (same as for Streptactin pull-down). For both pull downs, the proteins were liberated from the beads by heating the sample in SB for 5 minutes at 95 °C before loading the inputs and pull-downs on the SDS-PAGE gels and visualizing by Coomassie staining.

Structure modelling

The predicted virus Elp3 protein models were obtained using Swiss-model and Phyre2 (Kelley et al., 2015; Waterhouse et al., 2018). The predicted human ELP1, ELP2 and ELP3 protein atomic models were obtained from the online prediction software AlphaFold2 (AF-O95163-F1, AF-Q61A86-F1, AF-Q9H9T3-F1) (Jumper et al., 2021; Varadi et al., 2022). The individual model was fitted into the yeast Elp123 density (PDB: 6qk7) using Chimera (version 1.2). The tRNA (PDB: 1ehz) was taken from the Protein Data Bank and fit into the human Elongator based on the yeast tRNA fit. The analysis of ELP1 Lys815 was performed using the density and model of the ELP1 C-terminus (PDB: 5CQR) determined by crystallography. The analysis

and figures were performed using Pymol, the Molecular graphics system (version 2.0 Schrödinger, LLC).

Cryo-EM sample preparation and single particle analysis

Sample preparations for cryo-EM were carried out in a similar method to that previously described (Dauden et al., 2019). In brief, freshly prepared proteins (0.6 g/l) without or with RNAs (4-times excess) was prepared in binding buffer (20 mM HEPES, pH 7.5, 100 mM NaCl, 2 mM MgCl2, 2 mM DTT) and applied to glow-discharged holey carbon grids (Quantifoil) with a thin amorphous carbon film of around 10 nm thickness over the holes and incubated for 15 s at 4 °C and 100% humidity followed by blotting and plunge freezing. Grid screening and data collection were carried out at the Solaris Synchrotron, Krakow, Poland. Data was collected using a transmission electron cryo-microscope (FEI Titan Krios 3Gi) operated at an accelerating voltage of 300 kV equipped with Falcon III and K3 direct detectors. Particles were picked using built-in feature in CryoSPARC (Punjani et al., 2017), including blob picker and template picker, combining with TOPAZ training (Bepler et al., 2020; Rubinstein & Brubaker, 2015; Zheng et al., 2016; Zivanov et al., 2020). The picked particles were subjected to 2D and 3D classifications (in CryoSPARC or RELION) to remove junk particles and the rest were processed for 3D reconstruction. Subclassification was performed, and the best class was further refined. The models obtained from existing PDB or AlphaFold prediction were fitted into the density using Namdinator for dynamic fitting (Jumper et al., 2021; Kidmose et al., 2019; Varadi et al., 2022). The models will be further refined using Phenix for real-space refinement (Adams et al., 2010). The structures were visualized using Pymol or ChimeraX (The PyMOL Molecular Graphics System, Version 2.0 Schrödinger, LLC, (Pettersen et al., 2004).

Materials

Chemicals and consumables

Chemical/consumable	Company
2-Propanol	VWR
30% Acrylamide/Bis-acrylamide solution	Roth
Acetic acid	POCH
Agar	Lab Empire
Agarose	Lab Empire
Amicon® Ultra Centrifugal Filters (3K, 30K)	Merck Millipore
Ammonium persulfate (APS)	Roth
APM	LGC Standards
Bolt™ 4–12% Bis-Tris Plus Gels	Thermo Fisher Scientific
Bromophenol blue	Sigma-Aldrich
Cell culture flasks (T25, T75)	VWR
Cell culture multiwell plates (6-well, 12-well, 24-well, 96-well)	VWR
Coomassie brilliant blue	BioShop Canada Inc
DMSO	Corning
DNA Gel Loading Dye (6X)	Thermo Fisher Scientific
dNTP Mix (10 mM each)	Thermo Fisher Scientific
DTT	Lab Empire
Dynabeads™ MyOne™ Streptavidin C1	Thermo Fisher Scientific
EDTA	POCH
Ethanol	VWR
FBS	EurX
GeneRuler™ 1kb DNA Ladder	Thermo Fisher Scientific
Glycerol	VWR
Glycine	Lab Empire
HEPES	Lab Empire
HiTrap Heparin	GE Healthcare
HiTrap Q	GE Healthcare
Imidazole	ROTH
IPTG	DNA Gdańsk

Lithium chloride	Acros Organics
Magnesium chloride	POCH
Methanol	VWR
NiNTA	Qiagen
Nuclease free water	sigma
PageRuler™ Prestained Protein Ladder	Thermo Fisher Scientific
Pasteur pipettes	Lab-Szkło
PBS w/o Mg^{2+} & Ca^{2+}	Lonza
PCR tubes	VWR
PEI	Sigma-Aldrich
PES syringe filters (0.2 μm, 0.45 μm)	VWR
Phusion GC Buffer Pack	Thermo Fisher Scientific
Phusion HF Buffer Pack	Thermo Fisher Scientific
Pipette tips	Lab Empire
Potassium chloride	Sigma-Aldrich
Protease Inhibitor Cocktail	Sigma-Aldrich
qPCR Sealing film	Brand
Sensors for cell counting	Merck Millipore
Sodium chloride	Lab empire
Sodium deoxycholate	VWR
Sodium dodecyl sulfate	Roth
Sodium hydroxide	VWR Chemicals
Sterile conical tubes (15 ml, 50 ml)	Sarstedt
Sterile cryotubes	VWR
Sterile serological pipettes	Equimed
Sucrose	Lab Empire
Superdex 200 column	GE Healthcare
SYBR™ Safe DNA Gel Stain	Thermo Fisher Scientific
TAE buffer (50X)	VWR
TCEP	Sigma-Aldrich
TEMED	Sigma-Aldrich
TRIS base	Lab Empire
Triton X-100	BioShop Canada Inc

Tween 20	Lab Empire
Urea	BioShop Canada Inc
β-Mercaptoethanol	Lab Empire

Technical devices

Technical devices	Company
Cell counter	Merck Millipore
Centrifuge 5427 R	Eppendorf
Centrifuge 5804 R	Eppendorf
Chamber for agarose gels	Bio-Rad
ChemiDoc™ XRS+ imaging system	Bio-Rad
Digital rotator	IKA
Freezing container	Thermo Fisher Scientific
Incubator for bacteria plates	Pol-Eko-Aparatura
Incubator for eukaryotic cells	New Brunswick
Laminar flow hood	Faster
Microplate reader	Tecan
Microwave	Zelmer
NanoDrop spectrophotometer	Thermo Fisher Scientific
Optical microscope	Nikon
Orbital shaker	Thermo Fisher Scientific
pH meter	Mettler-Toledo
Pipetor	HTL
Pipettes	Lab Empire
Q Exactive orbitrap mass spectrometer	Thermo Fisher Scientific
Rocking shaker	Biosan
Scale	Ohaus
Sonicator	Hielscher Ultrasound technology
Thermal block	Thermo Fisher Scientific
Trans-Blot Turbo Transfer System	Bio-Rad
Water bath	GFL

Homemade buffers

Buffer	Components
Sample buffer (6X)	375 mM Tris-HCl pH 6.8, 10% SDS, 48% glycerol, 150 mM DTT, 0.03% bromophenol blue
SDS Running buffer (10X)	250 mM Tris base, 1.9 M glycine, 1% SDS
KCM buffer (5X)	500 mM KCl, 150 mM CaCl2, 250 mM MgCl2

Results

In the first section, I will present my results that contributed to the structural and functional characterization of Elp3 found in viruses, bacteria, archaea, and the comparison to yeast Elp3. My work on the eukaryotic Elongator complex, more precisely the Human elongator complex and its comparison with the yeast and mouse complexes will be described in the second section.

Part I - Non-eukaryotic Elp3

Study of bacterial Elp3

Figure 12. Sequence conservation of Elp3. Highlighted in yellow are the three eukaryotic ELP3 protein sequences (*Homo sapiens* (Hs), *Mus muculus* (Mm) and *Saccharomyces cerevisiae* (Sc)), in lavender is an archaeal Elp3 *Methanocaldococcus infernus* (Min), in green the bacteria *Dehalococcoides mccarty* (Dmc) and in pink are the viral species (Bodo saltran virus (BsV), Aurococcus anophagefferens virus (AaV), Phaeocytus globosa virus (PgV), Klosneuvirus (Klo), Pithovirus (PitV) and Cafeteria roenbergis virus (CroV)). The sequence similarity was calculated using MUSCLE. The SAM domain is circled in a mint-green box and the KAT domain is in a coral box.

First, I retrieved the amino acid sequences of the ORFs from selected Elp3s in the UniProt and NCBI databases (Bateman et al., 2021; Sayers et al., 2022), including bacteria (A0A1C7D1B7), archaea (D5VRB9) and eukaryotes (Q02908, Q9CZX0 and Q9H9T3). Elp3 is also found in viruses (Bäckström et al., 2019a; Deeg et al., 2018; Fischer et al., 2010; Moniruzzaman et al., 2014; Schulz et al., 2017; Selvadurai et al., 2014) (YP_009052437.1, ATZ80694.1, YP_008052718.1, ARF12340.1, QBK91503.1 , YP_003970024.1). Therefore, I included six out of over sixty predicted Elp3 sequences of Megaviruses from metagenomic work in water fractions in different oceans. The sequence alignment (Figure 10) was performed using MUSCLE (Madeira et al., 2022) and the identity threshold was set to 50%. The secondary structure topology of Elp3 is shown based on the *Dmc*Elp3 crystal structure (Glatt et al., 2016) (Figure 11). All Elp3s share a common core structure and contain two conserved functional domains, namely rSAM and KAT, but display different N-termini. The central linker is located between rSAM and KAT domains.
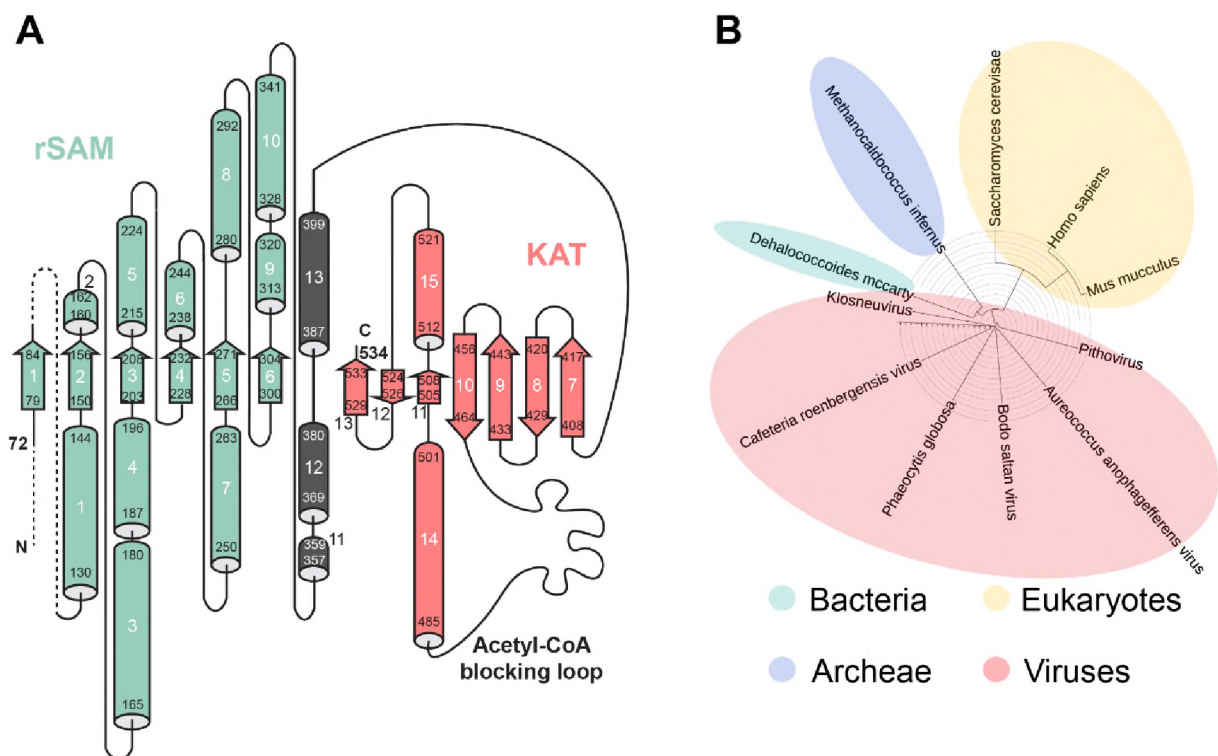
Figure 13. **Overview of Elp3.** A. Topology model of MinElp3 indicating secondary structure elements. (T.-Y. Lin et al., 2019, modified) B. Phylogenic tree showing distances between the previously aligned sequences using the EMBL iTOL.

According to the sequence alignment, the sequences show different degrees of sequence identity and similarity when compared to the human ELP3. For instance, the sequence identity of *Dmc*Elp3, *Min*Elp3, *Sc*Elp3, and *Mm*Elp3 to human ELP3 are 41.4%, 43.7%, 77.5% and 95.8%, respectively. Elp3 from Megaviruses are less conserved to human ELP3 (ranging from 30.5 to 33.3%). These results indicate that the Elp3 sequence is overall conserved among all

domains of life and viruses, and the latter ones are the least conserved, which is in line with the phylogenetic tree analysis based on their amino acid sequences (Figure 11B). Of note, some viruses have additional stretches (unstructured regions) in each domain, including rSAM and KAT domains, and contain extra-long C-termini. The C-termini in some viruses (*Phaeocytus globosa* virus, *Klosneuvirus* and *Aurococcus anophagefferens* virus) are annotated as transmembrane domains from the secondary structure predictions by Phyre2.

The different lengths and extremely low sequence similarity of various N-termini is an
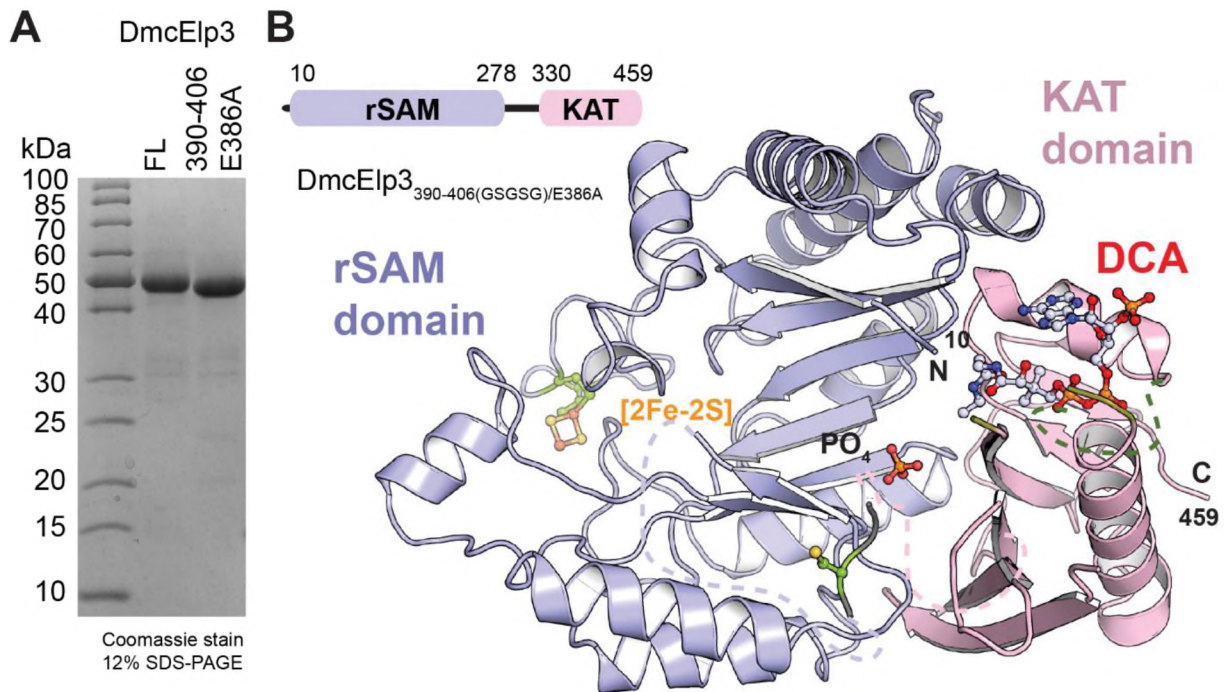
Figure 14. **Characterization of *Dmc*Elp3**. A. SDS-PAGE showing the purity of full-length Elp3 and DmcElp3$_{390-406(GSGSG)}$/E386. B. Cartoon representation of structures of SAM in light blue and KAT light pink in *Dmc*Elp3. The bound DCA, iron-sulfur and the cysteines (green) for iron-sulfur binding are shown in balls and sticks (PDB: 6IA6). (T.-Y. Lin et al., 2019, modified). The domain elements are shown as an inset.

interesting (and surprising) feature and an active area of research. In particular, the bacterial *Dmc*Elp3 has only 10 amino acids at its N-terminus, while other species have around 60-70 residues in this region, constituting an intriguing difference. Furthermore, there are several lysine and arginine residues in this stretch, suggesting a possible role in nucleic acid binding (i.e., recognition of specific DNA or RNA sequences). A closer study of this region could provide further insight into the roles of the various N-termini and their interaction with nucleic acids, foremost substrate tRNAs. It may also help to explain some of the differences between the bacterial and eukaryotic proteins.

There are several conserved residues in each domain and some of them are crucial according to the *in vivo* analyses using yeast as a model organism (performed by Glatt et al. Glatt et al. 2016). For instance, an iron/sulphur coordinating loop (CXCXXC) is present in all rSAM domain of Elp3s. Substitutions of these residues result in phenotypes in yeast that can be related to the tRNA modification activity of Elongator. To further explore structural details of Elp3, its biochemical activities and chemical reaction, I focused on producing the bacterial and archaeal Elp3 instead of yeast Elp3, which has been shown to be difficult to purify and to obtain reasonable quantities for biochemical characterizations (Glatt et al. 2016). Of note, despite extensive efforts on producing viral Elp3s, I did not manage to purify any of them. It seems that the proteins are intrinsically unstable which could be due to their additional unstructured regions.
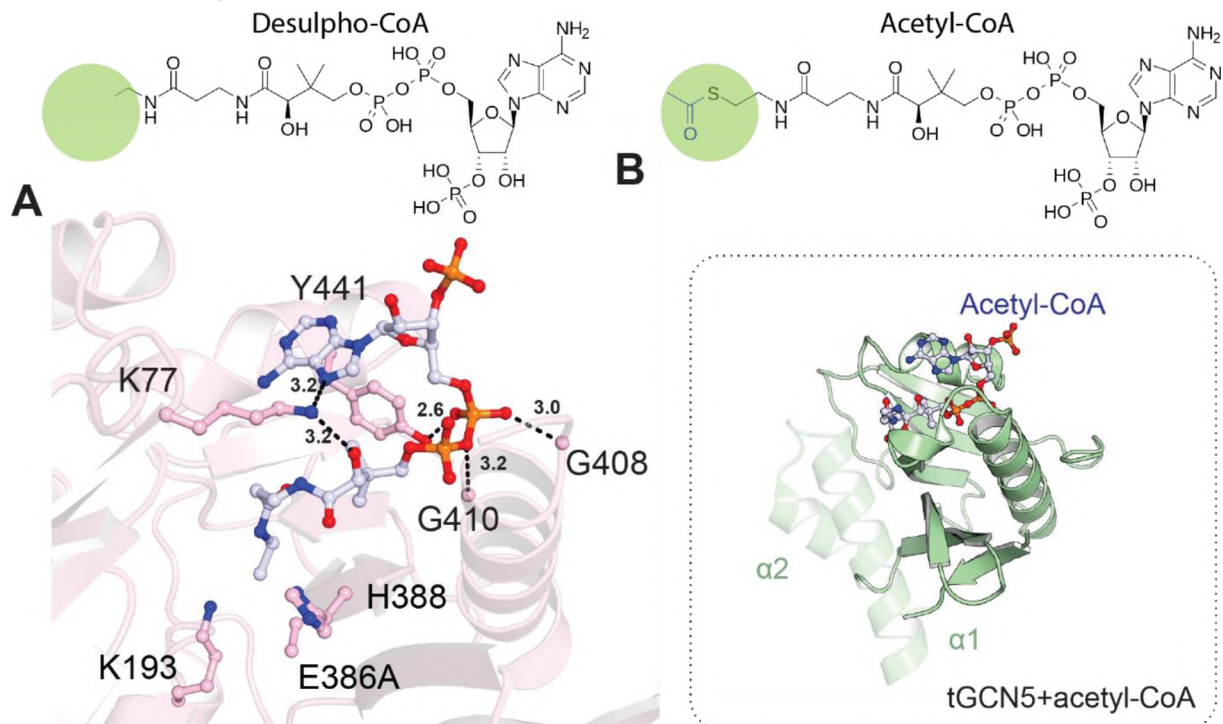
Figure 15. **Desulpho-CoA bound structure of Elp3.** A. Chemical formula of DCA and DCA bound structure of *Dmc*Elp3 (PDB: 6IA6) B. ACO chemical formula and ACO bound structure of tGCN5 (PDB: 1QSR).

I produced *Dmc*Elp3 and *Min*Elp3 using a bacterial overexpression system. *Dmc*Elp3 and *Min*Elp3 were initially inserted into a pETM30 vector so that the desired proteins of interest can be produced as a GST fusion with a purification tag. The purification procedure of *Dmc*Elp3 and *Min*Elp3 was conducted using affinity columns followed by TEV cleavage of the GST fusion. An additional step using heparin column purification was necessary for *Min*Elp3 to minimize nucleic acid contaminations from the protein prep. Subsequently, the proteins were further subjected to a gel filtration column to obtain the pure proteins (Figure 12A). It is worth noting that the purified recombinant *Dmc*Elp3 protein occurs in two forms:

monomer and dimer. The latter form is held together by an iron/sulphur cluster. The dimeric form appears reddish, while its monomeric counterpart is transparent, showing that the monomer has negligible or no iron content. The acetyl-CoA binding loop truncation (DmcElp3390-406(GSGSG)) was used by my colleagues to set up crystallization trials (Figure 12B). The Desulpho-Coenzyme A (DCA) bound structure of DmcElp3390-406(GSGSG)/E386A also had a E386A mutation which is located in the active site of the ACO binding pocket (Figure 13A), which might trap the molecule in its binding site (Glatt et al., 2016) (Figure 13). The DCA bound structure is highly similar to the ACO binding in the GCN5 protein (PDB: 1QSR) (Figure 13B).
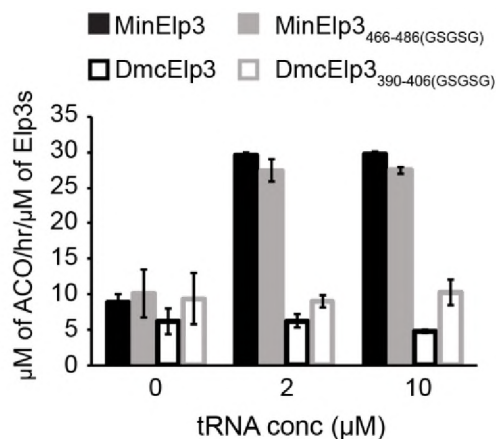
Figure 16. **Conserved role of the ACO blocking loop.** ACO hydrolysis rates of DmcElp3 compared to MinElp3 and their respective ACO loop truncations. (T.-Y. Lin et al., 2019, modified).

Next, I aimed to set up *in vitro* assays that could directly monitor enzymatic activities of Elp3, including tRNA-triggered ACO hydrolysis and tRNA binding. However, DmcElp3 seems to be insensitive to tRNA binding as its ACO hydrolysis does not change upon tRNA binding, although it can interact with tRNA (Glatt et al., 2016). On the other hand, MinElp3 indeed shows tRNA-induced ACO hydrolysis in my assay (Figure 14), which confirms published data (Selvadurai et al., 2014). I then decided to focus on the archaeal Elp3 protein and investigated its activity as a model protein for in-depth characterizations. Of note, the archaeal species *Min* is found in hydrothermal deep-sea vents at a depth of 3000 meters and temperatures of 85 °C. Many recombinantly expressed proteins from thermophilic species are often thermostable and easier to produce. This might also facilitate crystallization of these proteins.

46

Structural and biochemical characterization of MinElp3
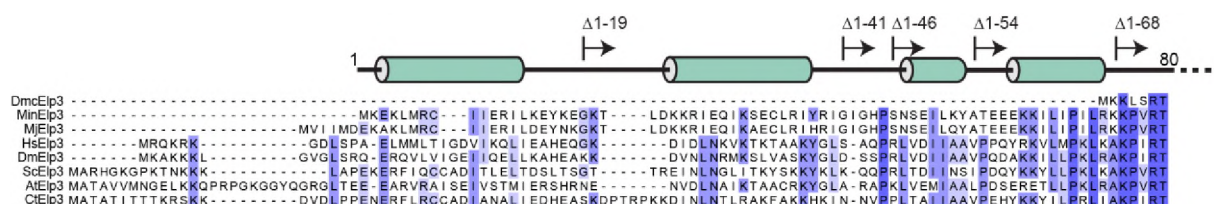
Crystallization trials of MinElp3

Figure 17. **Sequence Alignment of Elp3 N-termini**. Comparison of sequences from Dehalococcoides mccarty, Methanocaldococcus infernus, Methanocaldococcus jannaschii, Homo sapiens, Drosophila melanogaster Saccharomyces cerevisiae, Arabidopsis thaliana and Chaetomium thermophilum using MUSCLE alignment. Above it is the representation of the alpha helices of MinElp3 and the position of the truncations. (T.-Y. Lin et al., 2019, modified).

The production of *Min*Elp3 followed the same purification protocol and the obtainable yield is high and sufficient for crystallization trials (*Dmc*Elp3: 30 mg from 1 L culture; *Min*Elp3: 5 mg from 1 L culture). Interestingly, the gel filtration profile of *Min*Elp3 shows that *Min*Elp3 only exists as a monomer and the protein solution appeared transparent (Figure 15). Despite the high purity and homogeneity of the protein preps, I had no success in obtaining crystals. Even after various modifications to the conditions, such as altering the protein concentration (7.5, 12 or 15 mg/ml), salt concentration, temperature and including additives. A secondary structure analysis of *Min*Elp3 suggests that the extended N-terminus could hamper crystal formation. Therefore, the transactions of *Min*Elp3 N-terminus might overcome the problem. Based on the secondary structure prediction using Phyre2, the truncation sites may maintain the secondary structure elements (Figure 15). These truncations at the N-terminus of *Min*Elp3, namely *Min*Elp3$_{G20-543}$, *Min*Elp3$_{G20-543}$, *Min*Elp3$_{G20-543}$, *Min*Elp3$_{G20-543}$, *Min*Elp3$_{G20-543}$, were produced using the same purification procedure as described above. The gel filtration profiles of these
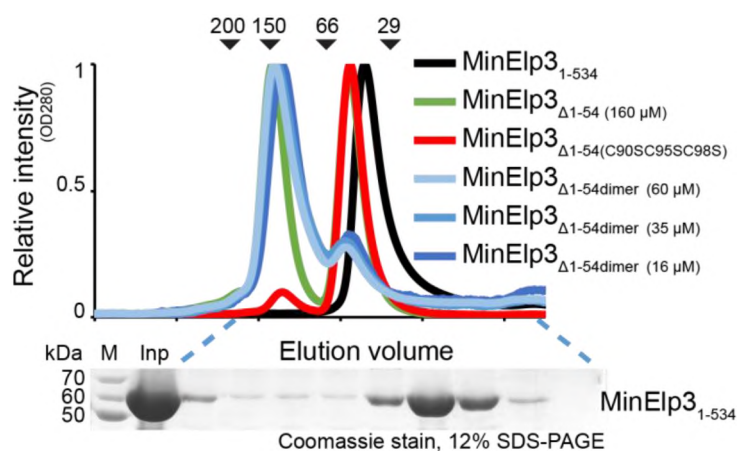

Figure 18. **Protein expression profiles of MinElp3 WT and mutants.** S200 gel filtration profile of MinElp3 WT in black and different concentrations of mutant. The Eluted fractions were resolved by 12% SDS-PAGE and visualized by Coomassie staining. (T.-Y. Lin et al., 2019, modified).

47

truncated proteins show that surprisingly they exist in dimeric and monomeric forms as observed for *Dmc*Elp3 (Figure 15). In addition, the dimeric forms of all truncated proteins displayed a pink color, which is likely caused by the coordination of an iron-sulphur cluster. Of note, the full-length *Min*Elp3 eluted from the gel filtration earlier than other truncated forms. Next, RALS (Right Angle Light Scattering) measurements were performed, which confirmed the molecular weight of full length *Min*Elp3 (~55 KDa). This atypical profile indicates that the conformation of the protein is different than the one of the truncated versions.

Given that the dimer form of *Dmc*Elp3 is stabilized by the coordination of an iron-sulphur cluster, the dimer formation of the N-terminal truncated *Min*Elp3s could be due to the same reason as for *Dmc*Elp3. Hence, I then generated cysteine to serine mutation at the iron-sulphur cluster residues. Interestingly, the *Min*Elp3$_{C90-95-98S}$ mutant, having transparent solution, exhibits a similar gel filtration profile as *Min*Elp3 wild-type, confirming that the dimeric form depends on the iron/sulphur cluster (Figure 16).
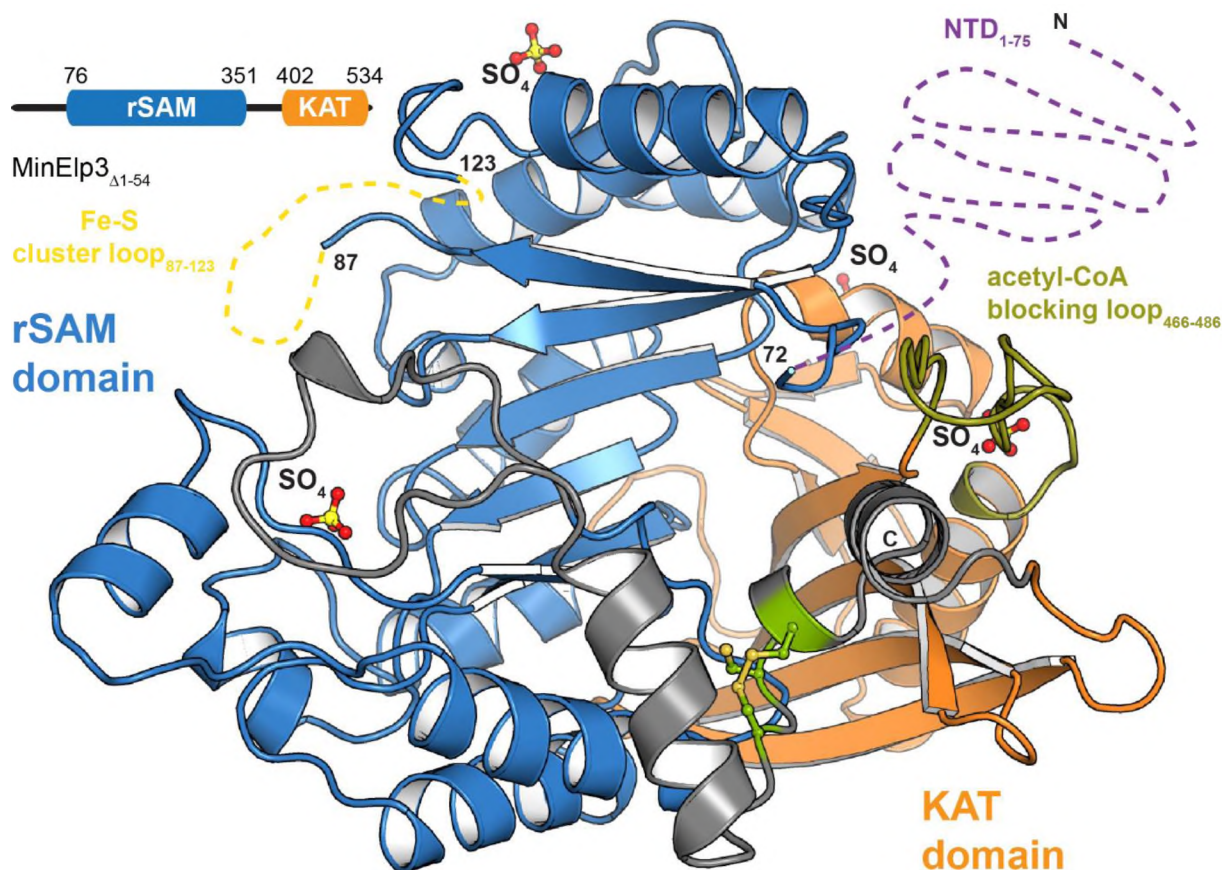

Figure 197. **Characterization of *Min*Elp3.** Scheme of SAM domain in blue and KAT domain in orange in *Min*Elp3 and structure of *Min*Elp3$_{\Delta1-54}$ (6IAD). (T.-Y. Lin et al., 2019, modified).

Although the crystallization trials with full length *Min*Elp3 failed, I continued the trials with the truncated forms. Strikingly, all five truncated proteins formed crystals in various

crystallization conditions. I optimized the original hit conditions and selected the conditions with the most defined crystals for data collections. In the meantime, I set up several crystallization trials to screen for *Min*Elp3 with DCA or *Min*Elp3 with full length tRNA (*Dmc*-tRNA[Glu]). However, all these extensive screenings failed. Several crystals of truncated *Min*Elp3 were obtained and I worked with a colleague and solved the structures of monomeric *Min*Elp3$_{\Delta1-19}$, *Min*Elp3$_{\Delta1-46}$, and *Min*Elp3$_{\Delta1-54}$, using a poly-alanine model of *Dmc*Elp3 for molecular replacement, at 1.9 Å (PDB: 6IA6) (Figure 16), 1.9 Å (PDB: 6IAZ), and 2.1 Å (PDB: 6IAD) resolution, respectively (Figure 17).
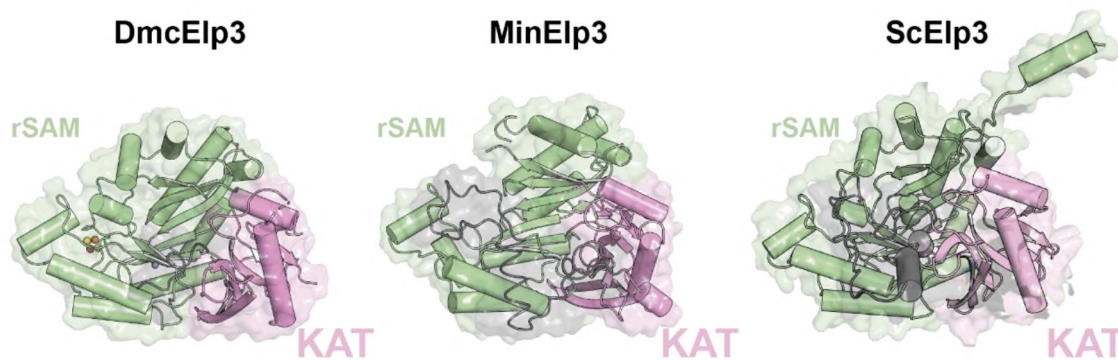
Figure 208. **Domain arrangement in all Elp3 structures obtained.** Comparison of crystal structure from *Dmc*Elp3 (PDB: 5L7J) and *Min*Elp3(PDB: 6IAD) to cryoEM structure of *Sc*Elp3 (PDB: 6QK7). rSAM domain shown in pale green and KAT domain shown in pale pink. (Abbassi et al.2020, modified)

The solved *Min*Elp3 structures are almost identical to *Dmc*Elp3 (Glatt et al., 2016) and *Sc*Elp3 (Dauden et al., 2019). For instance, the domains of KAT and rSAM join by an extended interaction interface and form a cleft for tRNA binding (Figure 18). The loop responsible for iron/sulphur cluster in rSAM domain as well as the iron/sulphur cluster are not visible in any of the *Min*Elp3 structures. Furthermore, the N-termini of the three truncations are still not visible, indicating high flexibility of this region. Interestingly, the ACO loop at the ACO binding site is visible due to crystal contacts with the neighboring *Min*Elp3 molecule. To obtain the co-crystal structure of *Min*Elp3 and DCA, I produced a similar ACO loop deletion in *Min*Elp3 (MinElp3$_{466-486(GSGSG)}$), where a GSGSG liner was placed to maintain the local structure. To be sure that the truncation does not affect the structure and activity, I performed ACO hydrolysis assays with this protein. Compared to the wild-type, the MinElp3$_{466-486(GSGSG)}$ display similar tRNA-triggered ACO hydrolysis rates (Figure 14). However, there was no success in obtaining crystals.

The expected iron-sulphur cluster is not observed in the *Min*Elp3 crystal structure, suggesting that the purification procedure under aerobic conditions may have led to its absence.

To restore the cluster, an established reconstitution assay under anaerobic condition was performed. To confirm the presence of the cluster, the reconstituted *Min*Elp3 was then measured using EPR. Unfortunately, the results did not show any sufficient signatures that could indicate the presence of the iron-sulphur cluster, suggesting that further experimentation is needed. In summary, Elp3s from bacteria, archaea and yeast are structurally conserved proteins. The N-terminus of Elp3 is flexible and to date its structure is only observed in the cryo-EM structure of *Sc*Elp123 bound to tRNA, which explains the difficulty in obtaining crystals with the full length *Min*Elp3. Further research on the iron-sulphur reconstitution of *Min*Elp3 will provide more insight into the nature of the iron-sulphur cluster and its interaction with *Min*Elp3, which may be useful in understanding the structure and function of the enzyme.

Characterization of *Min*Elp3-tRNA interaction

After successfully determining the *Min*Elp3 crystal structure, I next aimed to obtain the tRNA-
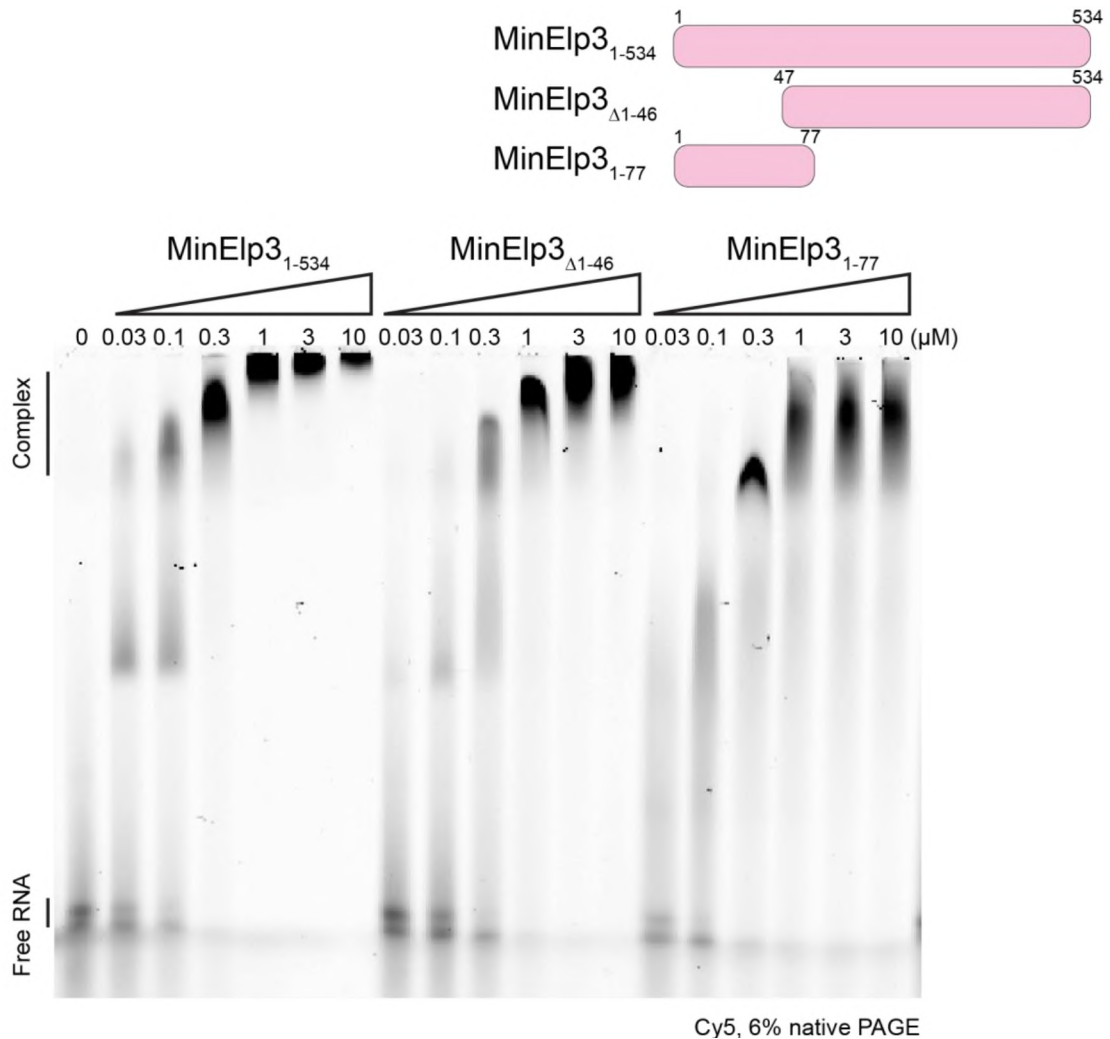
Figure 19. **tRNA affinity of MinElp3 N-terminus**. EMSA showing the affinity to tRNA of full-length *Min*Elp3, MinElp3$_{\Delta1-46}$, and *Min*Elp3 $_{1-77}$. Above is a schematic representation of the truncations studied (T.-Y. Lin et al., 2019, modified).

*Min*Elp3 complex structure. First, I investigated the ability of wild-type and the N-terminal truncated versions to interact with tRNA. I used an Electrophoresis mobility shift assay (EMSA), which resolves the proteins and protein-tRNA complexes on a native gel, where proteins can retain their natural shape and net charge. A titration of protein concentration was used against a constant amount of labelled tRNA in each condition (Figure 19). I first compared the *Dmc*-tRNA^{Glu} affinity to the full-length *Min*Elp3, the N-terminal truncation of *Min*Elp3 or the Elp3 N-terminus alone. While the measured affinity of full-length *Min*Elp3 is 0.3 μM, the N-terminal truncation of *Min*Elp3 shows lower affinity (1 μM). Interestingly, the N-terminal fragment of *Min*Elp3 retains a similar tRNA affinity to the full-length protein.

To obtain a quantitative K_D for proteins, the microscale thermophoresis (MST) method was used (Figure 20A). This assay is based on the detection of fluorescence signals from a labelled binding target (Cy5-tRNA) and the measurement monitors changes in the signals that correspond to the free and bound states upon the creation of a thermal gradient. *Dmc*-tRNA^{Glu} was used in the interaction. The calculated K_D profiles indicate that in general the interaction strength decreases as the N-terminus becomes shorter. In detail, the affinity of full-length *Min*Elp3 for the tRNA is about 50 nM, which then decreased to 210 nM for *Min*Elp3$_{\Delta 1-19}$, 980 nM for *Min*Elp3$_{\Delta 1-41}$, 1410 nM for *Min*Elp3$_{\Delta 1-46}$, 580 nM for *Min*Elp3$_{\Delta 1-54}$ and 660 nM for *Min*Elp3$_{\Delta 1-68}$. Furthermore, the loss of the N-terminal region has a consequence in losing the tRNA-induced ACO hydrolysis activity (Figure 20B).
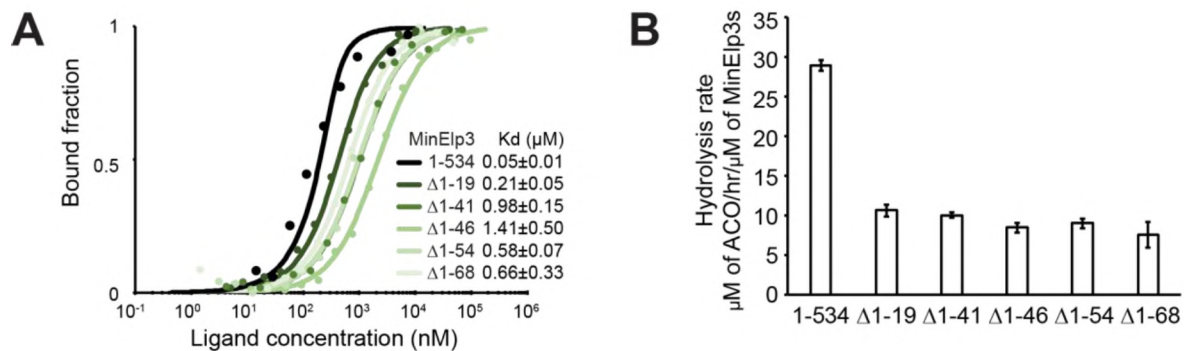
Figure 20. **Enzymatic activity of N-termini truncated proteins**. A. MST analysis of *Min*Elp3 N-terminus truncations. The curves are color coded. B. ACO hydrolysis rate of full-length *Min*Elp3 and N-terminus truncations (T.-Y. Lin et al., 2019, modified).

Although the sequences of N-termini in all Elp3s are not conserved, they all contain multiple lysine and arginine residues which can be implicated in direct nucleic acid interactions. To understand if the N-terminal domain of Elp3 from eukaryotes performs the same function as the archaeal Elp3, I generated a "chimeric" *Min*Elp3, where the N-terminus of *Min*Elp3 was replaced with the N-terminus of either human or yeast Elp3 (Figure 21). The hybrid Elp3s were subjected to further analysis of tRNA binding and tRNA-induced ACO hydrolysis. Using *Dmc*Elp3 and MinElp3$_{\Delta 1-68}$ as low binding controls (respective K$_{DS}$ of 1410 nM and 660 nM), we see that *Sc-Min*Elp3 and *Hs-Min*Elp3 both bind tRNA with a K$_D$ of 140 nM. On the one hand, this data clearly shows that both eukaryotic N-terminal domains restore the tRNA binding activity. On the other hand, the tRNA-triggered ACO hydrolysis activity was not recovered, which could hint towards a different mechanism being triggered between non-eukaryotes and eukaryotes. The more obvious point is that the addition of a longer and foreign N-terminus to *Min*Elp3 is probably interfering with the displacement of the ACO blocking loop. Overall, these results indicate the functional role and importance of the N-terminal region in tRNA recognition and the enzyme-mediated modification reaction.
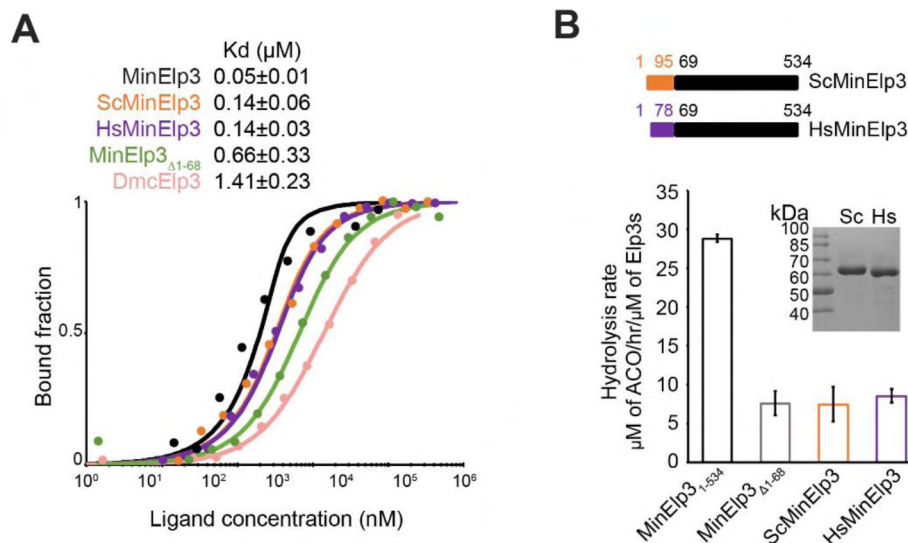

Figure 231. **Enzymatic activity of chimeric Elp3**. A. MST analysis of *Min*Elp3 and *Dmc*Elp3 together with *Min*Elp3 $_{\Delta 1-68}$ N-terminus truncations and rescue proteins of N-terminus of *Hs*ELP3 and *Sc*Elp3 combined to *Min*Elp $_{\Delta 1-68}$. B. Scheme of chimeric constructs above the acetyl-CoA hydrolysis rate of *Min*Elp3 WT and recombinant proteins (T.-Y. Lin et al., 2019, modified).

Given that *Min*Elp3 possesses tRNA binding ability, the next questions to be addressed are related to its substrate specificity. I performed the MST assays to measure the K$_D$ of *Min*Elp3 toward various tRNA species. First, MST results show that the tested tRNAs, such as *Dmc*-tRNA$^{Glu}_{UUC}$, *Sc*-tRNA$^{Cys}_{GCA}$, *Sc*-tRNA$^{Glu}_{UUC}$, and *Sc*-tRNA$^{Ser}_{UGA}$, are bound by the protein with similar affinity (Figure 22). Among the tested tRNAs, *Sc*-tRNA$^{Cys}_{GCA}$ harbors a G34 instead of U$_{34}$ and still shows the comparable affinity to Elp3, indicating Elp3 does not

distinguish modifiable (containing a U_{34}) and non-modifiable tRNA (without U_{34}). Moreover, *Min*Elp3 seems to display a greater affinity for tRNAs with a CCA end in the case of tRNA$^{Ser}_{UGA}$ with (K_D 60±50 nM) and without CCA end (K_D 370±110 nM). This suggests that either the protein can interact more effectively with the CCA 3' end of the tRNA or the extended tRNAs is able to fold to a more preferable structure for binding.

Elp3, initially identified as histone acetyltransferase, was further tested for its affinity to histone H3. I used a peptide containing the modifiable lysine14 in the histone H3 tail and measured the affinity toward Elp3 (Figure 22). The results show no interaction between the peptide and the protein. Because the binding curve does not reach saturation, the K_D cannot be calculated – it is thus marked as > 10 µM.
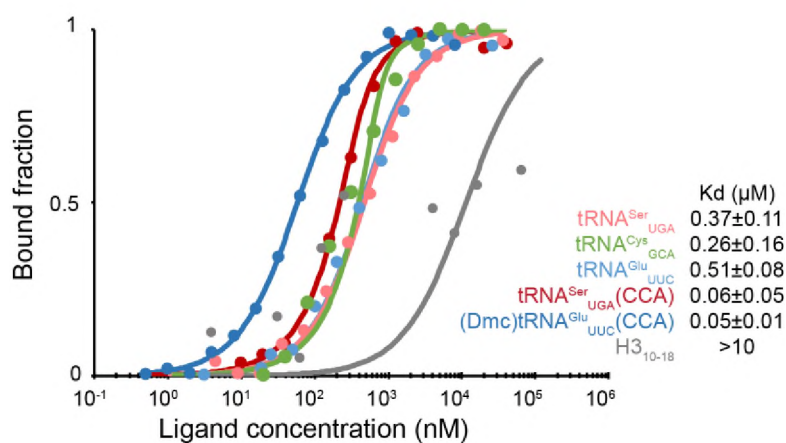
Figure 242. **tRNA selectivity of *Min*Elp3**. MST analysis of *Min*Elp3 with the unmodifiable in-vitro-transcribed *Sc*-tRNA^{Cys}, the two modifiable *Sc*-tRNAs^{Ser} and *Sc*-tRNAs^{Glu}, the modifiable and with 3'CCA sequence *Sc*-tRNAs^{Ser} and *Dmc*-tRNAs^{Glu} and the histone H3 peptide. The tested samples are color-coded and the calculated K_{Ds} are listed in inset.

Based on the affinity profiles of Elp3 with tRNAs, I selected the best complex (with strongest affinity) of full-length *Min*Elp3 and *Dmc*-tRNA^{Glu} for setting up subsequent crystallization trials. Despite extensive trails (various concentration and crystallization conditions) no crystals appeared. As the full-length tRNA in the complex with *Min*Elp3 might intervene with the crystal formation, performing co-crystallization trials with a truncated tRNA (e.g., the anti-codon stem loop of tRNA (19 nt)) can be an alternative option. Before setting up the co-crystallization trails, suitable short tRNA binders should be screened. I firstly monitored the affinity of *Min*Elp3 to ASL of *Sc*-tRNA^{Ser} using EMSA (Figure 23). The profile shows that the affinity to ASL of *Sc*-tRNA^{Ser} is 1 µM, which is weaker than for the full-length *Sc*-tRNA^{Ser} (K_D 0.3 µM). I also tested a 9-mer polyU chain which displays even weaker binding than that of the ASL of *Sc*-tRNA^{Ser}, suggesting the structured element is favored for interaction. In addition, the interaction of the ASL of *Sc*-tRNA^{Ser} with the N-terminal truncated *Min*Elp3 is

the worst, proving the necessity of the N-terminus for binding. Nonetheless, there was still no success in obtaining crystals for the ASL-*Min*Elp3 complex.
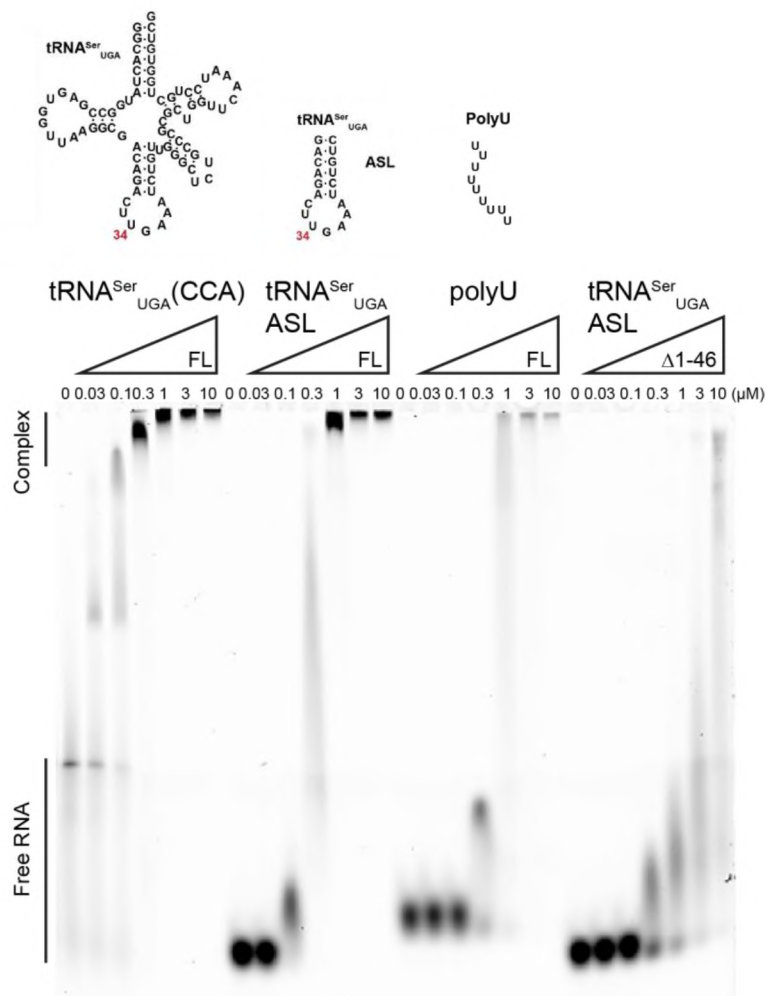

Figure 253. ***Min*Elp3 affinity to short RNA**. EMSA showing the affinity to tRNA of *Min*ElpWT to the anticodon stem and loop (ASL) of *Sc*-tRNA[Ser] and Poly-U. The last quarter of the gel shows the affinity of the tRNASer ASL to *Min*Elp3[Δ1-46] (Lin et al., 2019, modified).

To understand whether the ACO binding mechanism is conserved, I investigated the potential ACO binding residues in MinElp3. Based on the sequence alignment and structural alignment between *Dmc*Elp3 and *Min*Elp3, several conserved residues were identified and mutated for subsequent biochemical characterizations (Figure 24). These mutations include *Min*Elp3$_{K150A}$, *Min*Elp3$_{K266A}$, *Min*Elp3$_{Q461A}$, *Min*Elp3$_{H463A}$, and *Min*Elp3$_{Y517A}$. First, I confirmed the mutations on these residues do not affect their ability to bind tRNA and their affinities. Next, these mutants were tested for ACO hydrolysis. Most mutations, including *Min*Elp3$_{K150A}$, *Min*Elp3$_{K266A}$, *Min*Elp3$_{Q461A}$, and *Min*Elp3$_{Y517A}$ showed dramatically reduced tRNA-triggered ACO hydrolysis rates while *Min*Elp3$_{H463A}$ shows no effect. In addition to the point mutations, the ACO loop truncation of *Min*Elp3 was also tested in the MST assay and confirmed that it retains tRNA binding at wild-type levels, meaning that the loop does not influence initial tRNA binding.
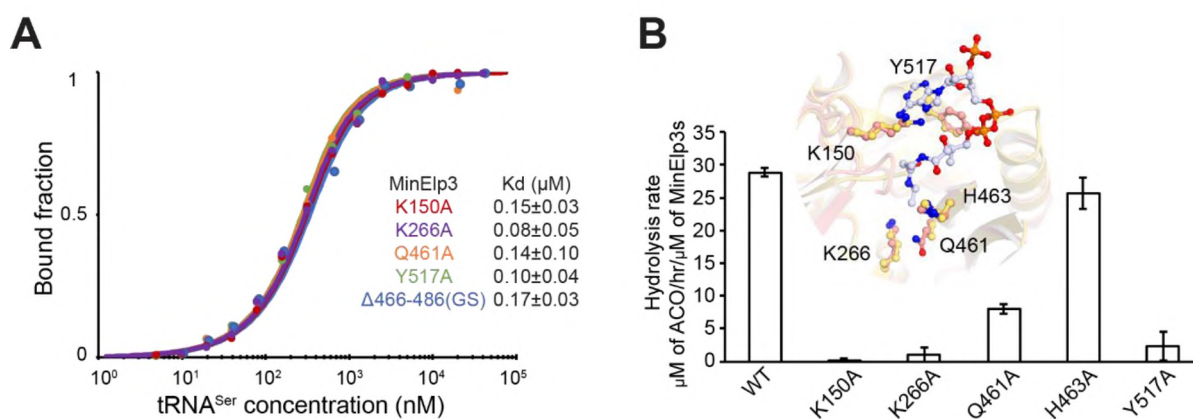

Figure 264. **Role of the ACO active site residues**. A. MST analysis of *Min*Elp3 proteins, including WT, four acetyl-CoA active site point mutation and ACO loop deletion. B. Positions of the active site residues are shown in the inset and ACO hydrolysis rate of these residues in the presence of tRNA (T.-Y. Lin et al., 2019, modified).

To understand whether these mutants lose their ACO binding ability, we performed isothermal titration calorimetry (ITC) measurements (Figure 25). This label-free method measures the heat release upon the binding of two molecules. In a similar principle with the other binding measurements, the sample contains constant concentration of ACO which then is mixed with an increasing amount of protein to obtain the curve that allows the calculation of a K_D value. The K_D of *Min*Elp3 wild-type toward ACO is K_D (135.4±55.3 µM) µM. Among the tested mutants, *Min*Elp3$_{K150A}$ retains wild-type ACO binding affinity (K_D 151.5±50.3 µM) and *Min*Elp3$_{K266A}$ shows weaker affinity to ACO (K_D >250 µM). However, *Min*Elp3$_{Q461A}$, and

*Min*Elp3Y517A lose binding towards ACO. Altogether, the results link the structural information with biochemical characterizations to reveal how ACO is captured by Elp3.
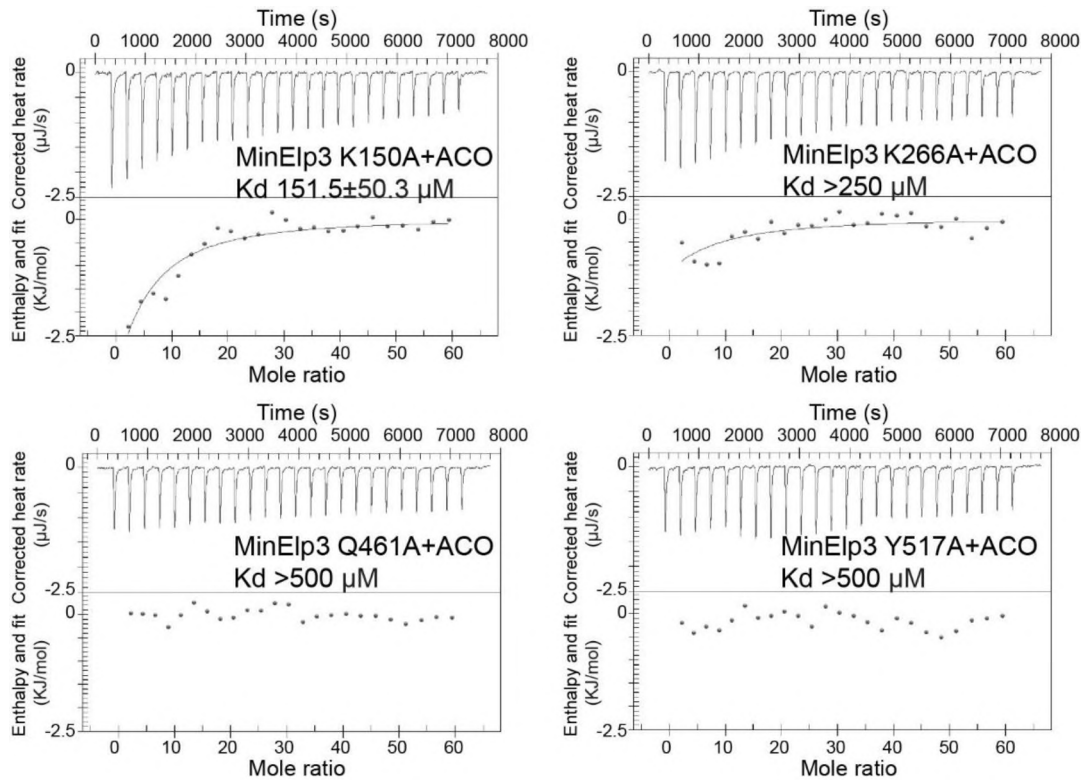

Figure 25. **ITC measurements of *Min*Elp3 mutants and ACO**. ITC experiments performed with *Min*Elp3 with point mutations K150A, K266A, Q461A and Y517A, measuring their affinity to acetyl-CoA (Lin et al., 2019, modified).

While bacteria, archaeal and eukaryotic Elp3s are the main interest of my investigation, viral Elp3s have been neglected. There are over 60 predicted sequences in various unrelated viruses, and most are found in the group of nucleocytoplasmic large DNA viruses (NCLDV). This raises the question whether viruses also require Elp3-mediated modification on U34 and whether the modified tRNA provides a benefit for its virus generation and its life cycle. For instance, *A. anophagefferens* has a double stranded DNA genome of 370 kb and possesses 377 potential coding sequences, and the viral genome is AT rich while its host has a GC rich genome. It is possible that the virus requires Elp3-mediated tRNA modification to generate tRNAs that can produce its proteins while infecting the host cells (Moniruzzaman et al., 2014). *C. roenbergensis* virus has the largest genome of any described virus (730 kb of double

stranded DNA), which also encodes 22 tRNA sequences (Fischer et al., 2010). Whether these tRNAs are relevant and can be modified by Elp3 is not clear.
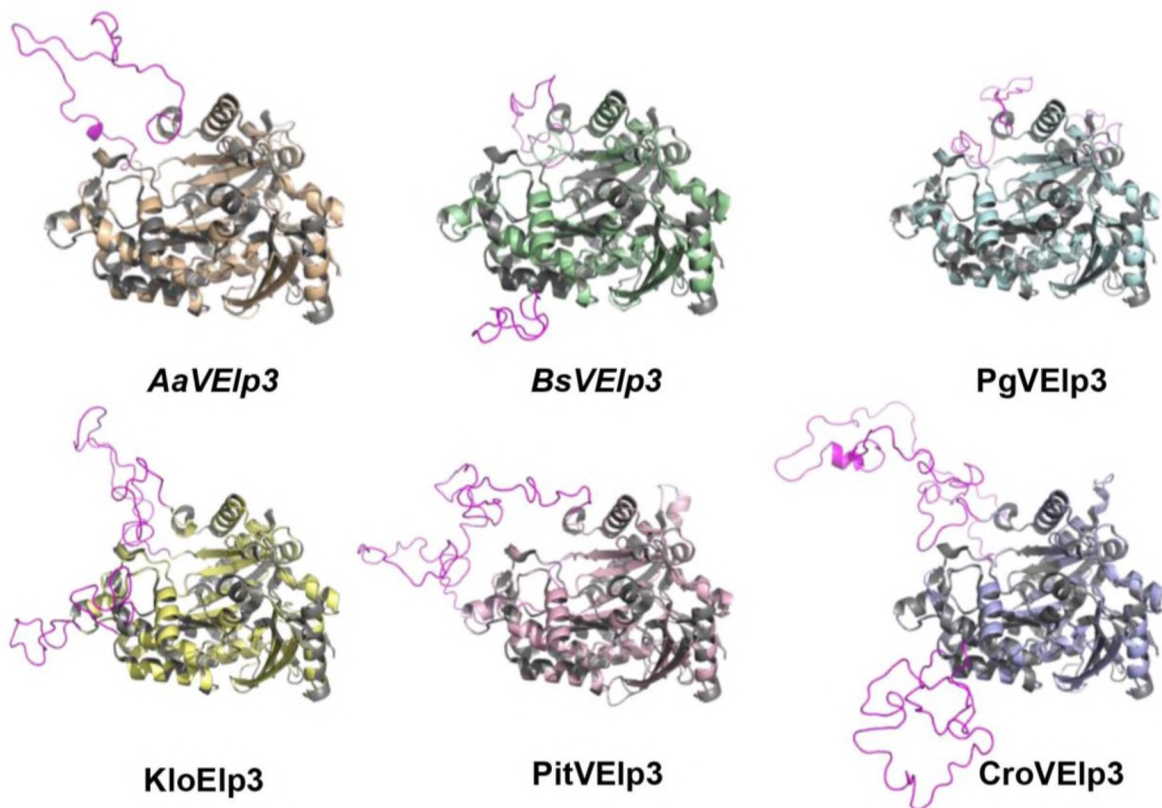

Figure 276. Viral Elp3 model predictions. Comparison of predicted structures *Aurococcus anophagefferens* virus (beige), *Bodo santran* virus (green), *Phaeocytus globosa* virus (lightblue), *Klosneuvirus* (yellow), *Pithovirus* (lightpink) and *Cafeteria roenbergis* virus (purple) supperposed with *Min*Elp3 structure (6ia6, grey). The regions from viral Elp3s that were not overlapping with *Min*Elp3 are colored in magenta.

Although obtaining crystals of viral Elp3s was not feasible due to difficulty in obtaining soluble proteins from bacteria expression system, I then used Phyre2 (Kelley et al., 2015) and Swiss model (Waterhouse et al., 2018) for predicting structural models of viral Elp3s based on the *Min*Elp3 structure (Figure 26). The predicted topologies of viral Elp3s, including specific functional motifs, are similar to *Min*Elp3. For example, rSAM and KAT domains form a cleft (Figure 26). Interestingly, numerous large insertions (unstructured regions) in these viral Elp3s are located near the iron-sulphur cluster binding motif. According to sequence alignment, they indeed contain the conserved iron-sulphur cluster coordination sequence (CXXXCXXC). Whether they could harbor iron-sulphur or can be stabilized by the presence of iron-sulphur or other components, like proteins or tRNAs, remains elusive.

In summary, my work characterized many features of Elp3, including i) details of DCA binding in the ACO pocket; ii) biochemical evidence on how Elp3 selects its substrate tRNAs instead of previously suggested proteins/peptides; iii) the conserved tRNA binding mechanism of Elp3 via its N-terminus.
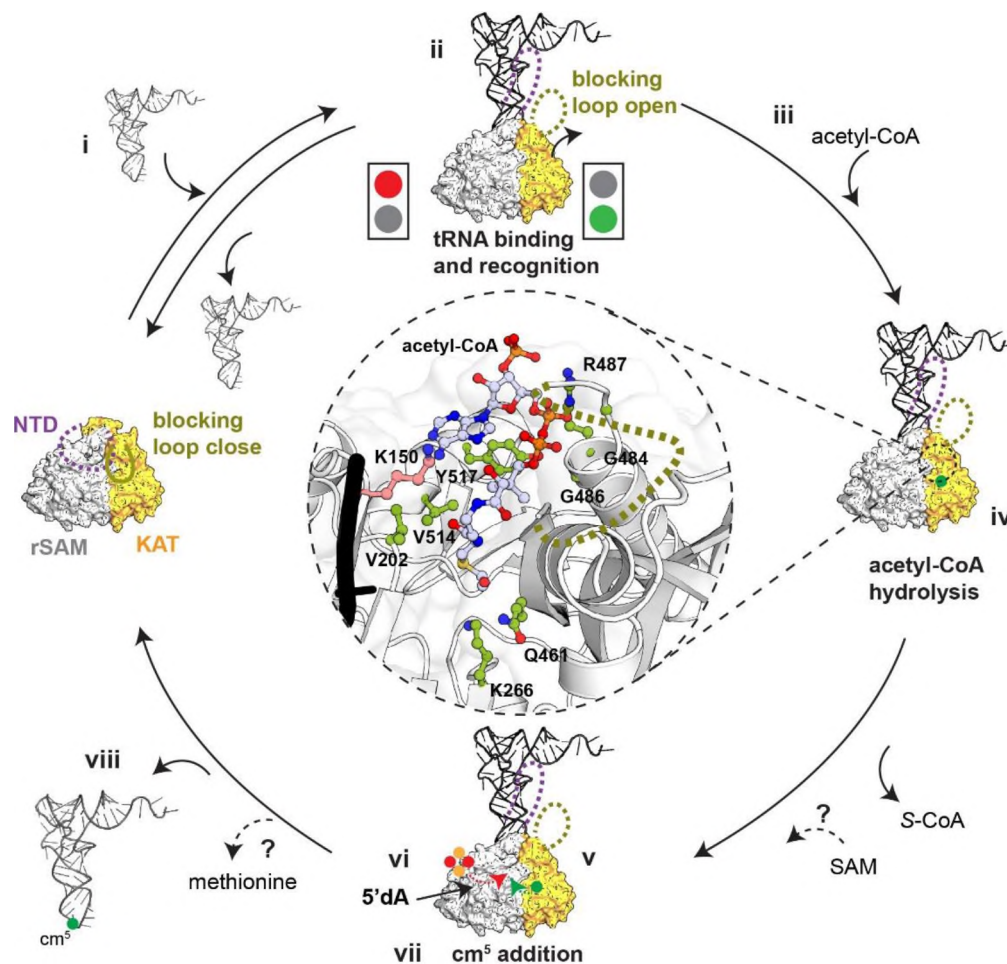

Figure 287. **Proposed diagram of the steps involved in the Elp3-mediated tRNA modification process.** The N-terminus may move when bound to tRNA, which controls the position of an acetyl-CoA blocking loop. Residues responsible for hydrolyzing acetyl-CoA (shown in pink) and binding it (shown in green) are highlighted in the figure's insert. SAM is necessary for catalysis, but when it is recruited and how methionine byproducts are released remain unknown (indicated by question marks) (Lin et al., 2019, modified).

Overall, my work provides an overview of the Elp3-mediated substrate recognition mechanism and its substrate specificity. In detail, Elp3 employs its N-terminus as well as its active site for tRNA binding, which may facilitate to accommodate only certain tRNA species (excluding other RNAs and proteins). Given that all tested tRNAs, carrying diverse sequences, can bind to Elp3, it can be assumed that Elp3 selects the substrate by recognizing the tRNA shape instead of sequence motifs. In addition, not all bound tRNAs can trigger ACO hydrolysis of Elp3. In the case of tRNA$^{Cys}_{GCA}$, it does not contain U_{34} which might be the main determinant for triggering Elp3 activity (Lin et al., 2019). One could also consider that other modifications

residing in the ASL (e.g., methylation at C_{32} or pseudouridine at U_{39}) might be required for the modification of certain tRNAs.

The proposed mechanism is presented in Figure 27: (i) tRNA binds to Elp3; (ii) the tRNA binding is regulated by the core and the N-terminus, which results in opening the ACO loop; (iii) ACO binds to the pocket with the support of the ACO loop; (iv) ACO hydrolysis takes place; (v) the hydrolyzed acetyl group is transferred across domains; (vi) while cleavage of SAM generates the radical 5'-dA to produce the radical acetyl group; (vii) the radical acetyl group is attached to U_{34} to form cm^5U_{34}; (viii) release of the modified tRNA.

Part II - Eukaryotic Elongator complex

In this section, I aim to characterize Elongator complex from higher eukaryotes and understand its biochemical, biophysical, and structural properties.

Most of the yeast Elongator subunit, including Elp1, Elp2, Elp456, can be produced using a bacterial expression system. Me and colleagues made extensive efforts to produce Elp3 in different expression systems. However, we still failed to obtain enough purified eukaryotic Elp3 for any downstream *in vitro* analyses. Nonetheless, purification of the assembled yeast Elp123 subcomplex (containing Elp3) has been possible using a yeast expression system - although the yield was still below the desired levels. I sought to express mouse and human Elp123 subcomplexes using an insect cell expression system, as this method is known for producing challenging proteins or complexes.

Elongator complex construct and purification

In order to express ELP123 or ELP456 in insect cells, the "BigBac" system was used, where the plasmid containing *HsELP1*, *HsELP2* and *HsELP3* were generated using the Gibson assembly protocol (Lampert et al., 2016). In detail, the open reading frames of *ELP1*, *ELP2* and *ELP3* were amplified with specific gating primers, designed to facilitate fragment assembly
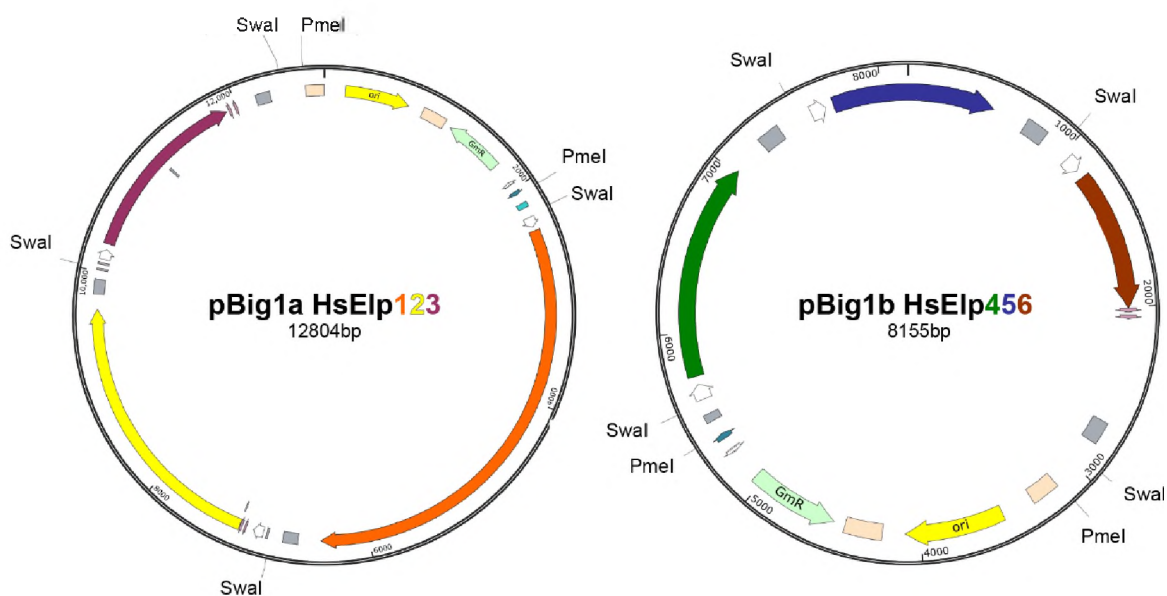

Figure 28. Plasmid maps of *HsELP123* and *HsELP456*. Construct of *HsELP123* with *ELP1* in orange, *ELP2* in yellow and *ELP3* in purple. Between the cassettes are the SwaI digestion sites and the release of all three cassettes can be done from the PmeI sites near *ELP1* and *ELP3*. On the right, construct of *HsELP456* with *ELP4* in green, *ELP5* in blue and *ELP6* in brown.

via complementary sequences. The region amplified for each gene of interest (GOI), called

cassette, contained a polyhedrin promoter, the GOI and an SV40 terminator. After amplification, the cassettes were assembled within the vector backbone in all possible combinations. The order and length of the cassettes proved to be important for the assembly and the order is as follows 5′-*ELP1-ELP2-ELP3*-3′. I also supervised my student while he prepared the plasmid for *HsELP456* using the same cloning and assembly pipeline. In connection to the assembly of all Elongator subunits in the same mega plasmid, I included *HsELP123* in the pBig1a plasmid and *HsELP456* in the pBig1b, so that they could be properly intricated in the pBig2 plasmid in the future (Figure 28).
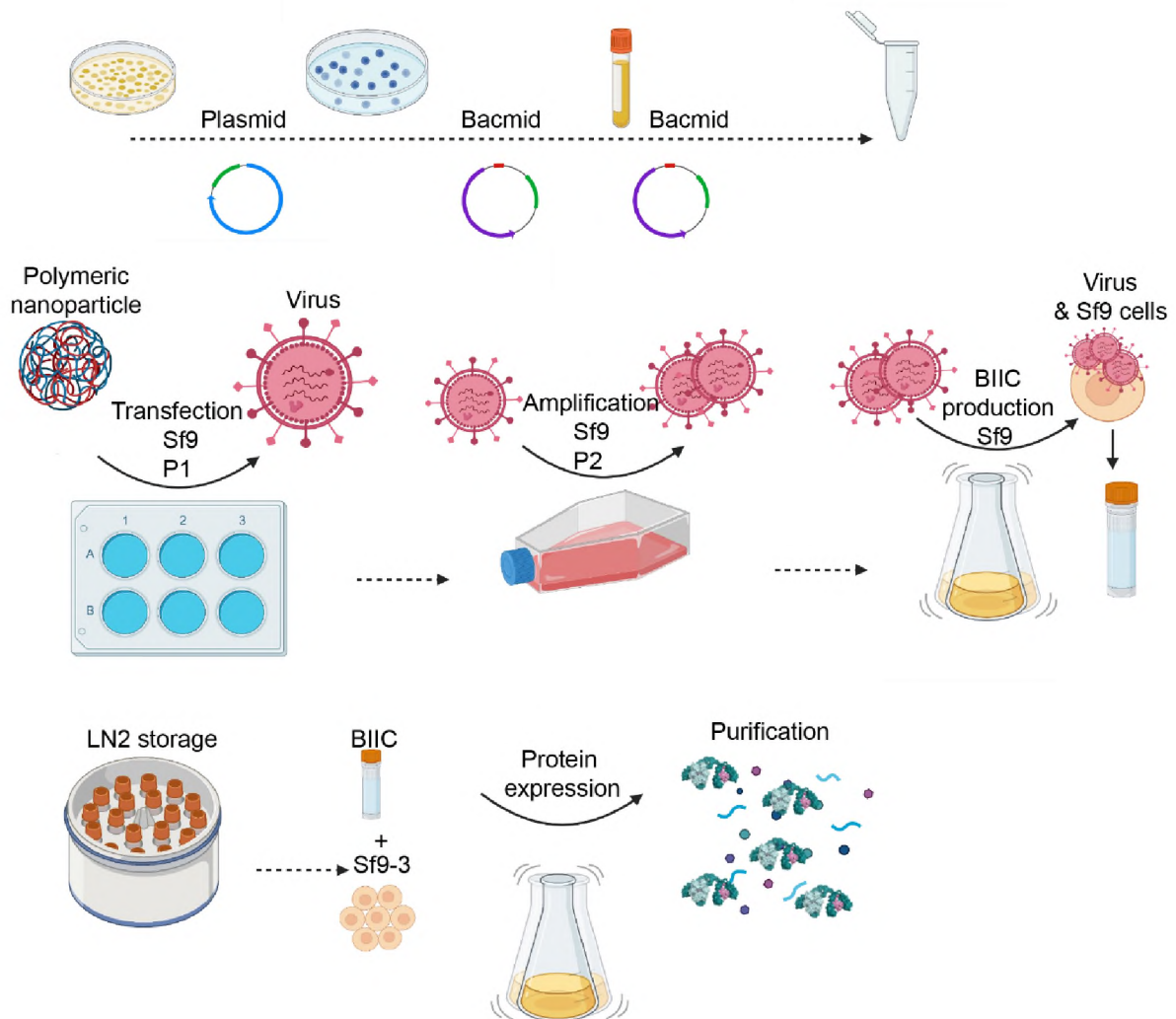

Figure 319. **Schematic representation of insect cell expression**. Plasmid as well as the bacmid are prepared DH10 cells. During Bacmid selection, a color selection system is used that white colonies indicate successfully transposed bacmids and blue colonies are negative. The bacmids are transfected in adherent insect cells (Sf9) using FuGENE® polymer and expresses viruses that are amplified and used to infect the protein expressing cells (Sf9-3). The cell pellets are then collected for purification. (Figure created with Biorender.com)

The recombinant *Hs*ELP1 seems to be expressed in excess compared to *Hs*ELP2 and *Hs*ELP3. To ensure the purified protein complex is obtained with the correct subunit stoichiometry, a Twin-strep Tag (TST) was introduced to ELP3 in the construct. The tag was placed at the C-terminus because it is the least likely place to disrupt the interaction between the subunits. Several clones were obtained, the correct plasmid sequences were confirmed, and all were shown to be able to produce the proteins of interest. The expression system uses a multitude of techniques and steps - starting from the transposition of the cassettes from the pBig plasmid to a bacmid containing the baculovirus genome that is transfected into adherent insect cells (Figure 29). One of the advantages of expressing proteins in insect cell systems is that it provides the opportunity for protein to have post-translational modifications that might be of importance for protein stability, complex assembly, and enzymatic activity.

I tested different insect cell strains, including Hi5, Sf9-2 and Sf9-3, and Sf9-3 cells to optimize the expression levels and to obtain higher yields. Small-scale purifications indeed confirmed that the stoichiometry of each subunit is approximately 1:1:1, indicating a stable and well-defined ELP123 assembly. For the big-scale culture, I have performed extensive trials and optimization to set up the pipeline for complex production. The final yield was about 300 μg per liter of culture, which was a more efficient production than that for *Sc*Elp123 using a yeast overexpression system (60 μg from 12 L culture). More importantly, the purified ELP123 complex contained all three subunits at a 1:1:1 stoichiometry. Of note, a higher mass protein is co-purified along with ELP123, which was analyzed by mass spectrometry and identified to be ACC1 (acetyl-coenzyme A carboxylase 1). It was at first a concern that ACC1 would interfere with our ACO hydrolysis assay readings, but the use of catalytic inactive Elp3 controls for hydrolysis showed no additional background activity.

With the constructs in hand, I created mutated variants, including catalytic and pathogenic mutations. As Gibson assembly method is time- and effort-consuming, I employed a site-directed mutagenesis method to create the plasmids. Despite the challenge of priming such big templates, the usage of high fidelity of Phusion polymerase solved certain technical issues. The obtained plasmids were checked by sequencing to avoid unwanted mutations in the genes of interests.

Characterizations of Elp123 subcomplex

To characterize the *Hs*ELP123 subcomplex regarding the biochemical and biophysical properties, I aimed to investigate its basic features, including tRNA binding and tRNA-induced ACO hydrolysis activity (Figure 30).
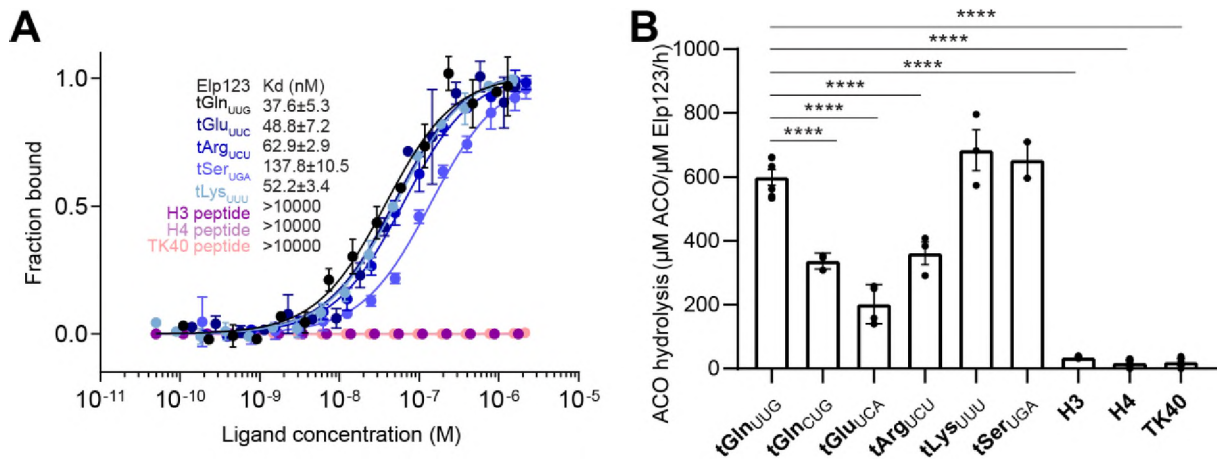

Figure 30. **Characterizations of *Hs*ELP123**. A. MST analyses of *Hs*ELP123 with tRNA^{Gln}, tRNA^{Glu}, tRNA^{Arg}, tRNA^{Ser}, tRNA^{Lys}, and histone peptides H3 and H4 and tubulin peptide containing a lysine. B. ACO hydrolysis rates of *Hs*ELP123 in the presence of tRNAs or peptides. N=3 Statistical analysis: one-way ANOVA. Statistically significant differences are indicated (**$p \leq 0.05$). Data represent mean ± SEM.

First, several human tRNAs harboring a U_{34} were selected for the interaction assays. These tRNAs were internally fluorescently labelled and subjected to MST measurements to determine the K_Ds of binding to wild-type *Hs*ELP123. tRNA^{Gln} has the highest affinity (K_D 37.6±5.7 nM) among all the tested tRNA. Thereby it was used as a control for all the following assays. While most tRNAs affinities were in the range between 40-60 nM, tRNA^{Ser} shows two-times weaker binding affinity, which could be due to the large variable loop of tRNA^{Ser}. Of note, tRNA^{Ser} is modified to ncm^{5}U$_{34}$ and is not clear whether this is caused by the lower affinity to *Hs*ELP123. Furthermore, I investigated whether *Hs*ELP123 has exclusive substrate specificity for tRNAs or whether it can also recognize peptides using MST analyses. The results show that *Hs*ELP123 does not interact with any tested lysine-containing peptide, namely H3, H4 and TK40. This confirms our earlier observation in *Min*Elp3 showing that the KAT domain does not act in a conventional fashion as a protein acetyltransferase and does not interact with protein substrates.

Induced ACO hydrolysis upon tRNA binding is a characteristic of *Min*Elp3 and I observed the same trend of tRNA triggering ACO hydrolysis for *Hs*ELP123. Although all tRNAs trigger ACO hydrolysis at different levels, it is not correlated to the corresponding tRNA binding affinities for *Hs*ELP123. Furthermore, ACO hydrolysis is not triggered at all by the peptide fragments that are derived from histone or tubulin. In summary, these results

provide strong experimental evidence that *Hs*ELP123 has a substrate specificity toward tRNAs and does not modify proteins.

Case study of the ELP1$_{K815T}$23 mutant detected in patients with neurodegenerative disease.

A clinical team treated siblings with severe neuro-developmental delay and identified a single point mutation in the *ELP1* gene, which results in a lysine to threonine missense mutation of residue 815 in ELP1. They contacted us to perform an in-depth biochemical characterizations of the mutant complex (N.-E.-H. Abbassi et al., 2023).
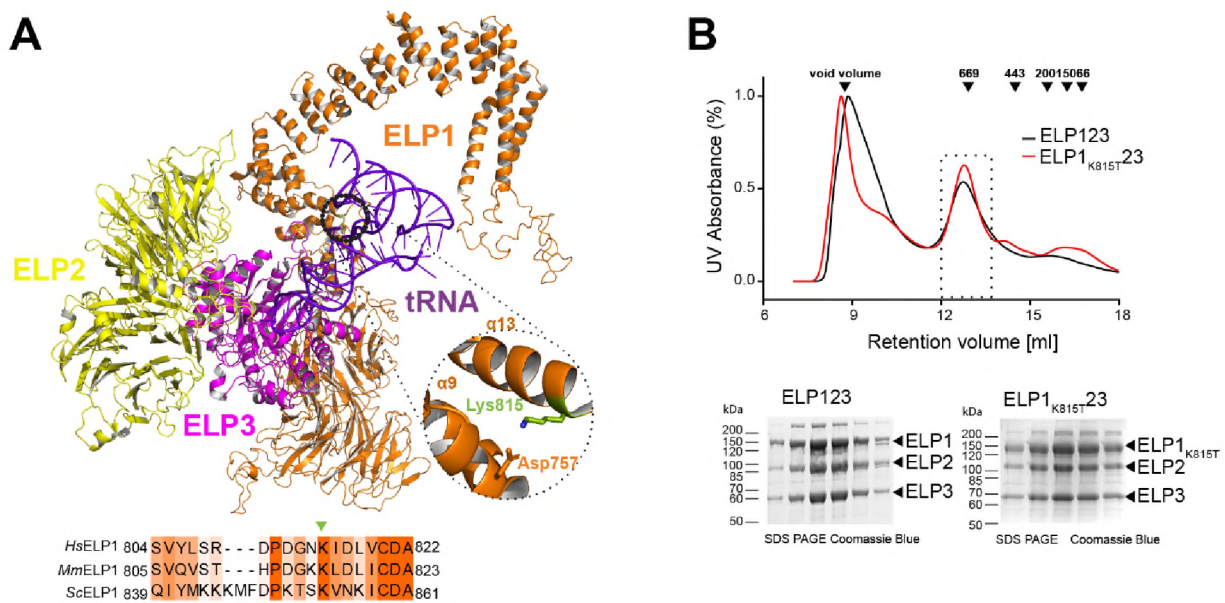
Figure 31. Characterizations of *Hs*ELP1$_{K815T}$23 *in vitro*. A. A cartoon representative of human ELP123 complex harboring the patient-derives Elp1$_{K815T}$23 residue (the predicted human ELP123 model is obtained from AlphaFold2; ELP1: AF-O95163_F1, Elp2: AF_Q61A86, and Elp3:AF_Q9H9T3_F1 while tRNA structure is from PDB 1EHZ). B. (top) Gel filtration profiles of wild-type and mutant. (bottom) The purified proteins were resolved in 12% SDS-PAGE gels and visualized by Coomassie staining (N.-E.-H. Abbassi et al., 2023).

First, I performed the sequence alignment using MUSCLE and found that lysine 815 is highly conserved (Figure 31A). I then mapped the location of Lys815 in the known human ELP1 crystal structure. It resides in a helix of the C-terminal TPR region. To understand if this position may contact other subunits or tRNA, I created a structural model of human ELP123 based on the known cryo-EM map of the yeast complex. The models of the subunits were obtained from AlphaFold2 (AF-O95163_F1 (ELP1), AF_Q61A86 (ELP2) and AF_Q9H9T3_F1 (ELP3) (Jumper et al., 2021; Varadi et al., 2022)) and fitted into the map. Next, I confirmed the model using our previous *Sc*Elp123 structure (PDB: 6QK7) obtained by cryo-EM and the crystal structure of the homodimeric C-terminal domain of *Hs*ELP1 (PDB: 5CQR). Using the high-confidence model, we again located the mutated residue, which is in the base of the tetratricopeptide repeat (TPR) domain. The position of Lys815 is not in the

proximity of any structural motif, involved in the catalytic activity of the complex. Based on the previously resolved *Hs*ELP1 crystal structure, we further analyzed the available density of the structure and observed that the side chain of Lys815 forms a direct contact with Asp757, spanning from helix 9 to helix 13 in the predicted human model (corresponding to helices 4 and 7 in the previously obtained structure of yeast Elongator). This indicates that the residue Lys815 is likely involved in maintaining the tertiary structure of ELP1 and any perturbation in this region could affect the local stability and general flexibility of the Elp1 arm. To address whether the mutation affects complex formation, both ELP123 and ELP1$_{K815T}$23 were produced, analyzed, and compared. Both purified complexes display the expected stoichiometric ratios, show no signs of proteolytic degradation and result in similar yields (Figure 31B). Therefore, the mutation in ELP1 neither affects dimerization of ELP123, nor does it lead to a dramatic destabilization of the sub-complex during the purification. Furthermore, I performed a series of complementary pull-down experiments using affinity tags in either of the sub-complexes. The results clearly show that the K815T mutation did not influence the formation of the fully assembled Elongator complex (Figure 32A). In summary, my analyses show that the presence of K815T in ELP123 does not negatively influence the formation and integrity of the bi-lobed Elongator complex *in vitro*. I then used MST to test the affinity of ELP123 and ELP1$_{K815T}$23 towards human tRNA$^{Gln}_{UUG}$. The ELP123 complex shows a K_D of approximately 50 nM, whilst ELP1$_{K815T}$23 has a 3-time reduced affinity (approximate K_D of 150 nM; Figure 32B). The weaker binding suggests a restricted access of the tRNA to the binding pocket of ELP3, caused by a collapse in the ELP1 arm due to the loss of the interaction between Lys815 and Asp757 that influences the integrity of the ELP1 CTD. It is worth noting that the binding curve for ELP1$_{K815T}$23 did not reach the plateau, which usually happens if the equilibrium of bound and unbound states has not been accomplished. As I was not able to use higher concentrations of the mutated sub-complex, it is most likely that I

overestimated the K_D for the ELP1$_{K815T}$23 mutant and that the actual affinity is even lower than the calculated value after curve fitting.

Furthermore, I set out to explore whether the K815T mutation affected the tRNA-induced acetyl-CoA activity of the catalytic ELP3 subunit in the context of the ELP123
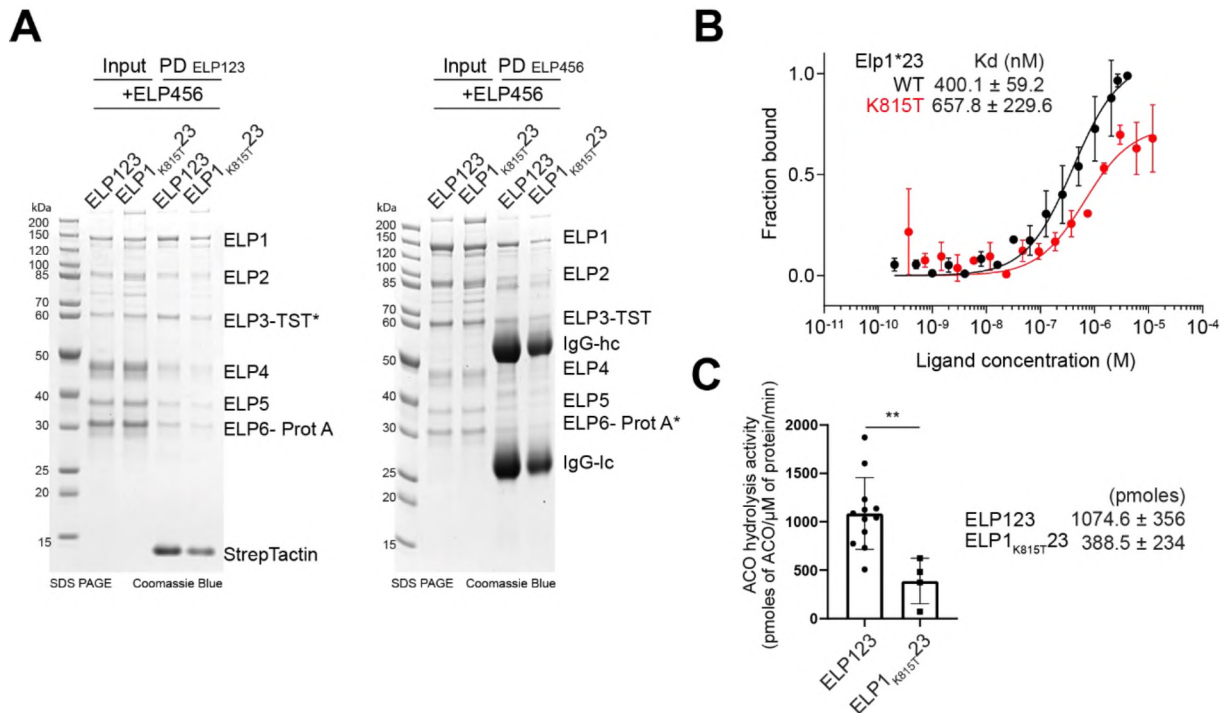

Figure 322. **Biochemical characterizations of Elp1$_{K815T}$23**. A. Protein interaction assay performed between the core elongator ELP123 and the ELP456 subunit for both WT and mutant First the protein were pulled from the TST tag on Elp3 and in the second gel they were pulled from the ELP6 Tag protein. B. tRNA affinity measured using MST assay, ELP123WT is shown in black and the mutant in red. The K_{DS} are shown in inset. C. ACO hydrolysis assay of purified ELP123 in the presence of tRNA$^{Gln}_{UUG}$. n>3 Statistical analysis: t test. Statistically significant differences are indicated (**$p \leq 0.05$). Data represent mean ± SEM. (N.-E.-H. Abbassi et al., 2023).

subcomplex. The results of the analyses revealed a significantly lower hydrolysis rate in ELP1$_{K815T}$23 than in the wild-type subcomplex (Figure 32C). Of note, the assays were performed at high concentration of tRNA (2 μM) to compensate for the lower binding constant in the mutant. Therefore, we concluded that the mutation in ELP1 reduces substrate binding and consequently it renders the initial step of ACO hydrolysis. In summary, our results show that the identified single amino acid substitution in ELP1 leaves the complex intact, but specifically affects the tRNA binding and modification activity of the Elongator.

Structural characterization of core Elongator.

Since the early work on *Dmc*Elp3, the goal was to obtain the structure of Elongator's active site together with its ligands (e.g., tRNA, ACO and SAM) to understand the mechanistic details of its modification reaction. As mentioned earlier, ELP123 can interact with all tested tRNAs with similar affinities in the low nanomolar range, we selected human tRNA^{Gln} to reconstitute a human ELP123-tRNA complex. To facilitate stable complex formation, I assembled the tRNA-protein complex in the presence of an ACO analogue, namely DCA, which was shown to bind to the ACO binding pocket of *Dmc*Elp3. In addition to DCA, another ACO analogue is available, namely *S*-Ethyl-CoA (ECA). DCA lacks the whole acetyl group while ECA has the thiol being replaced by oxygen. As DCA or ECA could both act as inhibitors, I assumed that they likely stabilize the complex by locking the conformation in a certain reactive intermediate. I first analyzed the binding affinity of tRNA^{Gln} to *Hs*ELP123 in the presence of ACO, DCA, ECA or CoA. The presence of ACO, DCA or ECA leads to a slightly reduced tRNA binding by ELP123, while CoA shows no effect on the affinity of *Hs*ELP123 to tRNA^{Gln} (Figure 33). Given that the MST analyses demonstrated that the tRNA still binds to ELP123 in the presence of ACO or ACO derivatives, I reconstituted the individual complexes using the same incubation setup as in the MST. Apart from the desired tRNA-ELP123-ligand complexes, I also attempted to reconstitute other complexes - including ELP123-tRNA^{Glu} and ELP123456 with tRNA^{Glu} (with and without DCA). Subsequently, I prepared the samples for vitrification on cryo-EM grids and single particle data collection (Figure 34).
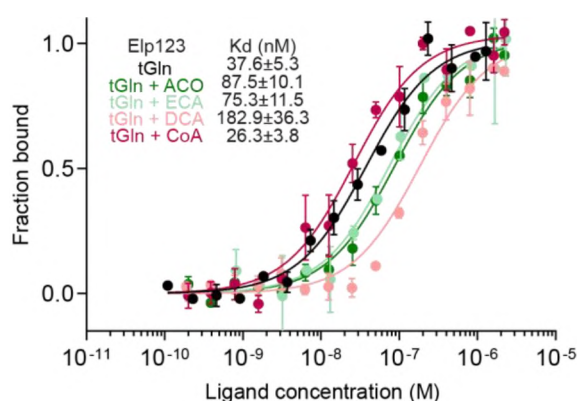

Figure 333. **Influence of ACO on tRNA binding**. MST analyses of tRNA^{Gln} binding to ELP123 in presence of ACO and its analogs. N=3 Data represent mean ± SEM.

*Hs*ELP123 needs to be expressed and purified from insect cells expression, which provides relatively small l yields (50-100 μg per 1L of culture). Hence, crystallization is not a very good option and I mainly used cryo-EM, as it only requires a few micrograms of protein for grid preparation. The sample was prepared following an established protocol (Figure 34).

The prepared cryo grids were screened using a Glacios microscopy prior data collection. These iterative rounds of grid optimization ensured that the samples were in thin ice and distributed evenly in the holes, which is needed to maximize the collected data quality from the Titan Krios microscope. Several preliminary data sets (with 1000-3000 micrograp*hs*) were collected and the data quality was determined by the initial 3D reconstruction. The datasets with high quality 3D reconstructed maps were used to collect additional micrograp*hs* to reach a very large dataset size.
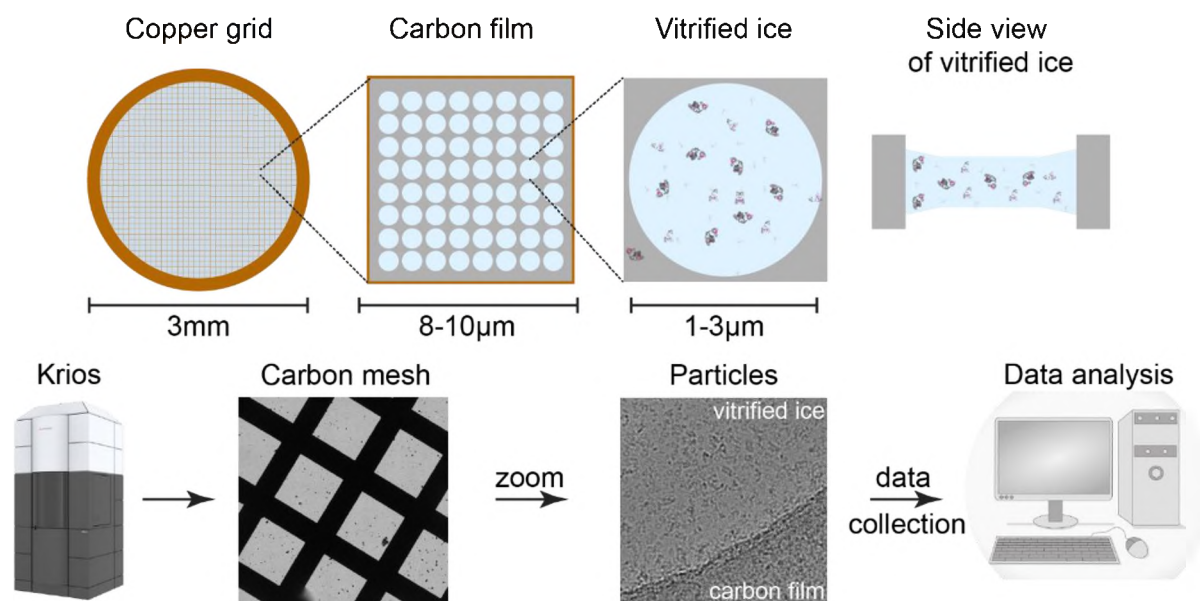
Figure 344. **Cryo-EM sample preparation and data collection/processing pipeline**. Graphic description of protein prepared in copper grid and froze in vitrified thin ice with various orientation, which is then subjected to data collection in microscopy (Krios) and further data processing.

The obtained 20,720 micrograp*hs* from the dataset of ELP123-tRNA-DCA were first processed by motion correction followed by CTF estimation/correction. Picking particles was performed by blob picking (CryoSPARC) and TOPAZ with a large-enough box size. The picked particles were curated using several rounds of 2D and 3D classifications to remove junk particles. The number of particles decreased from initially 1,803,276 to a total of 421,011 so we selected only 23,3% for further structure refinement. For the ELP123-tRNA^{Glu}-ECA dataset from 3192 Micrograp*hs*, we obtained 409,189 particles that dropped to 51,669 after analyses, 12,6% of the original particles were used for analysis (Appendix, Table1).

We successfully obtained the cryo-EM structures of ELP123-tRNA^{Glu}-DCA (Figure 35) and ELP123-tRNA^{Glu}-ECA. As the results between the datasets were similar, I will focus on the results of ELP123-tRNA^{Glu}-DCA. In this dataset, I could observe three types of particles, namely form1 as ELP123 (4.2 Å), form1.2 as ELP123-tRNA-DCA but with one lobe (3.8 Å),

and form2 as ELP123-tRNA-DCA with two lobes (4.3Å) (Figure 35). Form1 represents the apo structure of ELP123, but whether this state represents the conformation before or after tRNA binding cannot be answered conclusively. Given that form1.2 only displays ELP2, ELP3 and a partial structure of ELP1, I checked the protein integrity by SDS-PAGE and confirmed that each subunit remains intact after the incubation and no major degradation is observed for ELP1. Therefore, it is most likely that the C-terminal part of ELP1 is partially flexible in the absence or presence of tRNA. To obtain the structure with two lobes, I performed additional 3D classifications. However, due to the limited numbers of particles available, orientational bias or the high flexibility of the two lobes (in respect to each other), I did not manage to obtain a high-resolution two-lobed map. I focused on the one-lobe maps I obtained (of Form 1, 1p2 and 2) and to obtain the assembled complex models, I employed predicted protein structures from AlphaFold2 and fitted the models to the maps using the molecular dynamic fitting method: Namdinator. Once the models were fitted, the structure refinement was performed in Phenix and the geometry of the side chains were further manually checked and corrected (Jumper et al., 2021; Kidmose et al., 2019; Varadi et al., 2022).
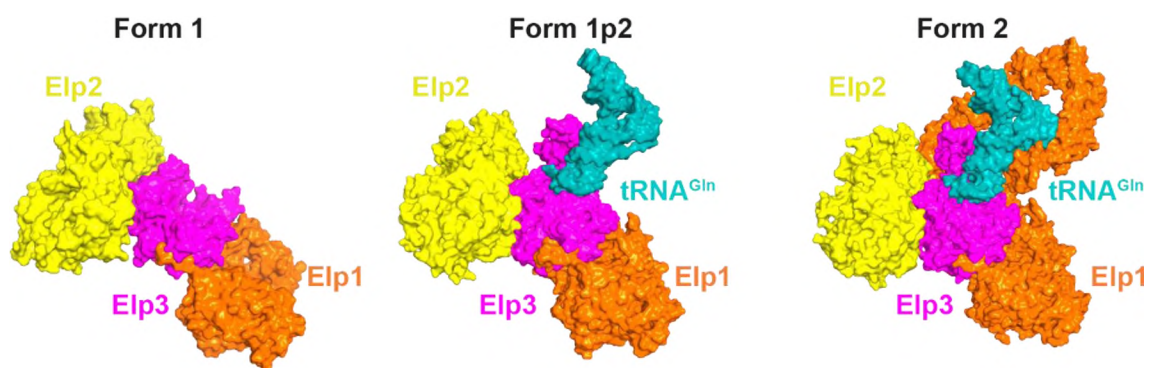

Figure 355. **tRNA-bound *Hs*ELP123 structures**. Cartoon representation of structure of HsELP123. The three forms observed are Form 1 with Elp1 N-terminus, not TPR domain or C-terminal domain, ELP2 and ELP3without N-terminus. Form 2 is the full ELP1, ELP2 and ELP3 with a tRNA bound to ELP3. Form 1.2 is intermediary between the other two with ELP1 N terminus and no C terminus, full ELP2 and ELP3 and a tRNA bound to ELP3. Subunits are colored as ELP1 in orange, ELP2 in yellow, ELP3 in magenta and tRNA in purple density.

Given that form2 displays more detailed structural information than form1 and form1.2, I focused on analyzing structural features in form2. Overall, the *Hs*ELP123-tRNA structure is very similar to its yeast counterpart (Figure 35). In detail, the elbow region of the tRNA is bound via the C-terminus of ELP1, while the catalytic cleft of ELP3 binds the ASL. In addition, several features in ELP3 seem to facilitate tRNA binding apart from the catalytic site (Figure 36). The helices and loops of the central linker (CL) of ELP3 between rSAM domain and KAT domain are well structured and bind to the tRNA. The N-terminus of Elp3 shows three parallel helices arranged in a similar way to AlphaFold2 predicted. This motif clearly becomes stable and interacts with the tRNA at the stem region of the ASL where several basic residues of ELP3, including Lys42, Lys44, Lys48 and Arg56, are positioned near the tRNA backbone. This is in line with the previous biochemical observations in *Dmc*Elp3 (Figure 22) and suggests that the tRNA recognition mechanism might be structure rather than sequence specific.
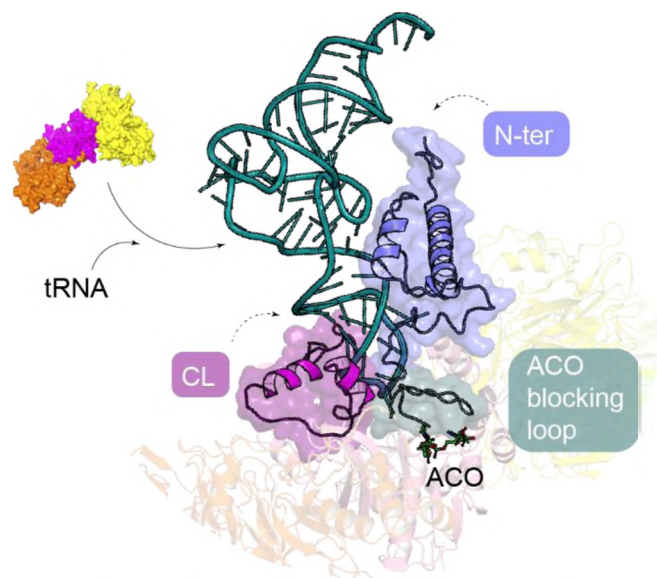

Figure 366. **Close view of the tRNA binding by ELP3**. Cartoon representation of the tRNA binding inducing stabilization of motifs of ELP3. The N-terminus of ELP3 (lavender), CL (purple) and ACO blocking loop (green) of ELP3 are highlighted and the movements are as indicated. The ACO binding in the pocket is also highlighted. An inset is the apo ELP123 with each subunit colored (ELP1 in orange, ELP2 in yellow and ELP3 in magenta).

Even though eukaryotic N-termini display similar ability to recognize and bind tRNA, they share very low sequence similarity (Figure 15). To understand if there is a different motif or structural arrangement among these N-termini when they interact with tRNA, I compared the available structures that have been obtained in presence of tRNA. Although the densities for the N-terminus in the tRNA bound structures are less defined in mouse and in yeast Elp123, it is still feasible to fit the predicted helices into the density and generate accurate models

(Figure 37). Although *Sc*Elp3 harbors a longer N-terminus, it shows no difference in the bound conformation compared to its mouse or human counterpart. In addition, the distances between the tRNA and N-terminal motifs are almost identical in all three structures.
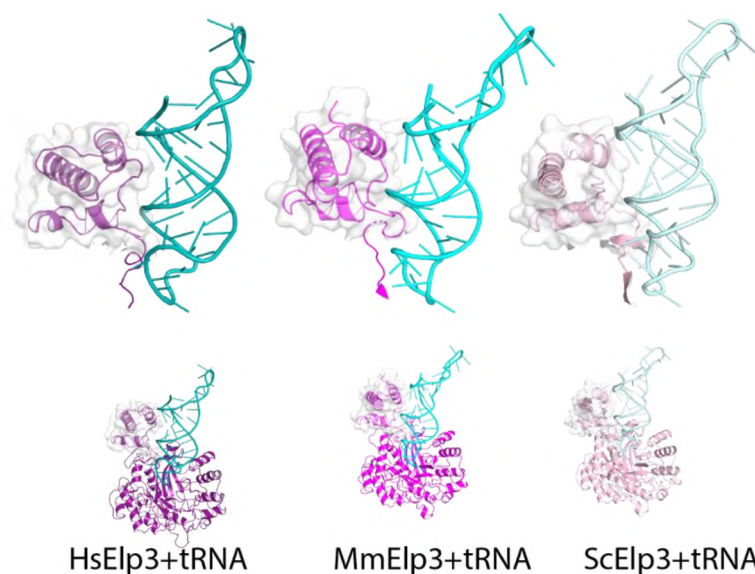

Figure 377. **Structural comparison of *Hs*ELP3, *Mm*Elp3 and *Sc*Elp3.** (top) The cartoon representation of the zoom-in view at the N-termini interacting with the stem region of the ELP3 bound tRNA, (bottom) The cartoon representation of the while ELP3 binds to tRNA. Only partial tRNA structure is shown.

Given the high quality of the tRNA-bound human ELP123 map, the density of the tRNA is very well-defined. In particular, the high resolution of the ASL allows the visualization of all protein-tRNA interactions in greater details (Figure 38A). As mentioned earlier, the ASL of tRNA is buried in the catalytic site of ELP3 (Figure 38B). I identified several basic residues, such as Arg242, Arg361, Arg364 and Arg402, interacting with the ASL of tRNA. The residue Arg364 is positioned most centrally and interacts with the phosphate group between U_{33} and U_{34}.

To investigate if the identified motifs or residues could be involved in tRNA binding and/or downstream activity, I generated several mutants – e.g., ELP123$_{\Delta1-85}$, ELP123$_{R364A}$, and ELP1$_{\Delta1132-1224}$23 (Figure 39). The yields for ELP123$_{\Delta1-85}$ and ELP123$_{R364A}$ are lower than for the wild-type, whereas the complex harboring a loop deletion in ELP1 results in an even lower yield, which was only sufficient for the enzymatic ACO hydrolysis activity assay. In detail, the MST analyses of ELP123$_{\Delta1-85}$ and ELP123$_{R364A}$ show that losing the Arg364 or the N-terminus of ELP3 reduces the tRNA binding affinity by 2-3 times compared to wild-type. Of note, in
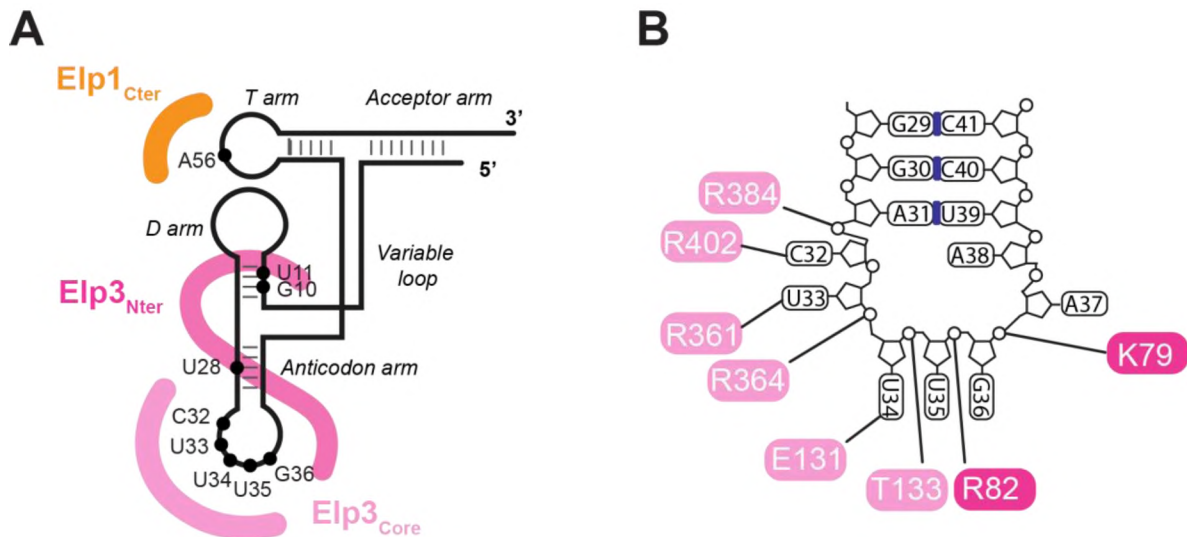
Figure 388. **Elongator residues interacting with tRNA**. A. schematic representation of 2D structure of tRNA interacting with ELP1 C-terminus, ELP3 N-terminus and ELP3 core. B. Structurally identified residues interacting tRNA^{Gln} ASL. Light pink residues lie in the core of ELP3 while magenta residues are from in the N-terminus.

our previous study, a similar ELP1 loop deletion was generated for ELP123 and the tRNA binding affinity was confirmed to be similar to wild-type in EMSA analysis. Next, I performed the ACO hydrolysis assay to monitor the tRNA-triggered hydrolysis activity in these mutants. It is clear that ELP123$_{\Delta1-85}$ and ELP123$_{R364A}$ mutants abolish the activity while ELP1$_{\Delta1132-1224}$23 retains about 50% ACO hydrolysis activity compared to wild-type.
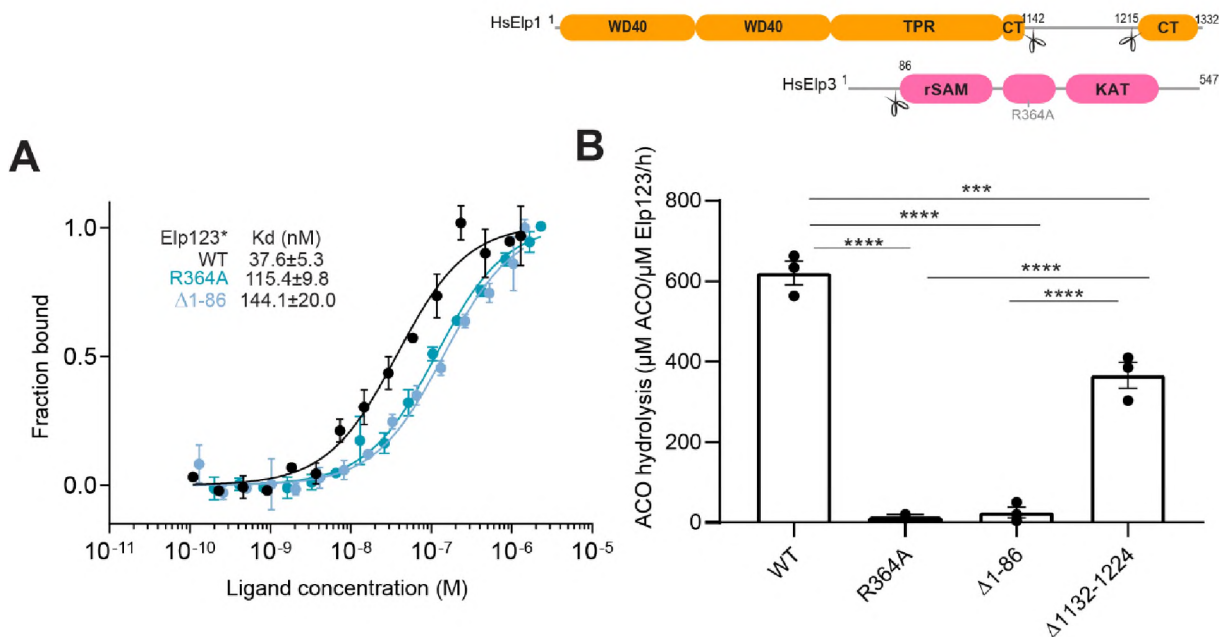

Figure 399. **Biochemical characterizations of tRNA binding residue or motifs of *Hs*ELP123**. A. MST analyses of ELP123WT, ELP3$_{R364A}$ and N-terminus truncation B. (top) Representation of the truncations in ELP1 and ELP3. (bottom) ACO hydrolysis analyses the tRNA binding mutants. N=3 Statistical analysis: One-way ANOVA. Statistically significant differences are indicated (***$p \leq 0.005$; ****$p \leq 0.0005$). Data represent mean ± SEM.

73

Because of the high resolution of the tRNA-bound structure of *Hs*ELP123, the densities for most nucleotides, bases, and phosphates of the tRNA molecule are clearly traceable. In particular, the ASL density allows us to reliably build a full atomic model. The ASL structure is orientated in the same way as in the published yeast tRNA-Elp123 model (Dauden et al., 2019) - the ASL is unwound when bound to *Hs*ELP3 (Figure 40). Moreover, the universally conserved U_{33} points towards the KAT domain while U_{34} faces the iron-sulphur cluster in the rSAM domain.
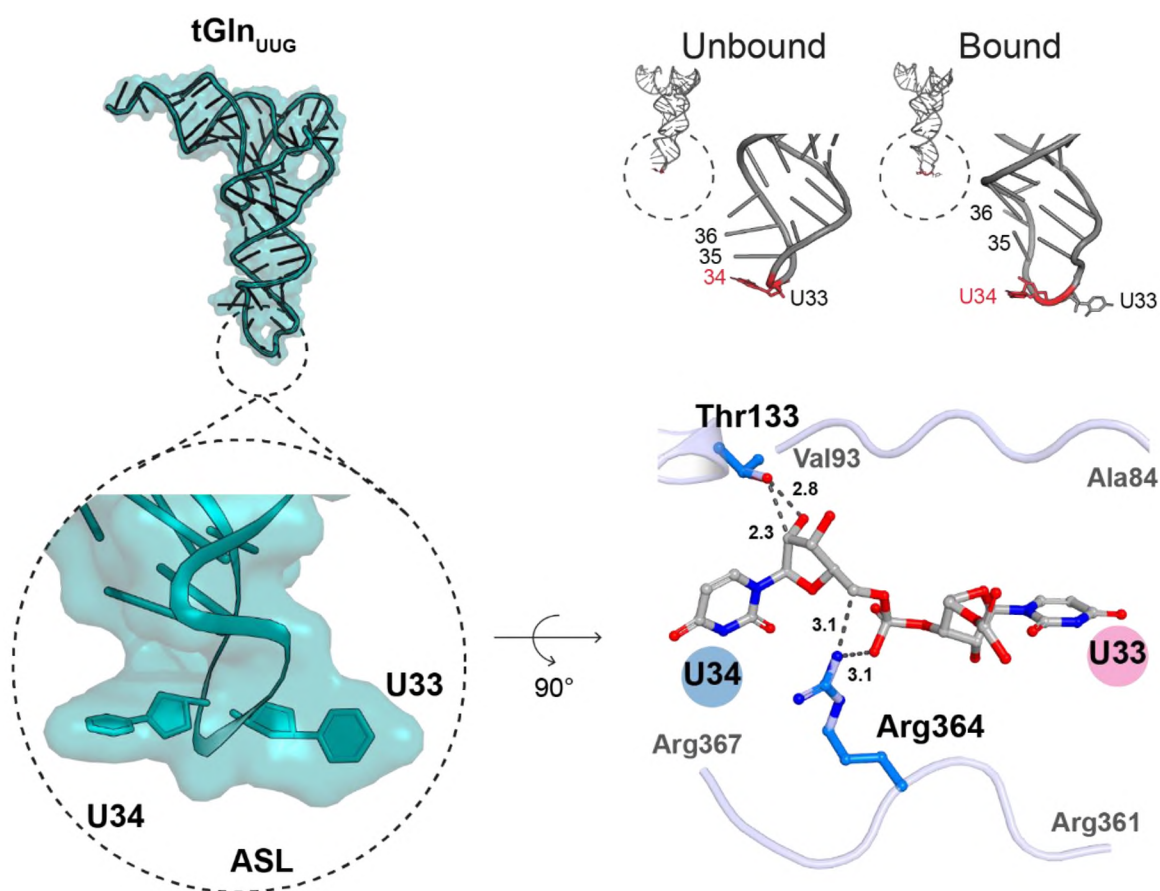

Figure 40. Close-up view of U_{33} facing the KAT domain. Small representation of the bound and unbound shape of the ASL and position of U_{34} and U_{33} in the tRNA binding pocket.

As mentioned in Figure 32, tRNA binds to *Hs*ELP123, resulting in ACO hydrolysis. In the ASL bound structure, U_{34} is not in close proximity to ACO, suggesting that the U_{34} is not the ultimate trigger for this reaction. Since U_{33} is facing ACO, we speculated that U_{33} might be the determinant for triggering ACO hydrolysis. In addition, U_{33} is present in almost all tRNAs (except for initiator-tRNA^{fMet}) and it is never modified in eukaryotes. Several mutated versions of human tRNA$^{Gln}_{UUG}$ carrying nucleotide substitution were produced, including tRNA$^{Gln}_{C33UUG}$, tRNA$^{Gln}_{UC34UG}$, tRNA$^{Gln}_{C33C34UG}$. These tRNA mutants do not affect
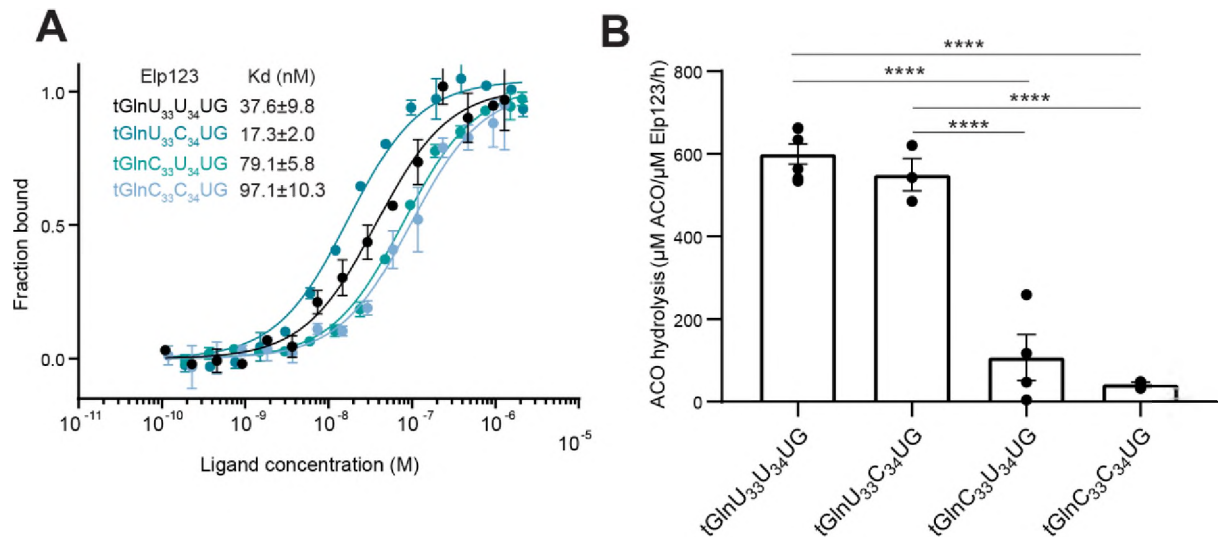
Figure 401. **Biochemical analyses of the tRNAs carrying mutated ASL**. A. MST analyses on ELP123 with various versions of $tRNA^{Gln}$. B. ACO hydrolysis rate of ELP123 triggered by various versions of $tRNA^{Gln}$. N=3 Statistical analysis: One-way ANOVA. Statistically significant differences are indicated (***$p \leq 0.005$; ****$p \leq 0.0005$). Data represent mean ± SEM.

HsELP123 binding dramatically and the U_{34} substitution with a cytosine does not affect tRNA-induced ACO hydrolysis activity, while the U_{33} substitution greatly reduces the activity (Figure 41). Furthermore, the double substitution of $U_{33}U_{34}$ with two cytosines completely abolishes the enzymatic activity. These findings are the first data that implicates U_{33} in the triggering U34 modifications.
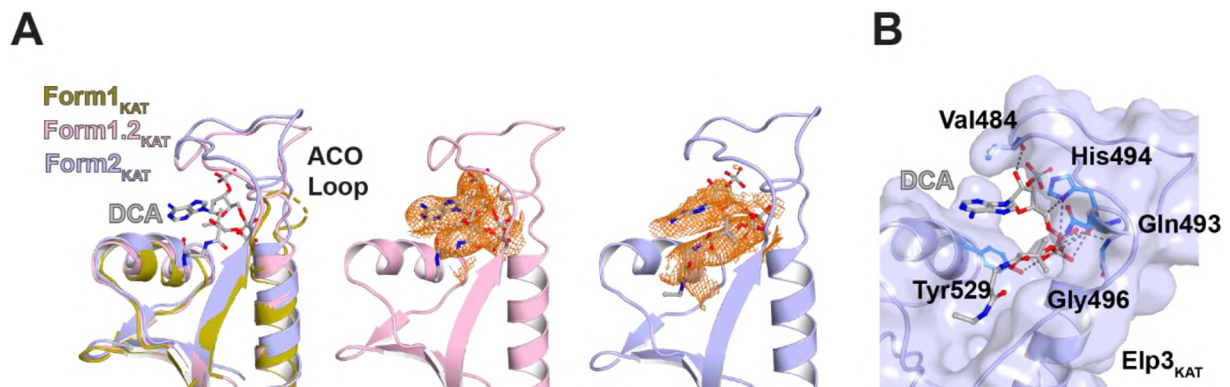

Figure 412. **Structural comparison of ACO loop.** A. Superposition of the ACO loop in HsELP123 structures with color-coded, including form1 (ELP123), form1.2 (tRNA-ELP123-DCA but with flexible TRP of ELP1) and form2 (tRNA-ELP123-DCA). The density of DCA in form1.2 and form2 are highlighted. As form1 does not show DCA density, a modeled DCA is placed. In addition, the ACO loop is not visible in form1, thereby a dash line is placed. B. A close-up view on residues interacting with DCA in form2.

DCA binding to *Dmc*Elp3 has been observed in a crystal structure, visualizing the details of the interacting residues. In addition, the co-crystal structure of *Dmc*Elp3-DCA was only obtained when a specific loop region was deleted - therefore we call this loop ACO "blocking" loop and hypothesized that the binding of DCA should be regulated upon tRNA binding. In the tRNA-ELP123-DCA dataset, I also identified DCA in form1.2 and form2 but not form1. Given that tRNA binding stabilizes the N-terminus as well as the ACO loop, I conclude that the presence of tRNA displaces the loop region. Therefore, similar to the artificial deletion of the loop, tRNA binding manages to "open" the ACO pocket and allows the ligand to enter and bind to ELP3. The bound DCA is coordinated very similar in the cryo-EM structure compared to the same ligand in the DCA-*Dmc*Elp3 crystal structure (Figure 42). In detail, the adenine group of DCA interacts with Tyr530 and the long carbon chain of DCA contacts several conserved amino acids in the ACO binding pocket (residues 478-494).
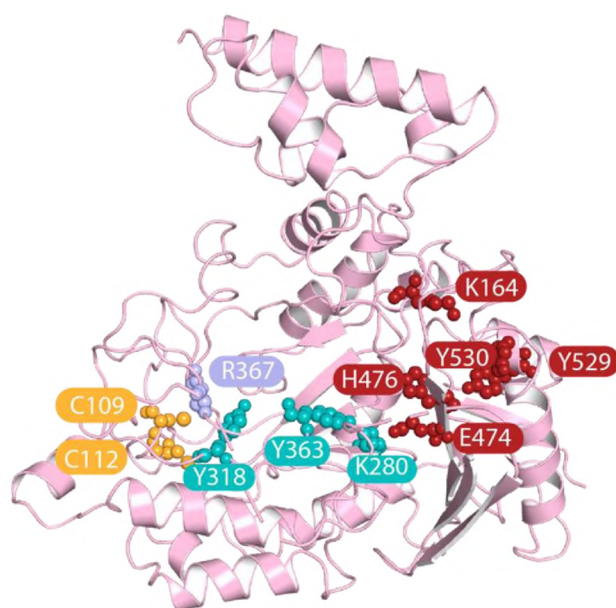

Figure 423. **Map of the investigated conserved catalytic residues in ELP3**. The residues are highlighted and categorized by color code. Red: ACO binding and hydrolysis; cyan: acetyl group transferring; light blue: SAM binding; yellow: iron-sulfur binding.

As the key residues involved in ACO hydrolysis reaction has been characterized for *Min*Elp3 and *Sc*Elp3, I investigated whether these highly conserved residues in *Hs*ELP3, namely, Lys164, Lys280, Glu474, His477, Tyr529 and Tyr530 serve the same purpose (Figure 43). First, I measured the tRNA binding affinity of these mutants (Figure 44). The MST results show that most mutants have slightly increased affinities, whereas the double tyrosine mutant Y529A/Y530A possesses 3 times weaker binding. Next, I performed ACO hydrolysis assays

and found that all mutants significantly reduce their activity. It is worth noting that the protein production yields of Y529A/Y530A was very low, while the other mutants resulted in comparable yields to the wild-type.
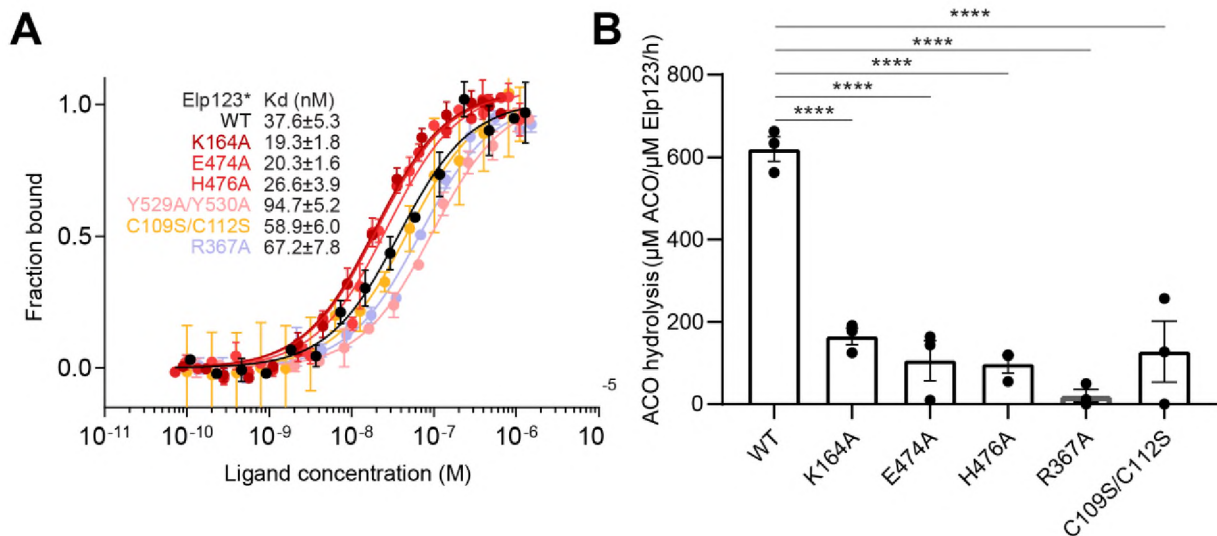

Figure 434. **Biochemical characterizations of the conserved catalytic residues in ELP3**. A. MST analyses of ELP3WT as well as the catalytical mutants of ELP3. The measured K_Ds are in inset. B. ACO hydrolysis rate of these active site residues. N=3 Statistical analysis: One-way ANOVA. Statistically significant differences are indicated (****$p \leq 0.0005$). Data represent mean ± SEM.

I was also wondering whether mutating residues in the rSAM domain would affect the tRNA binding or ACO hydrolysis. As the iron/sulphur is coordinated by Cys109 and Cys112 while SAM is bound by Arg376 (Figure 43), I generated the respective mutants (C109S/C112S and R367A) and investigated their impact on the enzyme activity (Figure 44). Both mutants show 2-times weaker tRNA binding compared to wild-type and surprisingly also lose the ability to hydrolysis ACO. This result suggests a possible cooperative mechanism between both domains in *Hs*ELP3. Of note, the yields for the C109S/C112S mutant are also very low, indicating that the binding of iron-sulphur could contribute to complex stability.

Acetyl transfer residues

My biochemical characterization and structural analyses revealed that U_{33} triggers ACO hydrolysis. Given that the distance between the acetyl group in ACO and the target base (U_{34}) is about 15 Å, it remained a long-standing question how the hydrolyzed acetyl group can get in contact with the radical generated in the rSAM domain and reach the wobble base. It has been proposed that several amino acids might take part in transferring the hydrolyzed acetyl group across the domains. In the tRNA-bound models, we noticed that two lysine residues, namely Lys280 and Lys316, are lined up directly between ACO and U_{34} (Figure 45).
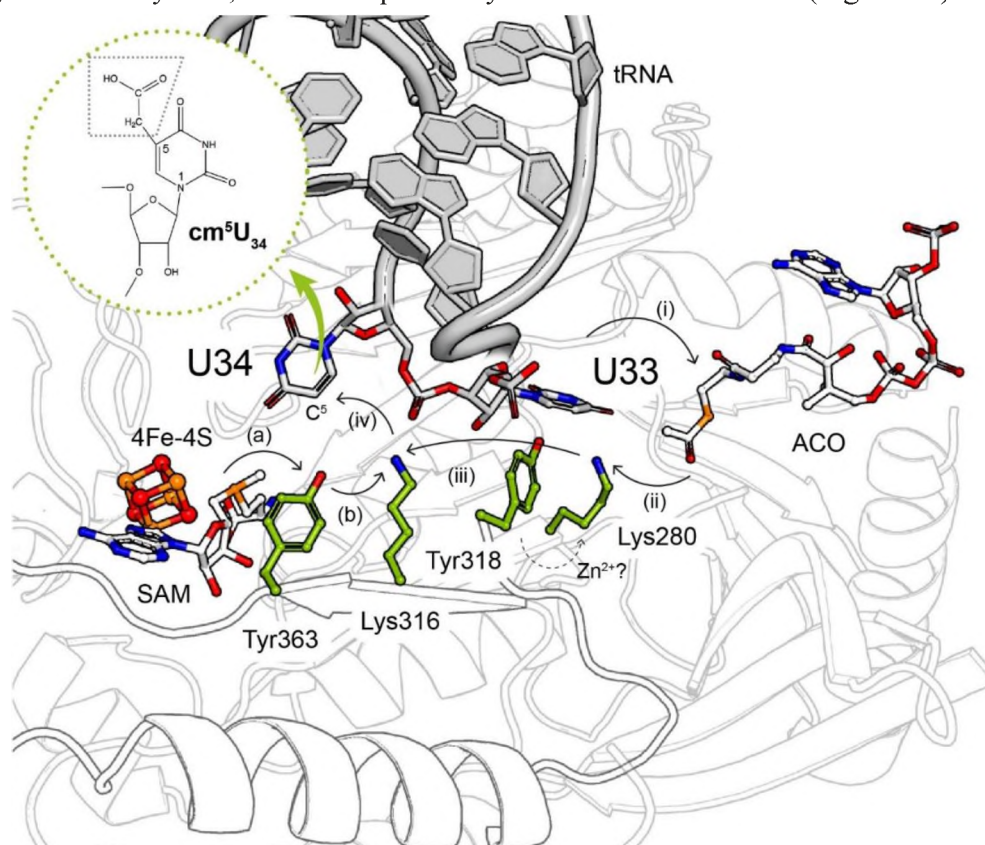

Figure 465. **Proposed acetyl transfer from KAT to SAM domain.** ELP3 cartoon structure is shown in white with outline. ACO, iron-sulfur cluster as well as SAM are colored by the elements. The ASL is in grey with U33 and U34 shown in sticks and colored by elements. The proposed residues are colored in green with oxygen in red and nitrogen in blue. The formed cm^5U chemical structure is shown in the inset where the added moiety is highlighted in a dash box. The proposed mechanisms are indicated by arrows. (i) U33 trigger the hydrolysis of ACO; (ii-iii) the hydrolyzed acetyl group is transferred via Lys280 and Lys316 with the help of Tyr318 and Tyr363. (a-b) the cleavage of SAM produces the 5-dA• radical which could attach to Tyr363 and then attack the acetyl group to form the radical acetyl group. The radical acetyl group then attacks the C5 position of U34 to form the cm^5U (iv).

It is possible that the acetyl group can be transferred via these lysine residues. To facilitate this transfer, an intermediate deacetylation mechanism should be in place as well. Based on the known mechanisms of protein deacetylation by HDACs, we deduced that Elp3 would require tyrosine and histidine residues for maintaining an acetylation-deacetylation

based transfer. Interestingly, we find Tyr318 positioned exactly in between Lys280 and Lys316, while Tyr363 is located between Lys316 and U$_{34}$. To test the hypothesis whether these lysine residues can be acetylated, purified HsELP3 protein was subjected to mass spectrometry (MS), which confirmed that Lys280 and Lys316 are acetylated as AC-K280 and AC-K316 at low abundance (appendix 2). I then treated the HsELP123 complex with tRNA and ACO and subjected the samples to MS analysis again. The abundance of the AC-K280 and AC-K316 still remained relatively low. Furthermore, I generated three mutant variants of ELP3, namely ELP3$_{K280A}$, ELP3$_{Y318A}$ and ELP3$_{Y363A}$, to investigate whether the acetylation of lysine residues is enriched or diminished in these mutants. The detected spectra of AC-K280 or AC-K316 still remained low. Given that the method is not quantitative, the results were not fully conclusive but showed that Lys280 and Lys316 can get acetylated. Of note, the MS identification detected two lysine residues, namely Lys6 and Lys164, that are also acetylated with high detection scores and several detected spectra. Lys6 is in the N-terminus and the functional role of it being acetylated is not clear. Lys164 is known to be involved in ACO binding and how its acetylation affects the interaction is yet to be investigated.
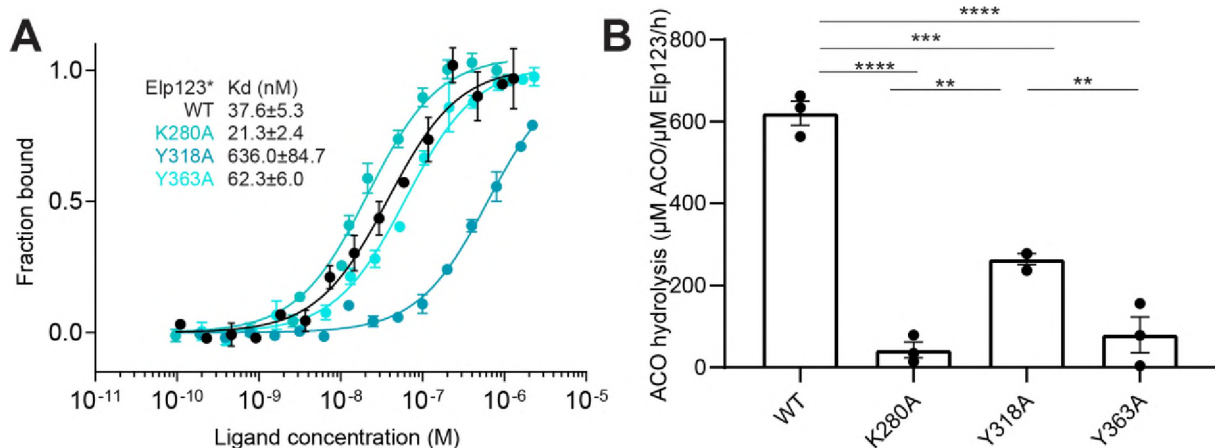

Figure 476. **Biochemical characterizations of residues in ACO hydrolysis and transfer**. A. MST analyses on ELP3 mutants with tRNA^{Gln}. The calculated K$_D$S are listed in inset. B. ACO hydrolysis rate of WT and mutants. N=3 Statistical analysis: One-way ANOVA. Statistically significant differences are indicated (**$p \leq 0.05$; ***$p \leq 0.005$; ****$p \leq 0.0005$). Data represent mean ± SEM.

To investigate the regulatory role of these residues for the activity of Elongator, I performed MST assays and ACO hydrolysis assays on ELP3$_{K280A}$, ELP3$_{Y318A}$ and ELP3$_{Y363A}$. First, the ELP3$_{K280A}$ and ELP3$_{Y363A}$ retain similar tRNA binding affinities as wild-type, whereas ELP3$_{Y318A}$ shows a 10-fold weaker binding rate (Figure 46). Second, I observed a drastic reduction of ACO hydrolysis rate for ELP3$_{K280A}$ and ELP3$_{Y363A}$, while ELP3$_{Y318A}$ shows medium reduction in the hydrolysis, which might be linked to its weaker tRNA binding propensity. Altogether, the results show that these residues are important in the reaction.

Biochemical characterizations of pathogenic ELP3 variants

I initially established the expression system that allows producing intact and active ELP123 and ELP456 (more details on ELP456 are published in Jaciuk et al., 2023). I employed this system to investigate the impact of pathogenic ELP3 variants that are derived from patients suffering from neurodegenerative diseases (R454K, R473K, I298S and R139H) and cancer (R242K, R402T and D443N) using our *in vitro* assays. First, I analyzed the sequence conservation of the residues and mapped the residues in the structural model of ELP123 (Figure 47). Arg473 and Arg454 are conserved residues among all ELP3 proteins, whiles Arg139, Ile298 and Asp443 are only conserved in eukaryotic ELP3s. This observation coincides with the function/location of the residues, because Arg139, Ile298 and Asp443 are located outside of the core of ELP3 and seem to be in contact with ELP1 or ELP2 subunit, respectively. Bacterial and archaeal ELP3 are "stand-alone" proteins without the support from other subunits and there the respective positions appear to be functionally less important. As the highly conserved Arg454 and Arg473 reside in the KAT domain and face the rSAM domain, they are likely to support the formation of the domain interface and their relative positioning. Arg242 and Arg402 are also conserved and located close to the ASL. Hence, the affected residues are likely to contribute to stabilizing the unwound structure of ASL upon tRNA binding.
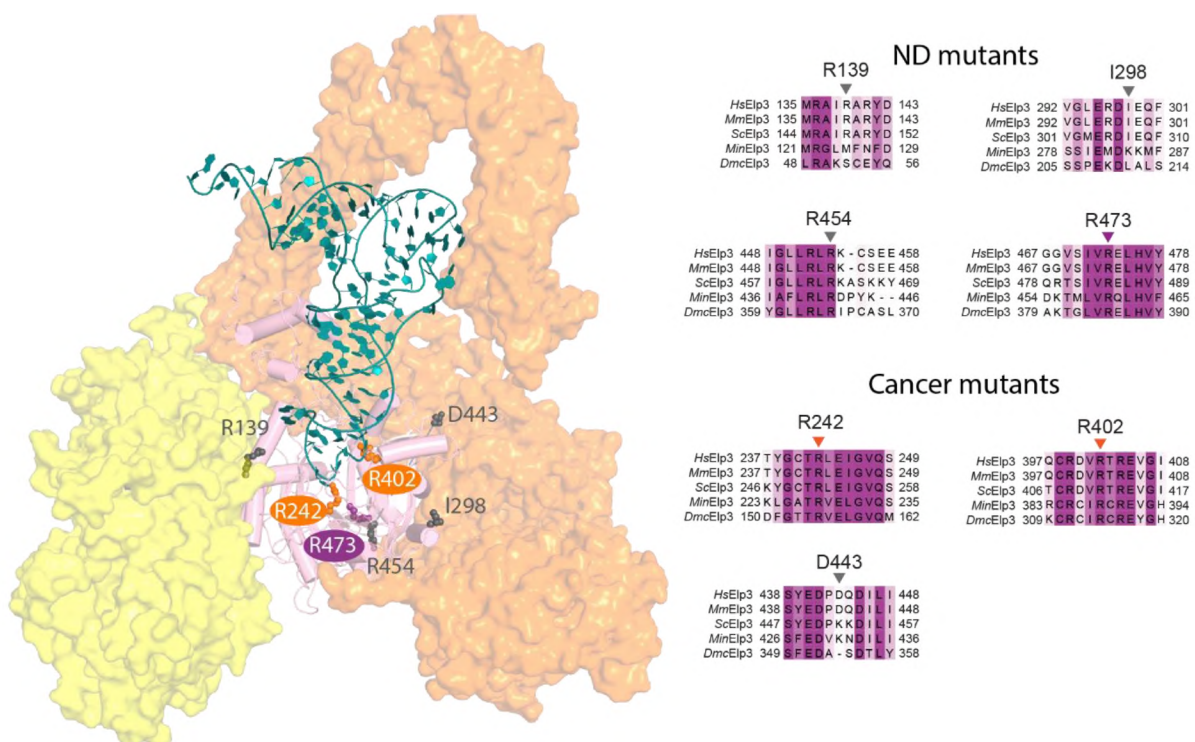

Figure 487. Study of Cancer and neurodegenerative mutants. Cartography of the disease mutants, in grey are the ones that could not be expressed, in orange are the cancer mutants and in purple the ND mutants. On the right are the MUSCLE alignments showing the conservation of the residues.

I generated all disease-related mutants and the yields of R242K and R402T are comparable to wild-type, whereas I298S and R473K resulted in strongly reduced protein levels (Figure 48). I failed to obtain R454K after gel filtration step, suggesting an even stronger destabilizing effect of the substitution. In addition, I298S and R473K display an incorrect stoichiometry, indicating the formation of an instable complex. These observations are in line with the prediction that I298S, R454K and R473K render the complex formation - thus possibly diminishing the expression level of ELP123 in patient's cells. I further investigated the impact of R242K and R402T on enzyme activity. The results show that both mutations still retain comparable tRNA affinity but fail to hydrolyze ACO in the presence of tRNA.
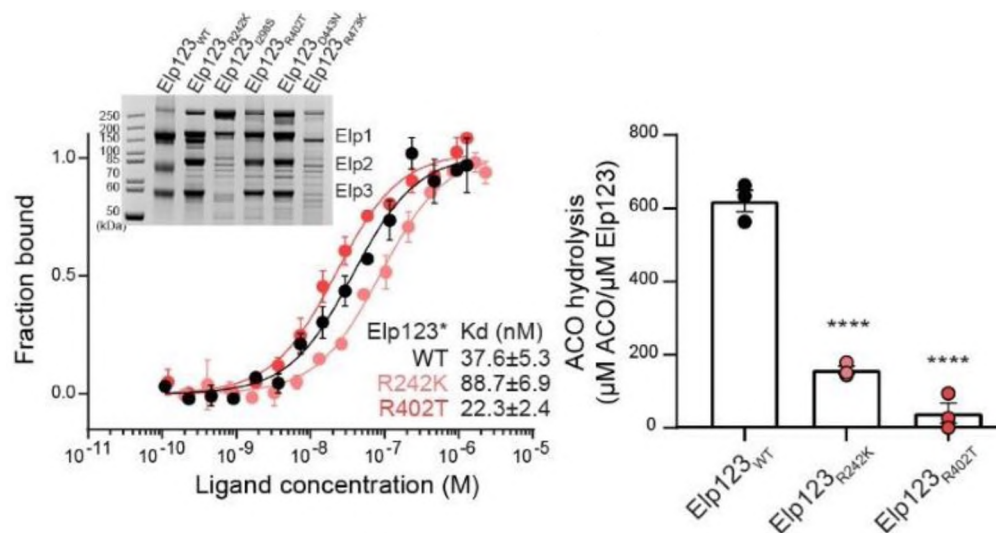

Figure 48. **Biochemical characterizations of clinically relevant ELP3 mutants.** (left) MST analyses on tRNA^{Gln} with Elp123 proteins. An SDS-PAGE in inset show the complex quality after purification. The calculated K_Ds are listed in inset. (right) ACO hydrolysis rate of WT and mutants by tRNA^{Gln}. N=3 Statistical analysis: One-way ANOVA. Statistically significant differences are indicated (****$p \leq 0.0005$). Data represent mean ± SEM.

The eukaryotic Elongator complex, originally annotated as a protein acetylase, is now proven to be a tRNA modifier that attaches cm^5 to uridines in the wobble position. Several structural and biochemical details have already been demonstrated using proteins from model organisms, including yeast and mouse, but the details of the human complex have remained elusive. As the complex is clinically relevant for various severe human diseases, the here described work on the human complex has far reaching for the structure-function analyses of patient-derived mutations.
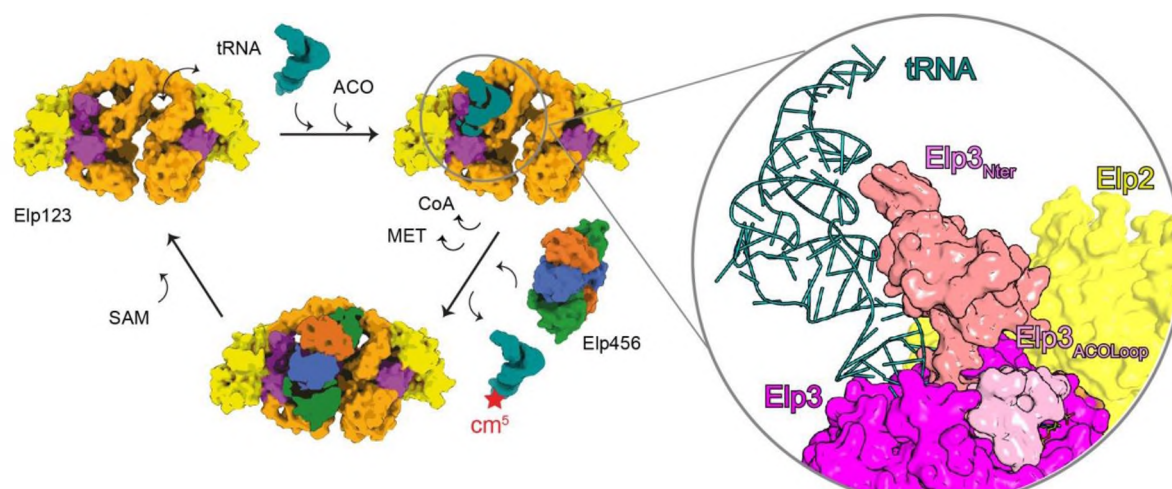

Figure 509. **Summary of the cooperation of ELP123 and ELP456 in catalyzing modification on tRNA**. Each subunit is color-coded as ELP1 in orange, ELP2 in yellow, ELP3 in magenta, ELP4 is green, ELP5 in blue and ELP6 in brown. The zoom-in view presents the stabilized structures of ELP3, including ELP3$_{Nter}$ and ELP3$_{ACOLoop}$ upon tRNA binding. The ACO is positioned in the binding site.

This study presents several cryo-EM structures. of different reaction intermediates, including the pre-substrate state (Elp123) and various substrate-bound states (e.g., tRNA-Elp123-DCA). The results allow to depict a sequential order of the catalytic states and their regulation (Figure 49). Combined with biochemical and *in vivo* functional analyses, my results confirm that Elp123 selectively binds to tRNA substrates without requiring a consensus sequence motif. However, I unexpectedly identified the invariant U_{33} nucleotide, present in almost all tRNAs, as the main determinant to trigger ACO hydrolysis. My molecular investigations also pinpoint to a cluster of residues responsible for transferring the hydrolyzed ACO across domains to facilitate cm^5 addition at U_{34}. However, I could not detect any cm^5U formation from the *in vitro* reaction or obtain the structure of the fully assembled human Elongator complex (Elp1-6). The former is likely due to low reaction efficiency or other components that are required to facilitate the chemical reaction (e.g., priming modifications at other positions). The determination of the cryo-EM structure of human ELP123456 was

impeded by highly dynamic subcomplexes interaction, visible in complementary cross-linking mass spectrometry studies by our collaborations partners. Finally, I also characterized several reported clinically relevant ELP3 variants and provide a possible molecular explanation for the reduced human enzyme activity and a link to disease formation.
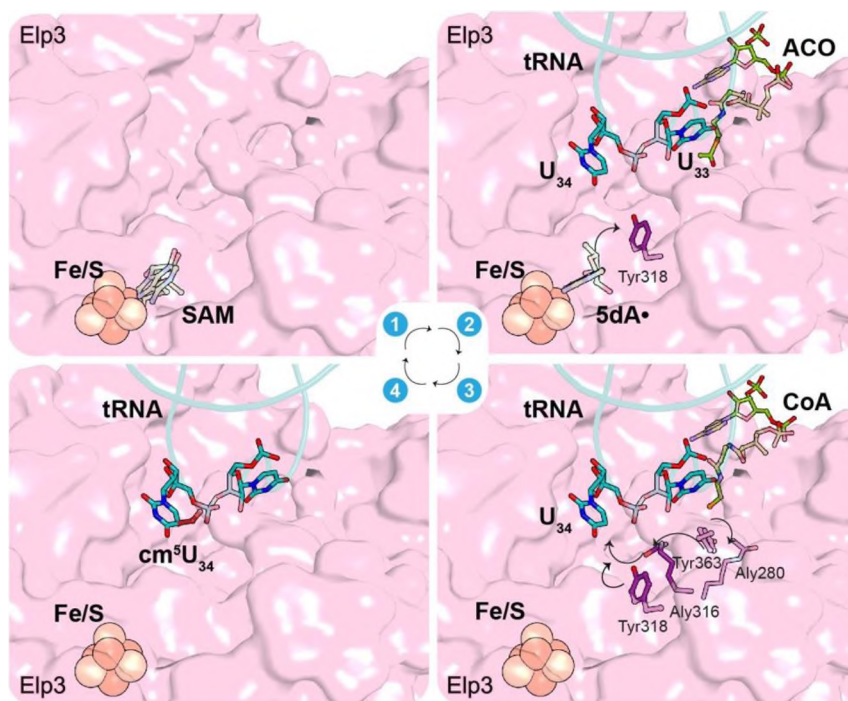

Figure 50. **Summary of ACO hydrolysis and transfer for cm⁵U addition**. (1) ELP3 harbors an iron-sulfur cluster and SAM is positioned. (2) tRNA binding allows the binding of ACO and triggers SAM cleavage to produce 5-dA• radical. (3) U33 triggers ACO hydrolysis and generates CoA and acetyl group which is attached to lysine residues as ALY280 and ALY316. The acetyl group reacts with the 5-dA• radical to form a radical acetyl group which attacks the C5 of U_{34} to form the cm⁵U_{34}. ELP3 is depicted with surface representation in pink.

To summarize the sequential order of the chemical reaction, the details are as follows (Figure 49). First, the bilobed ELP123 structure seems to be relatively mobile, and it is only stabilized when tRNA is recognized. The binding of tRNA is orchestrated via ELP1 and ELP3, where the C-terminus of Elp1 interacts with the elbow region, while the N-terminus and the core of Elp3 interact with the ASL region. This extensive contact area ensures that the ASL of tRNA is positioned properly in the catalytic pocket of ELP3. tRNA binding also stabilizes the N-terminus of ELP3, which leads to the rearrangement of the ACO loop and promotes the binding of ACO. Hydrolysis of ACO is then triggered by the tRNA-identification mark and universally conserved U_{33} nucleotide (Figure 50). The binding of SAM seems to be independent of tRNA recruitment, but SAM is also cleaved upon tRNA binding. Subsequently, the hydrolyzed acetyl group is transferred via a linearly arranged cluster of residues from the

KAT domain to the rSAM domain, where it interacts with the radical adenine to form an acetyl radical. Finally, the activated acetyl group is added to position C5 of U_{34}, forming cm^5U_{34}.

Discussion

In the previous sections, I presented the current status of my work that I performed during the experimental part of my PhD thesis and compared them to the latest results from the group regarding the structure and function of the yeast and mouse Elongator complexes. Here, I seek to address and answer the most essential questions when working with the human Elongator complex. Furthermore, I try discussing the obtained results in the light of all available literature and define a set of open issues that need to be resolved in the future.

Unique Elongator-mediated substrate recognition and reaction

From the work on MinElp3, we partially validated our first hypothesis. Indeed, while the cleft between the SAM and the KAT domain is partly responsible for the tRNA binding, the N-terminus of Elp3 is also heavily involved in the recognition. Although, all Elp3s are highly similar in their protein sequences, the N-termini are way less conserved compared to rSAM or KAT domains. They are different in sequence and length – for instance, a bacterial Elp3 has only 10 N-terminal residues, whereas the human ELP3 possesses a 93-residue N-terminus. The N-terminal motifs in yeast, mouse and human share very low sequence identity, but consistently three helices have been predicted (Dauden et al., 2019; Jaciuk et al., 2023). They seem to serve the same function, namely, to bind/stabilize tRNA by contacting the phosphate backbone of tRNA. This observation suggests that this interaction does not rely on specific sequence motifs but on the recognition of the overall tRNA shape/structure. Of note, it is difficult to imagine how the bacterial Elp3 recognizes tRNA substrate in a similar way, as its N-terminus might not provide sufficient interactions (Glatt et al., 2016). It is also worth mentioning that the C terminus of ELP1 can also interact with tRNA and for a time we believed that it was necessary for tRNA recruitment but truncation of the region, while very difficult to express, did not reduce the tRNA affinity of the complex (Jaciuk et al., 2023). Our more recent models gave us better structural information suggesting a sequence-independent interaction between tRNA and the protein, more for guiding the tRNA than binding it.

Accumulating results have shown that Elongator is a tRNA modifying enzyme (Dauden et al., 2018; Huang et al., 2005; T.-Y. Lin et al., 2019; Selvadurai et al., 2014). The second aim of this work was to identify a sequence of events that lead from the unmodified tRNA to the modified one. Our study, contrary to our hypothesis, suggests that the tRNA binds first to Elp3 before the ACO enters the KAT domain to be hydrolyzed. In fact, the first tRNA bound structure we managed to obtain had a hydrolyzed ACO mimic in the mix (DCA). From our

various trials, we know that obtaining a tRNA-Elongator structure is not possible, which suggests that the ACO blocking loop must be closed from a previous hydrolysis to allow the N-terminus of Elp3 to accept the tRNA in the binding pocket. The hydrolyzed molecule can then be released and replaced with a new ACO. Elongator recognizes the characteristic L-shaped tRNA architecture by Elp1 contacting the elbow region in a sequence-independent manner, while Elp3 binds the D-arm with its N-terminus and accommodates the ASL in the catalytic pocket. This shape-recognition mechanism allows Elongator to bind all tRNAs. The ASL is then distorted and forms a non-canonical conformation to flip out nucleobases, where U_{33} triggers the ACO hydrolysis and U_{34} receives the modification. All tested human U_{34}-containing tRNAs in this study can trigger ACO hydrolysis *in vitro* at various rates. The different induction levels of each tRNA can be explained by how well the ASL is deformed. The deformation may be also dependent on other tRNA modifications, such as methylation at position C_{32} or pseudouridine at position U_{39} to regulate the local structure of the ASL.

This feature of enzyme-induced changes to the tRNA structure has also been observed in many other tRNA modifying enzymes. The distortions can take place locally near the modified nucleotide or even in regions distal to the target site. For instance, the Dus enzyme from *Thermus thermophilus* catalyzes the modification on position 20 and the binding of Dus to tRNA only causes the deformation of the D-arm to flip out the target nucleotide (Yu et al., 2011). The eukaryotic ADAT 2/3 deaminase, which edits the A_{34} to I_{34}, was shown to bind and distort the ASL into a non-canonical conformation. In detail, ADAT3 has two domains linked by not one but two protein linkers, the N-terminal part of Adat 3 binds to the D loop on the elbow region of the tRNA and directs it so the ASL binds in the pocket created between the Adat2 and Adat3 proteins. In this case the interaction of Adat3 with C56 in the T loop, G19 in the D loop and the D arm in the elbow region helps distort the tRNA from the D loop to the ASL to allow for a better alignment of the nucleic acids to the catalytic residues in the binding pocket (Dolce et al., 2022).

In general, the specific target base needs to be exposed to the catalytic site to facilitate the modification. In case of the Elongator-mediated reaction, both U_{33} and U_{34} are flipped out. Position 33 of tRNAs is unique in two ways. First, position 33 is always a uridine except for the initiator Met tRNA (f-tMet) (Marck & Grosjean, 2002; Sprinzl et al., 1998). The invariant U_{33} is beneficial for translation regulation in ribosome that can ensure the tRNA translation to the P site (Ashraf et al., 1999). Second, U_{33} is kept unmodified in almost all known tRNAs

except for the mitochondrial tRNA^{Trp} from a protozoan *Leishmania tarentolae* which carries a thiolated U$_{33}$ (Boccaletto et al., 2022; Crain et al., 2002). In the case of Elongator, the affinity to the protein is not affected but the capacity to trigger the ACO hydrolysis plummets. This data, together with the high-resolution structure showing the orientation of U33 towards ACO, shows that this residue is used as a platform for the modification of U34. This stratagem allows U34 to stay in place facing the iron-sulphur cluster and be closer to the radical released by SAM. The ACO hydrolysis and the SAM cleavage can then be performed in a synchronized manner and the products of each reaction can reach the lysine 316 that is the closest to U34 to be available and be added on the carbon 5 of the Uridine 34.

Despite our efforts, we could not find a reliable method to study the cleavage of SAM in the SAM domain or the catalytic reaction occurring in this domain. From our results we know that the ACO hydrolysis is independent from the SAM cleavage (T.-Y. Lin et al., 2019). We also know that we can co-purify SAM or 5-dA• from insect cells. In our structures, we found an average of SAM and 5-dA• density in the *Hs*Elp123-tRNA- ACO and *Hs*Elp123-tRNA-ECA structures, while for *Hs*Elp123-tRNA-DCA, form 2 had a density for 5-dA• while form 1 had also had an average density of both 5dA and SAM (unpublished data). Since we did not supplement the samples with SAM, the presence of 5-dA• could come from a residual reaction that happened in the insect cells as well as from the interaction with the supplied human tRNA.

The third aim of this work was to determine if the eukaryotic ELP3 and archaeal Elp 3 had the same catalytic mechanism. According to these results, MinElp3 and *Hs*ELP3 do not differ much: the enzyme still selectively hydrolyses ACO in presence of tRNA, the affinity for tRNA is still very high and the structures, when supposed, are conserved. The human protein is however more fragile, it cannot be expressed without co-expression of at least ELP1, its stability at room temperature does not exceed 30 minutes (when MinElp3 is stable for several hours and can be exposed to higher temperatures). The activity of *Hs*ELP3 is more difficult to measure because of time constraints and little amounts of proteins. Some of the studied mutants in the Human construct also showed unexpected behavior, for example C110S/C112S, situated in the SAM domain, has been previously studied in MinElp3 and showed no change in tRNA binding or ACO activity compared to the WT while in Human, the ACO hydrolysis was significantly lowered compared to WT (T.-Y. Lin et al., 2019). This result suggests that the SAM and KAT domains in *Hs*ELP3 are much more cooperative and the slightest change in the

protein will lead to negative consequences on the activity.

Lastly, a recent study reports an unconventional role of Elongator, controlling microtubule and asymmetric spindle formation in *Drosophila melanogaster* (Planelles-Herrero et al., 2022). This unexpected activity is independent from the SAM cleavage or ACO hydrolysis activity. Instead, it relies on the Elongator interaction with the microtubule to control the polarization speed. However, how the Elongator structurally binds to microtubule is not clear, yet. Whether this is a specific mechanism *Drosophila melanogaster* neuron or also happens in human cells still requires further investigations.

Cryo-EM captures multiple conformations of Elongator.

Most tRNA modifying enzymes are either monomeric proteins, homo/heterodimers or heterotetrametric complexes. Examples are the monomeric ribonuclease I, the homodimer pseudouridine synthase 3 or heterotetrametric MnmE/MnmG complex (J. Chen & Patton, 2000; Hur & Stroud, 2007; Keller et al., 2019; Przykorska et al., 1992; R. Shi et al., 2009; Wang & He, 2014). Over the last decades, macromolecular crystallography was the preferred structural biology method, which revealed structures of some apo proteins as well as tRNA-bound complexes (Hoang & Ferré-D'Amaré, 2001; Krutyhołowa et al., 2019; López-Estepa et al., 2015; Qiu et al., 2019; Schmeing et al., 2003; Takagi et al., 2020). Due to the limitations of forming crystals with full-length tRNA, the bound tRNA substrate was most often mimicked by a fragment of the tRNA (e.g., bacterial tRNA deaminase A (TadA) with a ASL of tRNA [PDB 2B3J]). To date, there is still only a limited numbers of crystal structures of tRNA-enzyme complex in PDB (e.g., bacterial pseudouridine synthase TruA-tRNA complex [PDB 2NR0]), the reason becomes apparent with some experience in the field of crystallography (Hur & Stroud, 2007; Karijolich & Yu, 2011; Schwalm et al., 2016). Out of thousands of buffer conditions, the conditions allowing the formation of crystals from the protein alone do not necessarily create co-crystals with tRNA. It is also possible to obtains structures using NMR method, but in this case the experimenter is limited by the size of the molecule he can analyze, usually the maximal size that can be analyzed by NMR is 30 kDa but some scientists managed to obtain molecules up to 100kDa (Tugarinov et al., 2002). In the case of tRNA-Elp3 crystallization trials, the need of pure tRNA was too high to be able to be produced and used successfully in screening. The alternative use of an oligonucleotide chain unfortunately was not successful.

Single particle cryo-EM provides an alternative method to obtain structural snapshots of these

highly dynamic and transient complexes in their apo or RNA-bound states. One of the major advantages of cryo-EM is the relatively low demand of sample quantity and the low concentrations used during sample preparation, which are critical bottlenecks for difficult proteins or protein complexes. In contrast to crystallography, which requires extremely homogenous samples and selects for a single conformation during crystal formation, cryo-EM can image multiple status within the same sample. With the recent advent of cryo-EM, many tRNA-free or tRNA-protein complex structures have been reported which has boosted the molecular discovery in the field of tRNA modifications. The mass of the Elongator complex is relatively large compared to other RNA modifying enzymes, which has made the determination of the structure difficult by X-ray crystallography. Using cryo-EM, the rather small quantity of obtainable Elongator complex from insect cells was sufficient for sample preparation and data collection. Thereby, we not only obtained a static high-resolution image of human Elongator, but we also received structural information about the multiple conformations of Elongator after a tRNA molecule is bound by the complex. These structures clearly demonstrate how the individual Elongator subunits form a multicomponent complex, orchestrate substrate binding, and proceed with the catalytic reaction.

The last aim of the work was attainable with the use of cryoEM. I could express and obtain the structure of the Human ELP123 subcomplex and compare it to my colleague's structures of ScElp123 and MmElp123 (Gaik et al., 2022; Jaciuk et al., 2023). While we managed to obtain tRNA-bound structures for all three subcomplexes, the local resolution for tRNA was not as good in yeast and mouse as it is in the human complex, so the model fitting and the interpretation needs to be taken with a grain of salt. Our original assumption was that the subcomplexes work in a similar fashion. Our hypothesis was not entirely correct. While all three subcomplexes contain Elp1, Elp2 and Elp3, interacting in the same manner and can bind tRNA, we can see differences between ScElp123 and *Hs*Elp123 that for one part derive from the difference number of amino acid in Sc compared to Human. The Elp1 C-terminal loop that was studied here was based on the observations in the ScElp123 in the 2019 Elongator paper. With our structure we can see that it is not the loop that interacts with tRNA in *Hs*Elp123 but the alpha helices just above it. The interaction of tRNA with the N-termini is also interesting to observe. As established previously, the amino acid sequence of the N-termini is not conserved and the interaction to tRNA is sequence-independent. The structures also show that while *Hs* and MmElp3 N-terminus interacts with the help of 3 alpha helices with tRNA, the Sc interacts with 4. The pattern of recognition is slightly different between all three species.

Interestingly the core of the proteins, in this tRNA-bound state align perfectly. The slight changes observed in the structures can be based on the interaction with different tRNAs, or simply different stages of the tRNA binding or modification process. The conditions developed during this project are a great template for further investigation of more intermediary catalytic states.

While the results gathered in this study presents deep insight into tRNA binding and the catalytic reaction of Elp3, the reconstitution of the cm^5U modification by human ELP123 *in vitro* still has not be accomplished. Despite extensive efforts by me and several of my colleagues to obtain the cm^5U product, there are still no signs of even minor levels of an ELP123-mediated cm^5U formation. This shows a gap of knowledge that needs to be explored in the future. Many different factors need to be considered - for example, the rate of *in vitro* cm^5U formation by human ELP123 could be very slow or other factors are strictly required for an efficient reaction to occur. In addition, the interaction of ELP123 with the ELP456 subcomplex and the other accessory proteins (e.g., DPH3, KTI12) would benefit from comprehensive structural study in complex with Elongator. The structures and activities or the individual players from model organisms have partially been explored already (Dauden et al., 2019; Krutyhołowa et al., 2019; Z. Lin et al., 2012; Séraphin et al., 2017; H. Xu et al., 2015). Although these accessary proteins contribute to the cm^5U addition via a direct interaction with Elongator (Krutyhołowa et al., 2019), the mechanistic detail of their regulatory function is still not clear. For instance, how, where and at which reaction stage exactly Kti12 interacts with Elp123 still needs further investigation. DPH3 has been proposed to be responsible for electron transfer to iron-sulphur cluster, which is essential for the Elp3 activity (Villahermosa & Fleck, 2017). How DPH3 interacts with Elp123 and whether it contacts the cluster directly is unclear, like the fundamental question how the presence of DPH3 could directly contribute to cm^5U conversion - these burning questions are waiting to be addressed.

While it was possible to purify the endogenous *Sc*Elp123456 complex from high-density yeast cultures grown in large fermenters (Dauden et al., 2018), it was not achievable to isolate the human counterpart from human cells. In addition, it was not possible to isolate the human ELP123456 complex directly from insect cells and it could only be obtained after *in vitro* reconstitution of the purified subcomplex by mixing. A yet unpublished crosslinking mass spectrometry analysis of the human and yeast complexes shows that the human complex has less contact points between the two subcomplexes than the yeast complex. These observations

suggest a slightly different regulation of the interplay between Elp123 and Elp456 in yeast and humans.

One of the originally defined goals of my PhD work was to obtain the structure of Elp123456 with tRNA. Few attempts to reconstitute this intermediate and image it by cryo-EM failed. Later, we found that it is highly unlikely to observe this intermediate at all. The C-terminus of Elp1 was shown to mediate the interaction with either tRNA or Elp456 (Jaciuk et al., 2023). This mutually exclusive interaction is in-line with the observation that Elp456 is to remove tRNAs from ELP123 (Gaik et al., 2022; Glatt & Müller, 2013). Meaning that it is either possible to obtain ELP123 bound to the tRNA (while ELP456 has lose interaction with ELP123) or the full complex devoid of any tRNA substrate.

Expanding knowledge of Elongator from bench side to bed side

My work on the HsELP1$_{K815T}$23 mutant clearly demonstrates that the in vitro characterization of ELP123 can provide a suitable platform to dissect the relevance of known and newly appearing clinically mutations detectable in patients. The mutations located in the core of subunits or at the interface between subunits are most likely to disrupt complex formation or significantly reduce the protein expression level in cells. Whereas mutations near the tRNA binding and catalytic sites most likely abolish the enzymatic activity, which can directly be observed in in vitro assay. With over hundreds of mutants waiting to be investigated, this work presents an opportunity to explain and discriminate between detailed mechanisms of how mutations impede enzyme function. Thereby, it provides causative links and explanations to the observed dysregulation and disease formation. The goal would be to obtain samples from patients and immediately confirm the observations at the bench. However, gaining patient approval to work on primary cell lines derived from their body is difficult and sometimes, when they approve, obtaining the documentation that allows to work on human samples can also take a long time. A potential alternative way is to overexpress the mutant of interest in stable model cell lines (e.g., HEK cells or SV40-dependent immortalization of human embryonic microglial cells [HMC3]), which could allow to monitor the expression and formation of the Elongator complex in human cells.

In contrast to the loss of Elongator activity in neurodegenerative diseases, it is mostly overexpression of Elongator subunits (e.g., ELP3 and ELP4) that is found in cancerous cells. Moreover, a circular RNA (hsa_circ_0001785) is encoded in *ELP3* (circ-ELP3) and its expression is upregulated in breast cancers. circRNAs, a class of non-coding RNAs that is

covalently closed without 5′ and 3′ ends, have higher durability in serum and are considered as biomarkers for disease diagnosis. Therefore, circ-ELP3 has been proposed as a biomarker for breast cancer (Barznegar et al., 2022; Omid-Shafaat et al., 2021). However, the synthesis of circ-Elp3 and its actual biological function(s) in cells are not understood. Whether this is correlated with disease onset or progression still needs to be established.

After the role of the Elongator complex has been studied for many years, some cures for the related diseases have recently started to emerge. For instance, to correct aberrant *Elp1* gene splicing, an exon specific U1 small nuclear RNAs was employed. Its delivery by an engineered adeno-associated virus (AAV) to target intronic sequences was shown to promote splicing and generate the correct mRNA in a mouse model (Romano et al., 2022). In addition, promoting the inclusion of exon 20 during splicing can also be achieved by a small molecule, kinetin, or some proteasome inhibitors to block the protein degradation machinery (Hervé & Ibrahim, 2017; Morini et al., 2019). In general, to rescue the loss of function or to correct gain-of function mutations in Elongator, gene editing by CRISPR-Cas9 systems also appears as a potential therapeutic strategy. Furthermore, enzyme replacement therapy could be an alternative method as well.

All mentioned techniques and approaches have their own advantages and pitfalls (e.g., tissue-specific targeting). In summary, more work and effort are required to circumvent technical and clinical hurdles to provide novel therapeutic solutions for human diseases. Foremost, targeted therapies require a fundamental understanding of the biological function of the affected genes/proteins in health and disease. My work paves the way to understand the tRNA modification activity of Elongator in humans and understand the unfortunate link to severe human diseases.

References

Abbassi, N.-E.-H., Kojic, M., Lin, T.-Y., Jones, A., Wakeling, E. L., Clement, E., Nakou, V., Singleton, M., Dobosz, D., Kaliakatsos, M., Glatt, S., & Wainwright, B. J. (2023). A novel ELP1 mutation impairs the function of the Elongator complex and causes a severe neurodevelopmental phenotype. *J Hum Genet* . https://doi.org/10.1038/s10038-023-01135-3

Abbassi, N., Biela, A., Glatt, S., & Lin, T. (2020). How Elongator acetylates tRNA bases. *Int J Mol Sci*. https://doi.org/10.3390/ijms21218209

Adami, R., & Bottai, D. (2020). S-adenosylmethionine tRNA modification: unexpected/unsuspected implications of former/new players. *International Journal of Biological Sciences*, *16*(15), 3018. https://doi.org/10.7150/IJBS.49302

Adams, P. D., Afonine, P. V., Bunkóczi, G., Chen, V. B., Davis, I. W., Echols, N., Headd, J. J., Hung, L. W., Kapral, G. J., Grosse-Kunstleve, R. W., McCoy, A. J., Moriarty, N. W., Oeffner, R., Read, R. J., Richardson, D. C., Richardson, J. S., Terwilliger, T. C., & Zwart, P. H. (2010). PHENIX: a comprehensive Python-based system for macromolecular structure solution. *Acta Crystallographica Section D: Biological Crystallography*, *66*(Pt 2), 213. https://doi.org/10.1107/S0907444909052925

Addis, L., Ahn, J. W., Dobson, R., Dixit, A., Ogilvie, C. M., Pinto, D., Vaags, A. K., Coon, H., Chaste, P., Wilson, S., Parr, J. R., Andrieux, J., Lenne, B., Tumer, Z., Leuzzi, V., Aubell, K., Koillinen, H., Curran, S., Marshall, C. R., … Pal, D. K. (2015). Microdeletions of ELP4 Are Associated with Language Impairment, Autism Spectrum Disorder, and Mental Retardation. *Human Mutation*, *36*(9), 842–850. https://doi.org/10.1002/humu.22816

Agris, P. F., Narendran, A., Sarachan, K., Väre, V. Y. P. P., & Eruysal, E. (2017). The Role of RNA Modifications in Translational Fidelity. *The Enzymes*, *41*, 1. https://doi.org/10.1016/bs.enz.2017.03.005

Ashraf, S. S., Guenther, R., & Agris, P. F. (1999). Orientation of the tRNA anticodon in the ribosomal P-site: quantitative footprinting with U33-modified, anticodon stem and loop domains. *RNA (New York, N.Y.)*, *5*(9), 1191–1199. https://doi.org/10.1017/S1355838299990933

Bäckström, D., Yutin, N., Jørgensen, S. L., Dharamshi, J., Homa, F., Zaremba-Niedwiedzka, K., Spang, A., Wolf, Y. I., Koonin, E. V., & Ettema, T. J. G. (2019a). Virus genomes from deep sea sediments expand the ocean megavirome and support independent origins of viral gigantism. *MBio, 10*(2). https://doi.org/10.1128/MBIO.02497-18

Bäckström, D., Yutin, N., Jørgensen, S. L., Dharamshi, J., Homa, F., Zaremba-Niedwiedzka, K., Spang, A., Wolf, Y. I., Koonin, E. V., & Ettema, T. J. G. (2019b). Virus genomes from deep sea sediments expand the ocean megavirome and support independent origins of viral gigantism. *MBio, 10*(2). https://doi.org/10.1128/MBIO.02497-18

Barznegar, M., Rahimi, K., Mahdavi, P., Menbari, M.-N. N., Darvishi, N., Vahabzadeh, Z., Hakhamaneshi, M.-S. S., Andalibi, P., & Abdi, M. (2022). Relation between the circular and linear form of the Elongator Acetyltransferase Complex Subunit 3 in the progression of triple-negative breast cancer. *Cell Biochemistry and Function.* https://doi.org/10.1002/cbf.3724

Bateman, A., Martin, M. J., Orchard, S., Magrane, M., Agivetova, R., Ahmad, S., Alpi, E., Bowler-Barnett, E. H., Britto, R., Bursteinas, B., Bye-A-Jee, H., Coetzee, R., Cukura, A., da Silva, A., Denny, P., Dogan, T., Ebenezer, T. G., Fan, J., Castro, L. G., … Teodoro, D. (2021). UniProt: the universal protein knowledgebase in 2021. *Nucleic Acids Research, 49*(D1), D480–D489. https://doi.org/10.1093/NAR/GKAA1100

Bepler, T., Kelley, K., Noble, A. J., & Berger, B. (2020). Topaz-Denoise: general deep denoising models for cryoEM and cryoET. *BioRxiv,* 838920. https://doi.org/10.1101/838920

Bjork, G. R., Esberg, A., Johansson, M. J. O., Huang, B., & Bystrom, A. S. (2008). Eukaryotic Wobble Uridine Modifications Promote a Functionally Redundant Decoding System. *Molecular and Cellular Biology, 28*(10), 3301–3312. https://doi.org/10.1128/mcb.01542-07

Boccaletto, P., Stefaniak, F., Ray, A., Cappannini, A., Mukherjee, S., Purta, E., Kurkowska, M., Shirvanizadeh, N., Destefanis, E., Groza, P., Avşar, G., Romitelli, A., Pir, P., Dassi, E., Conticello, S. G., Aguilo, F., & Bujnicki, J. M. (2022). MODOMICS: a database of RNA modification pathways. 2021 update. *Nucleic Acids Res ., 50*(D1), D231–D235. https://doi.org/10.1093/NAR/GKAB1083

Broderick, J. B., Duffus, B. R., Duschene, K. S., & Shepard, E. M. (2014). Radical S-adenosylmethionine enzymes. *Chemical Reviews*, *114*(8), 4229–4317. https://doi.org/10.1021/cr4004709

Carlile, T. M., Rojas-Duran, M. F., Zinshteyn, B., Shin, H., Bartoli, K. M., & Gilbert, W. V. (2014). Pseudouridine profiling reveals regulated mRNA pseudouridylation in yeast and human cells. *Nature*, *515*(7525), 143–146. https://doi.org/10.1038/NATURE13802

Chen, C., Huang, B., Anderson, J. T., & Byström, A. S. (2011). Unexpected Accumulation of ncm5U and ncm5s2U in a trm9 Mutant Suggests an Additional Step in the Synthesis of mcm5U and mcm5s2U. *PLOS ONE*, *6*(6), e20783. https://doi.org/10.1371/JOURNAL.PONE.0020783

Chen, C., Tuck, S., & Byström, A. S. (2009). Defects in tRNA modification associated with neurological and developmental dysfunctions in Caenorhabditis elegans elongator mutants. *PLoS Genetics*, *5*(7). https://doi.org/10.1371/JOURNAL.PGEN.1000561

Chen, J., & Patton, J. R. (2000). Pseudouridine synthase 3 from mouse modifies the anticodon loop of tRNA. *Biochemistry*, *39*(41), 12723–12730. https://doi.org/10.1021/BI001109M

Chen, L., Wang, W.-J., Liu, Q., Wu, Y.-K., Wu, Y.-W., Jiang, Y., Liao, X.-Q., Huang, F., Li, Y., Shen, L., Yu, C., Zhang, S.-Y., Yan, L.-Y., Qiao, J., Sha, Q.-Q., & Fan, H.-Y. (2022). NAT10-mediated N 4-acetylcytidine modification is required for meiosis entry and progression in male germ cells. *Nucleic Acids Research*, *50*(19), 10896–10913. https://doi.org/10.1093/nar/gkac594

Chimnaronk, S., Suzuki, T., Manita, T., Ikeuchi, Y., Yao, M., Suzuki, T., & Tanaka, I. (2009). RNA helicase module in an acetyltransferase that modifies a specific tRNA anticodon. *The EMBO Journal*, *28*(9), 1362–1373. https://doi.org/10.1038/EMBOJ.2009.69

Cohen, J. S., Srivastava, S., Farwell, K. D., Lu, H. M., Zeng, W., Lu, H., Chao, E. C., & Fatemi, A. (2015). ELP2 is a novel gene implicated in neurodevelopmental disabilities. *American Journal of Medical Genetics. Part A*, *167*(6), 1391–1395. https://doi.org/10.1002/AJMG.A.36935

Crain, P. F., Alfonzo, J. D., Rozenski, J., Kapushoc, S. T., McCloskey, J. A., & Simpson, L. (2002). Modification of the universally unmodified uridine-33 in a mitochondria-imported

edited tRNA and the role of the anticodon arm structure on editing efficiency. *RNA, 8*(6), 752. https://doi.org/10.1017/S1355838202022045

Dai, Q., Zhang, L. S., Sun, H. L., Pajdzik, K., Yang, L., Ye, C., Ju, C. W., Liu, S., Wang, Y., Zheng, Z., Zhang, L., Harada, B. T., Dou, X., Irkliyenko, I., Feng, X., Zhang, W., Pan, T., & He, C. (2022). Quantitative sequencing using BID-seq uncovers abundant pseudouridines in mammalian mRNA at base resolution. *Nature Biotechnology 2022*, 1–11. https://doi.org/10.1038/s41587-022-01505-w

Dauden, M. I., Jaciuk, M., Müller, C. W., & Glatt, S. (2018). Structural asymmetry in the eukaryotic Elongator complex. *FEBS Letters, 592*(4), 502–515. https://doi.org/10.1002/1873-3468.12865

Dauden, M. I., Jaciuk, M., Weis, F., Lin, T. Y., Kleindienst, C., Abbassi, N. E. H., Khatter, H., Krutyholowa, R., Breunig, K. D., Kosinski, J., Müller, C. W., & Glatt, S. (2019). Molecular basis of tRNA recognition by the Elongator complex. *Science Advances, 5*(7), 1–14. https://doi.org/10.1126/sciadv.aaw2326

De Crécy-Lagard, V., Boccaletto, P., Mangleburg, C. G., Sharma, P., Lowe, T. M., Leidel, S. A., & Bujnicki, J. M. (2019). Matching tRNA modifications in humans to their known and predicted enzymes. *Nucleic Acids Research, 47*(5), 2143. https://doi.org/10.1093/NAR/GKZ011

Deeg, C. M., Chow, C. E. T., & Suttle, C. A. (2018). The kinetoplastid-infecting bodo saltans virus (Bsv), a window into the most abundant giant viruses in the sea. *ELife, 7*. https://doi.org/10.7554/ELIFE.33014

Delaunay, S., Rapino, F., Tharun, L., Zhou, Z., Heukamp, L., Termathe, M., Shostak, K., Klevernic, I., Florin, A., Desmecht, H., Desmet, C. J., Nguyen, L., Leidel, S. A., Willis, A. E., Büttner, R., Chariot, A., & Close, P. (2016). Elp3 links tRNA modification to IRES-dependent translation of LEF1 to sustain metastasis in breast cancer. *Journal of Experimental Medicine, 213*(11), 2503–2523. https://doi.org/10.1084/jem.20160397

Dolce, L. G., Zimmer, A. A., Tengo, L., Weis, F., Rubio, M. A. T., Alfonzo, J. D., & Kowalinski, E. (2022). Structural basis for sequence-independent substrate selection by eukaryotic wobble base tRNA deaminase ADAT2/3. *Nature Communications, 13*(1).

https://doi.org/10.1038/s41467-022-34441-z

Dong, C., Lin, Z., Diao, W., Li, D., Chu, X., Wang, Z., Zhou, H., Xie, Z., Shen, Y., & Long, J. (2015). The Elp2 Subunit Is Essential for Elongator Complex Assembly and Functional Regulation. *Structure*, *23*(6), 1078–1086. https://doi.org/10.1016/j.str.2015.03.018

Dyubankova, N., Sochacka, E., Kraszewska, K., Nawrot, B., Herdewijn, P., & Lescrinier, E. (2015). Organic & Biomolecular Chemistry Contribution of dihydrouridine in folding of the D-arm in tRNA †. *Org. Biomol. Chem*, *13*, 4960. https://doi.org/10.1039/c5ob00164a

Fellows, J., Erdjument-Bromage, H., Tempst, P., & Svejstrup, J. Q. (2000). The Elp2 subunit of elongator and elongating RNA polymerase II holoenzyme is a WD40 repeat protein. *The Journal of Biological Chemistry*, *275*(17), 12896–12899. https://doi.org/10.1074/JBC.275.17.12896

Fernández-Vázquez, J., Vargas-Pérez, I., Sansó, M., Buhne, K., Carmona, M., Paulo, E., Hermand, D., Rodríguez-Gabriel, M., Ayté, J., Leidel, S., & Hidalgo, E. (2013). Modification of tRNALysUUU by Elongator Is Essential for Efficient Translation of Stress mRNAs. *PLoS Genetics*, *9*(7). https://doi.org/10.1371/JOURNAL.PGEN.1003647

Fischer, M. G., Allen, M. J., Wilson, W. H., & Suttle, C. A. (2010). Giant virus with a remarkable complement of genes infects marine zooplankton. *Proceedings of the National Academy of Sciences of the United States of America*, *107*(45), 19508–19513. https://doi.org/10.1073/PNAS.1007615107

Fleming, B. A., Blango, M. G., Rousek, A. A., Kincannon, W. M., Tran, A., Lewis, A. J., Russell, C. W., Zhou, Q., Baird, L. M., Barber, A. E., Brannon, J. R., Beebout, C. J., Bandarian, V., Hadjifrangiskou, M., Howard, M. T., & Mulvey, M. A. (2022). A tRNA modifying enzyme as a tunable regulatory nexus for bacterial stress responses and virulence. *Nucleic Acids Research*, *50*(13), 7570–7590. https://doi.org/10.1093/NAR/GKAC116

Frenkel-Morgenstern, M., Danon, T., Christian, T., Igarashi, T., Cohen, L., Hou, Y. M., & Jensen, L. J. (2012). Genes adopt non-optimal codon usage to generate cell cycle-dependent oscillations in protein levels. *Molecular Systems Biology*, *8*. https://doi.org/10.1038/MSB.2012.3

Gaik, M., Kojic, M., Stegeman, M. R., Öncü-Öner, T., Kościelniak, A., Jones, A., Mohamed, A., Chau, P. Y. S., Sharmin, S., Chramiec-Głąbik, A., Indyka, P., Rawski, M., Biela, A., Dobosz, D., Millar, A., Chau, V., Ünalp, A., Piper, M., Bellingham, M. C., … Glatt, S. (2022). Functional divergence of the two Elongator subcomplexes during neurodevelopment. *EMBO Molecular Medicine*, *14*(7). https://doi.org/10.15252/EMMM.202115608

Gaik, M., Kojic, M., Wainwright, B. J., & Glatt, S. (2023). Elongator and the role of its subcomplexes in human diseases. *EMBO Molecular Medicine*, *15*(2). https://doi.org/10.15252/EMMM.202216418

Gao, W., Gallardo-Dodd, C. J., & Kutter, C. (2022). *Cell type-specific analysis by single-cell profiling identifies a stable mammalian tRNA-mRNA interface and increased translation efficiency in neurons*. https://doi.org/10.1101/gr.275944.121

Glatt, S., Létoquart, J., Faux, C., Taylor, N. M. I., Séraphin, B., & Müller, C. W. (2012). The Elongator subcomplex Elp456 is a hexameric RecA-like ATPase. *Nature Structural and Molecular Biology*, *19*(3), 314–320. https://doi.org/10.1038/nsmb.2234

Glatt, S., & Müller, C. W. (2013). Structural insights into Elongator function. *Current Opinion in Structural Biology*, *23*(2), 235–242. https://doi.org/10.1016/j.sbi.2013.02.009

Glatt, S., Zabel, R., Kolaj-Robin, O., Onuma, O. F., Baudin, F., Graziadei, A., Taverniti, V., Lin, T. Y., Baymann, F., Séraphin, B., Breunig, K. D., & Müller, C. W. (2016). Structural basis for tRNA modification by Elp3 from Dehalococcoides mccartyi. *Nature Structural and Molecular Biology*, *23*(9), 794–802. https://doi.org/10.1038/nsmb.3265

Han, L., & Phizicky, E. M. (2018). A rationale for tRNA modification circuits in the anticodon loop. *RNA*, *24*(10), 1277–1284. https://doi.org/10.1261/rna.067736.118

Hanashima, C., Nishimura, T., Nakamura, H., & Stern, C. D. (2016). Time in Development. *Development Growth and Differentiation*, *58*(1), 3–5. https://doi.org/10.1111/DGD.12265

Hellen, C. U. T. (2018). Translation Termination and Ribosome Recycling in Eukaryotes. *Cold Spring Harbor Perspectives in Biology*, *10*(10), a032656. https://doi.org/10.1101/CSHPERSPECT.A032656

Hervé, M., & Ibrahim, E. C. (2017). Proteasome inhibitors to alleviate aberrant IKBKAP mRNA splicing and low IKAP/hELP1 synthesis in familial dysautonomia. *Neurobiology of Disease, 103*, 113–122. https://doi.org/10.1016/J.NBD.2017.04.009

Hoang, C., & Ferré-D'Amaré, A. R. (2001). Cocrystal structure of a tRNA Psi55 pseudouridine synthase: nucleotide flipping by an RNA-modifying enzyme. *Cell, 107*(7), 929–939. https://doi.org/10.1016/S0092-8674(01)00618-3

Hoffmann, N. A., Jakobi, A. J., Moreno-Morcillo, M., Glatt, S., Kosinski, J., Hagen, W. J. H., Sachse, C., & Müller, C. W. (2015). Molecular structures of unbound and transcribing RNA polymerase III. *Nature, 528*(7581), 231–236. https://doi.org/10.1038/nature16143

Holley, R. W., Apgar, J., Everett, G. A., Madison, J. T., Marquisee, M., Merrill, S. H., Penswick, J. R., & Zamir, A. (1965). STRUCTURE OF A RIBONUCLEIC ACID. *Science (New York, N.Y.), 147*(3664), 1462–1465. https://doi.org/10.1126/SCIENCE.147.3664.1462

Huang, B., Johansson, M. J. O. O., & Byström, A. S. (2005). An early step in wobble uridine tRNA modification requires the Elongator complex. *Rna, 11*(4), 424–436. https://doi.org/10.1261/rna.7247705

Huber, S. M., Leonardi, A., Dedon, P. C., & Begley, T. J. (2019). The Versatile Roles of the tRNA Epitranscriptome during Cellular Responses to Toxic Exposures and Environmental Stress. *Toxics, 7*(1). https://doi.org/10.3390/TOXICS7010017

Hur, S., & Stroud, R. M. (2007). How U38, 39, and 40 of many tRNAs become the targets for pseudouridylation by TruA. *Molecular Cell, 26*(2), 189–203. https://doi.org/10.1016/J.MOLCEL.2007.02.027

Ishida, K., Kunibayashi, T., Tomikawa, C., Ochi, A., Kanai, T., Hirata, A., Iwashita, C., & Hori, H. (2011). Pseudouridine at position 55 in tRNA controls the contents of other modified nucleotides for low-temperature adaptation in the extreme-thermophilic eubacterium Thermus thermophilus. *Nucleic Acids Research, 39*(6), 2304. https://doi.org/10.1093/NAR/GKQ1180

Ito, S., Akamatsu, Y., Noma, A., Kimura, S., Miyauchi, K., Ikeuchi, Y., Suzuki, T. T. T., & Suzuki, T. T. T. (2014). A single acetylation of 18 S rRNA is essential for biogenesis of the small ribosomal subunit in saccharomyces cerevisiae. *Journal of Biological Chemistry,*

289(38), 26201–26212. https://doi.org/10.1074/jbc.M114.593996

Jaciuk, M., Scherf, D., Kaszuba, K., Gaik, M., Rau, A., Kościelniak, A., Krutyhołowa, R., Rawski, M., Indyka, P., Graziadei, A., Chramiec-Głąbik, A., Biela, A., Dobosz, D., Lin, T.-Y., Abbassi, N.-E.-H., Hammermeister, A., Rappsilber, J., Kosinski, J., Schaffrath, R., & Glatt, S. (2023). Cryo-EM structure of the fully assembled Elongator complex. *Nucleic Acids Research*. https://doi.org/10.1093/NAR/GKAC1232

Jumper, J., Evans, R., Pritzel, A., Green, T., Figurnov, M., Ronneberger, O., Tunyasuvunakool, K., Bates, R., Žídek, A., Potapenko, A., Bridgland, A., Meyer, C., Kohl, S. A. A., Ballard, A. J., Cowie, A., Romera-Paredes, B., Nikolov, S., Jain, R., Adler, J., … Hassabis, D. (2021). Highly accurate protein structure prediction with AlphaFold. *Nature 2021 596:7873*, *596*(7873), 583–589. https://doi.org/10.1038/s41586-021-03819-2

Kaiser, C. M., & Liu, K. (2018). Folding up and Moving on—Nascent Protein Folding on the Ribosome. *Journal of Molecular Biology*, *430*(22), 4580–4591. https://doi.org/10.1016/J.JMB.2018.06.050

Karijolich, J., & Yu, Y.-T. T. (2011). Converting nonsense codons into sense codons by targeted pseudouridylation. *Nature*, *474*(7351). https://doi.org/10.1038/nature10165

Keller, C., Chattopadhyay, M., & Tabor, H. (2019). Absolute requirement for polyamines for growth of Escherichia coli mutants (mnmE/G) defective in modification of the wobble anticodon of transfer-RNA One sentence summary: Escherichia coli mutants (mnmE/G) defective in transfer-RNA modification need polyamines for growth. *FEMS Microbiology Letters*, *366*, 110. https://doi.org/10.1093/femsle/fnz110

Kelley, L. A., Mezulis, S., Yates, C. M., Wass, M. N., & Sternberg, M. J. E. (2015). The Phyre2 web portal for protein modeling, prediction and analysis. *Nature Protocols 2015 10:6*, *10*(6), 845–858. https://doi.org/10.1038/nprot.2015.053

Kidmose, R. T., Juhl, J., Nissen, P., Boesen, T., Karlsen, J. L., & Pedersen, B. P. (2019). Namdinator - automatic molecular dynamics flexible fitting of structural models into cryo-EM and crystallography experimental maps. *IUCrJ*, *6*(Pt 4), 526–531. https://doi.org/10.1107/S2052252519007619

Kimura, S., & Suzuki, T. (2015). Iron-sulfur proteins responsible for RNA modifications.

Biochimica et Biophysica Acta - Molecular Cell Research, 1853(6), 1272–1283. https://doi.org/10.1016/j.bbamcr.2014.12.010

Kojic, M., Gawda, T., Gaik, M., Begg, A., Salerno-Kochan, A., Kurniawan, N. D., Jones, A., Drożdżyk, K., Kościelniak, A., Chramiec-Głąbik, A., Hediyeh-Zadeh, S., Kasherman, M., Shim, W. J., Sinniah, E., Genovesi, L. A., Abrahamsen, R. K., Fenger, C. D., Madsen, C. G., Cohen, J. S., … Wainwright, B. J. (2021). Elp2 mutations perturb the epitranscriptome and lead to a complex neurodevelopmental phenotype. *Nature Communications 2021 12:1, 12*(1), 1–18. https://doi.org/10.1038/s41467-021-22888-5

Krogan, N. J., & Greenblatt, J. F. (2001). Characterization of a Six-Subunit Holo-Elongator Complex Required for the Regulated Expression of a Group of Genes in Saccharomyces cerevisiae. *Molecular and Cellular Biology, 21*(23), 8203. https://doi.org/10.1128/MCB.21.23.8203-8212.2001

Krutyhołowa, R., Hammermeister, A., Zabel, R., Abdel-Fattah, W., Reinhardt-Tews, A., Helm, M., Stark, M. J. R., Breunig, K. D., Schaffrath, R., & Glatt, S. (2019). Kti12, a PSTK-like tRNA dependent ATPase essential for tRNA modification by Elongator. *Nucleic Acids Research, 47*(9), 4814. https://doi.org/10.1093/NAR/GKZ190

Ladang, A., Rapino, F., Heukamp, L. C., Tharun, L., Shostak, K., Hermand, D., Delaunay, S., Klevernic, I., Jiang, Z., Jacques, N., Jamart, D., Migeot, V., Florin, A., Göktuna, S., Malgrange, B., Sansom, O. J., Nguyen, L., Büttner, R., Close, P., & Chariot, A. (2015). Elp3 drives Wnt-dependent tumor initiation and regeneration in the intestine. *Journal of Experimental Medicine, 212*(12), 2057–2075. https://doi.org/10.1084/jem.20142288

Lampert, F., Peters, J.-M. M., Westermann, S., Stark, H., Huis in 't Veld, P. J., Petzold, G., Schulman, B. A., VanderLinden, R., Weissmann, F., Brown, N. G., Petzold, G., VanderLinden, R., Huis In't Veld, P. J., Brown, N. G., Lampert, F., Westermann, S., Stark, H., Schulman, B. A., & Peters, J.-M. M. (2016). biGBac enables rapid gene assembly for the expression of large multisubunit protein complexes. *Proceedings of the National Academy of Sciences of the United States of America, 113*(19), E2564–E2569. https://doi.org/10.1073/PNAS.1604935113/-/DCSUPPLEMENTAL

Lin, T.-Y., Abbassi, N. E. H., Zakrzewski, K., Chramiec-Głąbik, A., Jemioła-Rzemińska, M., Różycki, J., & Glatt, S. (2019). The Elongator subunit Elp3 is a non-canonical tRNA

acetyltransferase. *Nature Communications, 10*(1), 1–12. https://doi.org/10.1038/s41467-019-08579-2

Lin, T.-Y., Smigiel, R., Bozena Kuzniewska, |, Chmielewska, J. J., Kosińska, J., Mateusz Biela, |, Biela, A., Kościelniak, A., Dominika Dobosz, |, Laczmanska, I., Chramiec-Głąbik, A., Jeżowski, | Jakub, Nowak, J., Gos, M., Dziembowska, M., Ploski, R., & Glatt, S. (2022). *Destabilization of mutated human PUS3 protein causes intellectual disability.* https://doi.org/10.1002/humu.24471

Lin, T. Y., Mehta, R., & Glatt, S. (2021). Pseudouridines in RNAs: switching atoms means shifting paradigms. *FEBS Letters, 595*(18), 2310–2322. https://doi.org/10.1002/1873-3468.14188

Lin, Z., Zhao, W., Diao, W., Xie, X., Wang, Z., Zhang, J., Shen, Y., & Long, J. (2012). Crystal structure of elongator subcomplex Elp4-6. *Journal of Biological Chemistry, 287*(25), 21501–21508. https://doi.org/10.1074/jbc.M112.341560

Liu, F., Clark, W., Luo, G., Wang, X., Fu, Y., Wei, J., Wang, X., Hao, Z., Dai, Q., Zheng, G., Ma, H., Han, D., Evans, M., Klungland, A., Pan, T., & He, C. (2016). ALKBH1-Mediated tRNA Demethylation Regulates Translation. *Cell, 167*(3), 816-828.e16. https://doi.org/10.1016/J.CELL.2016.09.038

López-Estepa, M., Ardá, A., Savko, M., Round, A., Shepard, W. E., Bruix, M., Coll, M., Fernández, F. J., Jiménez-Barbero, J., & Vega, M. C. (2015). The Crystal Structure and Small-Angle X-Ray Analysis of CsdL/TcdA Reveal a New tRNA Binding Motif in the MoeB/E1 Superfamily. *PLOS ONE, 10*(4), e0118606. https://doi.org/10.1371/JOURNAL.PONE.0118606

Lu, J., Esberg, A., Huang, B., & Byström, A. S. (2008). Kluyveromyces lactis gamma-toxin, a ribonuclease that recognizes the anticodon stem loop of tRNA. *Nucleic Acids Research, 36*(4), 1072–1080. https://doi.org/10.1093/NAR/GKM1121

Lu, J., Huang, B. O., Esberg, A., Johansson, M. J. O., & Byström, A. S. (2005). The Kluyveromyces lactis gamma-toxin targets tRNA anticodons. *RNA (New York, N.Y.), 11*(11), 1648–1654. https://doi.org/10.1261/RNA.2172105

Madeira, F., Pearce, M., Tivey, A. R. N., Basutkar, P., Lee, J., Edbali, O., Madhusoodanan, N.,

Kolesnikov, A., & Lopez, R. (2022). Search and sequence analysis tools services from EMBL-EBI in 2022. *Nucleic Acids Research, 50*(W1), gkac240–gkac240. https://doi.org/10.1093/NAR/GKAC240

Mahlab, S., Tuller, T., & Linial, M. (2012). Conservation of the relative tRNA composition in healthy and cancerous tissues. *RNA, 18*(4), 640. https://doi.org/10.1261/RNA.030775.111

Marck, C., & Grosjean, H. (2002). tRNomics: analysis of tRNA genes from 50 genomes of Eukarya, Archaea, and Bacteria reveals anticodon-sparing strategies and domain-specific features. *RNA (New York, N.Y.), 8*(10), 1189–1232. https://doi.org/10.1017/S1355838202022021

Merrick, W. C., & Pavitt, G. D. (2018). Protein Synthesis Initiation in Eukaryotic Cells. *Cold Spring Harbor Perspectives in Biology, 10*(12). https://doi.org/10.1101/CSHPERSPECT.A033092

Moniruzzaman, M., LeCleir, G. R., Brown, C. M., Gobler, C. J., Bidle, K. D., Wilson, W. H., & Wilhelm, S. W. (2014). Genome of brown tide virus (AaV), the little giant of the Megaviridae, elucidates NCLDV genome expansion and host-virus coevolution. *Virology, 466–467*, 60–70. https://doi.org/10.1016/J.VIROL.2014.06.031

Morini, E., Gao, D., Montgomery, C. M., Salani, M., Mazzasette, C., Krussig, T. A., Swain, B., Dietrich, P., Narasimhan, J., Gabbeta, V., Dakka, A., Hedrick, J., Zhao, X., Weetall, M., Naryshkin, N. A., Wojtkiewicz, G. G., Ko, C.-P. P., Talkowski, M. E., Dragatsis, I., & Slaugenhaupt, S. A. (2019). *ELP1 Splicing Correction Reverses Proprioceptive Sensory Loss in Familial Dysautonomia. 104*(4), 638–650. https://doi.org/10.1016/J.AJHG.2019.02.009

Mörl, M., Betat, H., & Rammelt, C. (2010). tRNA nucleotidyltransferases: ancient catalysts with an unusual mechanism of polymerization. *Cellular and Molecular Life Sciences : CMLS, 67*(9), 1447–1463. https://doi.org/10.1007/S00018-010-0271-4

Nagayoshi, Y., Chujo, T., Hirata, S., Nakatsuka, H., Chen, C. W., Takakura, M., Miyauchi, K., Ikeuchi, Y., Carlyle, B. C., Kitchen, R. R., Suzuki, T., Katsuoka, F., Yamamoto, M., Goto, Y., Tanaka, M., Natsume, K., Nairn, A. C., Suzuki, T., Tomizawa, K., & Wei, F. Y. (2021). Loss of Ftsj1 perturbs codon-specific translation efficiency in the brain and is associated

with X-linked intellectual disability. *Science Advances*, *7*(13). https://doi.org/10.1126/SCIADV.ABF3072

Nau, F. (1976). The methylation of tRNA. *Biochimie*, *58*(6), 629–645. https://doi.org/10.1016/S0300-9084(76)80387-2

Nedialkova, D. D., & Leidel, S. A. (2015). Optimization of Codon Translation Rates via tRNA Modifications Maintains Proteome Integrity. *Cell*, *161*(7), 1606–1618. https://doi.org/10.1016/j.cell.2015.05.022

Ohira, T., Minowa, K., Sugiyama, K., Yamashita, S., Sakaguchi, Y., Miyauchi, K., Noguchi, R., Kaneko, A., Orita, I., Fukui, T., Tomita, K., & Suzuki, T. (2022). Reversible RNA phosphorylation stabilizes tRNA for cellular thermotolerance. *Nature 2022 605:7909*, *605*(7909), 372–379. https://doi.org/10.1038/s41586-022-04677-2

Omid-Shafaat, R., Moayeri, H., Rahimi, K., Menbari, M. N., Vahabzadeh, Z., Hakhamaneshi, M. S., Nouri, B., Ghaderi, B., & Abdi, M. (2021). Serum Circ-FAF1/Circ-ELP3: A novel potential biomarker for breast cancer diagnosis. *Journal of Clinical Laboratory Analysis*, *35*(11). https://doi.org/10.1002/JCLA.24008

Otero, G., Fellows, J., Yang, L., De Bizemont, T., Dirac, A. M. G., Gustafsson, C. M., Erdjument-Bromage, H., Tempst, P., & Svejstrup, J. Q. (1999). Elongator, a multisubunit component of a novel RNA polymerase II holoenzyme for transcriptional elongation. *Molecular Cell*, *3*(1), 109–118. https://doi.org/10.1016/S1097-2765(00)80179-3

Paraskevopoulou, C., Fairhurst, S. A., Lowe, D. J., Brick, P., & Onesti, S. (2006). The Elongator subunit Elp3 contains a Fe4S4 cluster and binds S-adenosylmethionine. *Molecular Microbiology*, *59*(3), 795–806. https://doi.org/10.1111/J.1365-2958.2005.04989.X

Pechmann, S., Willmund, F., & Frydman, J. (2013). The Ribosome as a Hub for Protein Quality Control. *Molecular Cell*, *49*(3), 411–421. https://doi.org/10.1016/J.MOLCEL.2013.01.020

Pedrioli, P. G. A., Leidel, S., & Hofmann, K. (2008). ' Protein Modifications : Beyond the Usual Suspects ' Review Series. *EMBO Reports*, *9*(12), 1196–1202. https://doi.org/10.1038/embor.209

Pettersen, E. F., Goddard, T. D., Huang, C. C., Couch, G. S., Greenblatt, D. M., Meng, E. C., & Ferrin, T. E. (2004). UCSF Chimera--a visualization system for exploratory research and analysis. *Journal of Computational Chemistry*, *25*(13), 1605–1612. https://doi.org/10.1002/JCC.20084

Planelles-Herrero, V. J., Bittleston, A., Seum, C., Gaitan, M. G., & Derivery, E. (2022). Elongator stabilizes microtubules to control central spindle asymmetry and polarized trafficking of cell fate determinants. *Nature Cell Biology 2022 24:11*, *24*(11), 1606–1616. https://doi.org/10.1038/s41556-022-01020-9

Przykorska, A., Adlouni, C. E., Keith, G., Szarkowski, J. W., & Dirheimer, G. (1992). Structural specificity of Rn nuclease I as probed on yeast tRNA(Phe) and tRNA(Asp). *Nucleic Acids Research*, *20*(4), 659. https://doi.org/10.1093/NAR/20.4.659

Pukkila, P. J. (2001). Molecular Biology: The Central Dogma. *ELS*, 1–5. https://doi.org/10.1038/npg.els.0000812

Punjani, A., Rubinstein, J. L., Fleet, D. J., & Brubaker, M. A. (2017). CryoSPARC: Algorithms for rapid unsupervised cryo-EM structure determination. *Nature Methods*, *14*(3), 290–296. https://doi.org/10.1038/nmeth.4169

Qiu, C., Bhat, V. D., Rajeev, S., Zhang, C., Lasley, A. E., Wine, R. N., Campbell, Z. T., & Tanaka Hall, T. M. (2019). A crystal structure of a collaborative rna regulatory complex reveals mechanisms to refine target specificity. *ELife*, *8*. https://doi.org/10.7554/ELIFE.48968

Rafels-Ybern, À., Torres, A. G., Grau-Bove, X., Ruiz-Trillo, I., & Ribas de Pouplana, L. (2018). Codon adaptation to tRNAs with Inosine modification at position 34 is widespread among Eukaryotes and present in two Bacterial phyla. *RNA Biology*, *15*(4–5), 500. https://doi.org/10.1080/15476286.2017.1358348

Rak, R., Polonsky, M., Eizenberg-Magar, I., Mo, Y., Sakaguchi, Y., Mizrahi, O., Nachshon, A., Reich-Zeliger, S., Stern-Ginossar, N., Dahan, O., Suzuki, T., Friedman, N., & Pilpel, Y. (2021). Dynamic changes in tRNA modifications and abundance during T cell activation. *Proceedings of the National Academy of Sciences of the United States of America*, *118*(42), e2106556118.

https://doi.org/10.1073/PNAS.2106556118/SUPPL_FILE/PNAS.2106556118.SD04.XLSX

Ranjan, N., & Leidel, S. A. (2019). The epitranscriptome in translation regulation: mRNA and tRNA modifications as the two sides of the same coin? *FEBS Letters*, *593*(13), 1483–1493. https://doi.org/10.1002/1873-3468.13491

Ranjan, N., & Rodnina, M. V. (2017). Thio-Modification of tRNA at the Wobble Position as Regulator of the Kinetics of Decoding and Translocation on the Ribosome. *Journal of the American Chemical Society*, *139*(16), 5857–5864. https://doi.org/10.1021/JACS.7B00727/ASSET/IMAGES/LARGE/JA-2017-00727B_0003.JPEG

Ranjan, N., & Rodnina, M. V. (2016). *tRNA wobble modifications and protein homeostasis*. https://doi.org/10.1080/21690731.2016.1143076

Rogalski, M., Karcher, D., & Bock, R. (2008). Superwobbling facilitates translation with reduced tRNA sets. *Nature Structural & Molecular Biology*, *15*(2), 192–198. https://doi.org/10.1038/NSMB.1370

Romano, G., Riccardi, F., Bussani, E., Vodret, S., Licastro, D., Ragone, I., Ronzitti, G., Morini, E., Slaugenhaupt, S. A., & Pagani, F. (2022). Rescue of a familial dysautonomia mouse model by AAV9-Exon-specific U1 snRNA. *The American Journal of Human Genetics*, *109*(8), 1534–1548. https://doi.org/10.1016/J.AJHG.2022.07.004

Ronowska, A., Szutowicz, A., Bielarczyk, H., Gul-Hinc, S., Klimaszewska-Łata, J., Dyś, A., Zyśk, M., & Jankowska-Kulawy, A. (2018). The regulatory effects of Acetyl-CoA distribution in the healthy and diseased brain. *Frontiers in Cellular Neuroscience*, *12*, 169. https://doi.org/10.3389/FNCEL.2018.00169/BIBTEX

Rubinstein, J. L., & Brubaker, M. A. (2015). Alignment of cryo-EM movies of individual particles by optimization of image translations. *Journal of Structural Biology*, *192*(2), 188–195. https://doi.org/10.1016/J.JSB.2015.08.007

Sayers, E. W., Bolton, E. E., Brister, J. R., Canese, K., Chan, J., Comeau, D. C., Connor, R., Funk, K., Kelly, C., Kim, S., Madej, T., Marchler-Bauer, A., Lanczycki, C., Lathrop, S., Lu, Z., Thibaud-Nissen, F., Murphy, T., Phan, L., Skripchenko, Y., … Sherry, S. T. (2022).

Database resources of the National Center for BiotechnologyInformation. *Nucleic Acids Research, 50*(D1), D20. https://doi.org/10.1093/NAR/GKAB1112

Schmeing, T. M., Moore, P. B., & Steitz, T. A. (2003). Structures of deacylated tRNA mimics bound to the E site of the large ribosomal subunit. *RNA, 9*(11), 1345. https://doi.org/10.1261/RNA.5120503

Schulz, F., Yutin, N., Ivanova, N. N., Ortega, D. R., Lee, T. K., Vierheilig, J., Daims, H., Horn, M., Wagner, M., Jensen, G. J., Kyrpides, N. C., Koonin, E. V., & Woyke, T. (2017). Giant viruses with an expanded complement of translation system components. *Science (New York, N.Y.), 356*(6333), 82–85. https://doi.org/10.1126/SCIENCE.AAL4657

Schwalm, E. L., Grove, T. L., Booker, S. J., & Boal, A. K. (2016). Crystallographic capture of a radical S-adenosylmethionine enzyme in the act of modifying tRNA. *Science, 352*(6283), 309–312. https://doi.org/10.1126/science.aad5367

Selvadurai, K., Wang, P., Seimetz, J., & Huang, R. H. (2014). Archaeal Elp3 catalyzes tRNA wobble uridine modification at C5 via a radical mechanism. *Nature Chemical Biology, 10*(10), 810–812. https://doi.org/10.1038/nchembio.1610

Séraphin, B., Kolaj-Robin, O., Desfosses, A., Hoffmann, N. A., Sachse, C., Dauden, M. I., Kosinski, J., Beck, M., Glatt, S., Breunig, K. D., Faux, C., Müller, C. W., Ori, A., Onuma, O. F., Kolaj-Robin, O., Desfosses, A., Ori, A., Faux, C., Hoffmann, N. A., … Müller, C. W. (2017). Architecture of the yeast Elongator complex. *EMBO Reports, 18*(2), 264–279. https://doi.org/10.15252/embr.201643353

Setiaputra, D. T., Cheng, D. T., Lu, S., Hansen, J. M., Dalwadi, U., Lam, C. H., To, J. L., Dong, M., & Yip, C. K. (2017). *Molecular architecture of the yeast Elongator complex reveals an unexpected asymmetric subunit arrangement. 18*(2). /pmc/articles/PMC5286391/

Shi, H., & Moore, P. B. (2000). The crystal structure of yeast phenylalanine tRNA at 1.93 A resolution: a classic structure revisited. *RNA (New York, N.Y.), 6*(8), 1091–1105. https://doi.org/10.1017/S1355838200000364

Shi, R., Villarroya, M., Ruiz-Partida, R., Li, Y., Proteau, A., Prado, S., Moukadiri, I., Benítez-Páez, A., Lomas, R., Wagner, J., Matte, A., Velázquez-Campoy, A., Armengod, M. E., & Cygler, M. (2009). Structure-Function Analysis of Escherichia coli MnmG (GidA), a

Highly Conserved tRNA-Modifying Enzyme. *Journal of Bacteriology*, *191*(24), 7614. https://doi.org/10.1128/JB.00650-09

Slaugenhaupt, S. A., Blumenfeld, A., Gill, S. P., Leyne, M., Mull, J., Cuajungco, M. P., Liebert, C. B., Chadwick, B., Idelson, M., Reznik, L., Robbins, C. M., Makalowska, I., Brownstein, M. J., Slaugenhaupt, S. A., Scheidereit, C., Maayan, C., Axelrod, F. B., & Gusella, J. F. (2001). Tissue-specific expression of a splicing mutation in the IKBKAP gene causes familial dysautonomia. *American Journal of Human Genetics*, *68*(3), 598–605. https://doi.org/10.1086/318810

Sokołowski, M., Klassen, R., Bruch, A., Schaffrath, R., & Glatt, S. (2018). Cooperativity between different tRNA modifications and their modification pathways. *Biochimica et Biophysica Acta (BBA) - Gene Regulatory Mechanisms*, *1861*(4), 409–418. https://doi.org/10.1016/J.BBAGRM.2017.12.003

Sprinzl, M., & Cramer, F. (1979). The -C-C-A End of tRNA and Its Role in Protein Biosynthesis. *Progress in Nucleic Acid Research and Molecular Biology*, *22*(C), 1–69. https://doi.org/10.1016/S0079-6603(08)60798-9

Sprinzl, M., Horn, C., Brown, M., Loudovltch, A., & Steinberg, S. (1998). Compilation of tRNA sequences and sequences of tRNA genes. *Nucleic Acids Research*, *26*(1), 148–153. https://doi.org/10.1093/NAR/26.1.148

Studte, P., Zink, S., Jablonowski, D., Bär, C., Von Der Haar, T., Tuite, M. F., & Schaffrath, R. (2008). tRNA and protein methylase complexes mediate zymocin toxicity in yeast. *Molecular Microbiology*, *69*(5), 1266–1277. https://doi.org/10.1111/J.1365-2958.2008.06358.X

Suzuki, Takeo, Yashiro, Y., Kikuchi, I., Ishigami, Y., Saito, H., Matsuzawa, I., Okada, S., Mito, M., Iwasaki, S., Ma, D., Zhao, X., Asano, K., Lin, H., Kirino, Y., Sakaguchi, Y., & Suzuki, T. (2020). Complete chemical structures of human mitochondrial tRNAs. *Nature Communications*, *11*(1). https://doi.org/10.1038/S41467-020-18068-6

Suzuki, Tsutomu. (2021). The expanding world of tRNA modifications and their disease relevance. *Nature Reviews Molecular Cell Biology 2021 22:6*, *22*(6), 375–392. https://doi.org/10.1038/s41580-021-00342-0

Takagi, Y., Kuwabara, N., Dang, T. T., Furukawa, K., & Kiong Ho, C. (2020). Crystal structures of the RNA triphosphatase from Trypanosoma cruzi provide insights into how it recognizes the 59-end of the RNA substrate. *Journal of Biological Chemistry, 295*(27), 9076–9086. https://doi.org/10.1074/jbc.ra119.011811

Taniguchi, T., Miyauchi, K., Sakaguchi, Y., Yamashita, S., Soma, A., Tomita, K., & Suzuki, T. (2018). Acetate-dependent tRNA acetylation required for decoding fidelity in protein synthesis. *Nature Chemical Biology, 14*(11), 1010–1020. https://doi.org/10.1038/S41589-018-0119-Z

Tavakoli, S., Nabizadeh, M., Makhamreh, A., Gamper, H., McCormick, C. A., Rezapour, N. K., Hou, Y. M., Wanunu, M., & Rouhanifard, S. H. (2023). Semi-quantitative detection of pseudouridine modifications and type I/II hypermodifications in human mRNAs using direct long-read sequencing. *Nature Communications 2023 14:1, 14*(1), 1–12. https://doi.org/10.1038/s41467-023-35858-w

Tugarinov, V., Muhandiram, R., Ayed, A., & Kay, L. E. (2002). Four-dimensional NMR spectroscopy of a 723-residue protein: Chemical shift assignments and secondary structure of malate synthase G. *Journal of the American Chemical Society, 124*(34), 10025–10035. https://doi.org/10.1021/JA0205636/ASSET/IMAGES/LARGE/JA0205636F00008.JPEG

Ueki, Y., Shchepetkina, V., & Lefcort, F. (2018). Retina-specific loss of Ikbkap/Elp1 causes mitochondrial dysfunction that leads to selective retinal ganglion cell degeneration in a mouse model of familial dysautonomia. *Disease Models & Mechanisms, 11*(7). https://doi.org/10.1242/DMM.033746

Van Den Born, E., Vågbø, C. B., Songe-Møller, L., Leihne, V., Lien, G. F., Leszczynska, G., Malkiewicz, A., Krokan, H. E., Kirpekar, F., Klungland, A., & Falnes, P. Ø. (2011). *ALKBH8-mediated formation of a novel diastereomeric pair of wobble nucleosides in mammalian tRNA.* https://doi.org/10.1038/ncomms1173

Varadi, M., Anyango, S., Deshpande, M., Nair, S., Natassia, C., Yordanova, G., Yuan, D., Stroe, O., Wood, G., Laydon, A., Zídek, A., Green, T., Tunyasuvunakool, K., Petersen, S., Jumper, J., Clancy, E., Green, R., Vora, A., Lutfi, M., … Velankar, S. (2022). AlphaFold Protein Structure Database: massively expanding the structural coverage of

protein-sequence space with high-accuracy models. *Nucleic Acids Research*, *50*(D1), D439–D444. https://doi.org/10.1093/NAR/GKAB1061

Villahermosa, D., & Fleck, O. (2017). Elp3 and Dph3 of Schizosaccharomyces pombe mediate cellular stress responses through tRNALys. *Scientific Reports*, *7*(1). https://doi.org/10.1038/s41598-017-07647-1

Wang, X., & He, C. (2014). Dynamic RNA modifications in posttranscriptional regulation. *Molecular Cell*, *56*(1), 5–12. https://doi.org/10.1016/J.MOLCEL.2014.09.001

Waterhouse, A., Bertoni, M., Bienert, S., Studer, G., Tauriello, G., Gumienny, R., Heer, F. T., De Beer, T. A. P., Rempfer, C., Bordoli, L., Lepore, R., & Schwede, T. (2018). SWISS-MODEL: homology modelling of protein structures and complexes. *Nucleic Acids Research*, *46*(W1), W296–W303. https://doi.org/10.1093/NAR/GKY427

Wruck, F., Katranidis, A., Nierhaus, K. H., Büldt, G., & Hegner, M. (2017). Translation and folding of single proteins in real time. *Proceedings of the National Academy of Sciences of the United States of America*, *114*(22), E4399–E4407. https://doi.org/10.1073/PNAS.1617873114/SUPPL_FILE/PNAS.1617873114.SAPP.PDF

Xu, H., Lin, Z., Li, F., Diao, W., Dong, C., Zhou, H., Xie, X., Wang, Z., Shen, Y., & Long, J. (2015). Dimerization of elongator protein 1 is essential for Elongator complex assembly. *Proceedings of the National Academy of Sciences of the United States of America*, *112*(34), 10697–10702. https://doi.org/10.1073/PNAS.1502597112

Xu, Y., Zhou, W., Ji, Y., Shen, J., Zhu, X., Yu, H., Guo, J., Pang, Z., & Wei, W. (2018). Elongator promotes the migration and invasion of hepatocellular carcinoma cell by the phosphorylation of AKT. *International Journal of Biological Sciences*, *14*(5), 518–530. https://doi.org/10.7150/ijbs.23511

Ye, S., & Lehmann, J. (2022). Genetic code degeneracy is established by the decoding center of the ribosome. *Nucleic Acids Research*, *50*(7), 4113–4126. https://doi.org/10.1093/nar/gkac171

Yu, F., Tanaka, Y., Yamashita, K., Suzuki, T. T., Nakamura, A., Hirano, N., Suzuki, T. T., Yao, M., & Tanaka, I. (2011). Molecular basis of dihydrouridine formation on tRNA.

Proceedings of the National Academy of Sciences of the United States of America, 108(49), 19593–19598. https://pubmed.ncbi.nlm.nih.gov/22123979/

Zheng, S. Q., Palovcak, E., Armache, J.-P., Cheng, Y., & Agard, D. A. (2016). Anisotropic Correction of Beam-induced Motion for Improved Single-particle Electron Cryo-microscopy. *BioRxiv*, 061960. https://doi.org/10.1101/061960

Zivanov, J., Nakane, T., & Scheres, S. H. W. (2020). Estimation of high-order aberrations and anisotropic magnification from cryo-EM data sets in RELION-3.1. *Urn:Issn:2052-2525, 7*(2), 253–267. https://doi.org/10.1107/S2052252520000081

List of figures

Appendix

Table 1. CryoEM data collection and processing values.

	*Hs*ELP123 tGln_DCA _Form1	*Hs*ELP123 tGln_DCA _Form1p2	*Hs*ELP123 tGln_DCA _Form2	*Hs*ELP123 tGln_ECA _ Form1p2	*Hs*ELP123 tGln_ECA _ Form1
Data collection and processing					
Magnification	105 000x	105 000x	105 000x	105 000x	105 000x
Voltage (keV)	300	300	300	300	300
Electron exposure (e-/ Å^2)	40	40	40	40	40
Defocus range	-0.9 to -2.1	-0.9 to -2.1	-0.9 to -2.1	-0.9 to -2.1	-0.9 to -2.1
Pixel size (Å)	0.86	0.86	0.86	0.85	0.85
Symmetry imposed	C1	C1	C1	C1	C1
Micrograph number	20720	20720	20720	3192	3192
Initial particle images (no.)	1 803 276	1 803 276	1 803 276	409 189	409189
Initial particle images (no.)	198 709	51574	170728	33 801	17 868
Map resolution (Å)	4.23	3.8	4.29	3.35	3.78
FSC threshold	0.143	0.143	0.143	0.143	0.143
Map resolution range (Å)	4.1 to 7.4	3.8 to 6.2	4.3 to 7.6	3.4 to 8.9	3.6 to 9.6

A

```
1
MRQKRKGDLS   PAELMMLTIG   DVIKQLIEAH   EQGKDIDLNK   VKTKTAAKYG   LSAQPRLVDI   IAAVPPQYRK   70
71
VLMPKLKAKP   IRTASGIAVV   AVMCKPHRCP   HISFTGNICV   YCPGGPDSDF   EYSTQSYTGY   EPTSMRAIRA   140
141
RYDPFLQTRH   RIEQLKQLGH   SVDKVEFIVM   GGTFMALPEE   YRDYFIRNLH   DALSGHTSNN   IYEAVKYSER   210
211
SLTKCIGITI   ETRPDYCMKR   HLSDMLTYGC   TRLEIGVQSV   YEDVARDTNR   GHTVKAVCES   FHLAKDSGFK   280
281
VVAHMMPDLP   NVGLERDIEQ   FTEFFENPAF   RPDGLKLYPT   LVIRGTGLYE   LWKSGRYKSY   SPSDLVELVA   350
351
RILALVPPWT   RVYRVQRDIP   MPLVSSGVEH   GNLRELALAR   MKDLGIQCRD   VRTREVGIQE   IHHKVRPYQV   420
421
ELVRRDYVAN   GGWETFLSYE   DPDQDILIGL   LRLRKCSEET   FRFELGGGVS   IVRELHVYGS   VVPVSSRDPT   490
491
KFQHQGFGML   LMEEAERIAR   EEHGSGKIAV   ISGVGTRNYY   RKIGYRLQGP   YMVKMLK      547
```

B

HsElp3

Peptide	Modified residue	IonScore	# PSMs	ΔM [ppm]
1	K6, M15, M16	84	5	0.06
1	K6	41	6	0.85
1	K6, M16	24	14	-0.99
2	K48	62	1	0.90
3	K70, M73	18	1	-0.22
6	C268, K275	26	1	2.50
7	K280, M285, M286	49	1	-2.05
8	K316	19	1	-0.56
9	K333	61	1	-0.45
10	K338	48	1	-0.82
12	K455, C456	32	1	-0.36
13	K491, M499, M502	31	1	-2.52

HsElp3$_{K280A}$

Peptide	Modified residue	IonScore	# PSMs	ΔM [ppm]
1	K6	68	27	0.68
1	K6, M15	50	85	-2.34
1	K6, M16	28	33	0.29
1	K6, M15, M16	67	53	-0.20
3	K70, M73	19	6	0.37
4	K77	14	1	-0.98
5	K164, M175	25	2	-6.41
5	K164, M170, M175	46	5	-0.24
6	C268, K275	14	1	-1.14
8	K316	38	1	-3.78
10	K338	56	4	1.01
11	M391, K392, C398	28	11	-2.16
11	K392, C398	14	1	0.68
12	K455, C456	52	5	0.08
13	K491, M499, M502	53	2	-3.49
14	K532	20	1	-0.18

HsElp3$_{Y363A}$

Peptide	Modified residue	IonScore	# PSMs	ΔM [ppm]
1	K6	67	21	0.29
1	K6, M15	42	24	-2.45
1	K6, M16	44	95	0.95
1	K6, M15, M16	63	30	-0.35
3	K70, M73	19	3	-0.07
4	K77	15	1	-0.63
5	K156	22	1	0.56
5	K164, M175	22	2	2.74
5	K164, M170, M175	46	6	1.43
7	K280	30	1	0.11
7	K280, M285, M286	42	3	-0.03
8	K316	27	2	-1.15
8	K338	55	3	0.13
11	M391, K392, C398	22	7	0.63
13	K491, M499, M502	24	1	6.57

Appendix 2. **Summary of Mass spectrometry data**. A. HsElp3 protein sequence, in green highlights are the peptides analyzed by Mass Spec, in Magenta are the modified residues (Lysines are acetylated, Methionines are oxidated, and Cysteines are Carbamidomethylated). Above the modified residues are the markers to indicate in which condition they were found, pink circle is HsElp3 WT, yellow star is HsElp3$_{K280A,}$ and green diamond is HsElp3$_{Y363A}$. B. Tables of scores from the Mass spectrometry readings. Ion score refers to the confidence level of the data (the higher, the better), PSMs refers to the number of reads performed on each peptide, ΔM is the technical error registered, best values are <|3|, experiments performed at least three times.

List of Scientific achievements

Participation in conferences and workshops

1. Oral presentation: Golden seminar MCB: Molecular insights into acetyl-CoA hydrolysis of human elongator, Krakow 2022.

2. Flash talk: EMBO PhD YIP course. *The Elongator complex puts the accent in our lives.* Online workshop **Nour-el-Hana Abbassi** 2021

3. Presentation: EMBO PhD YIP course. *Towards understanding the Human Elongator.* **Nour-el-Hana Abbassi**. Online workshop 2021

4. Oral Presentation: Golden seminar MCB: Biochemical and structural study of tRNA binding capability of Elp3. Online presentation. 2020

5. Oral presentation: Scientific retreat. Molecular insight of Mouse 123 complex. Ziwiec, 2019.

6. Poster: EMBO Couse. The Elongator subunit Elp3 is a noncanonical tRNA acetyltransferase. Ting-yu Lin, Nour-el-Hana Abbassi, Sebastian Glatt. Oxford 2019

7. Presentation: EMBO Couse High-throughput protein production and crystallization. *Towards understanding the Human Elongator.* **Nour-el-Hana Abbassi**. Oxford, 2019

8. Poster: KISS meeting, The noncanonical lysine acetyl transferase activity of Elp3. Krakow 2018

9. Flash-talk: MCB Summer school. *Towards understanding the Human Elongator.* **Nour-el-Hana Abbassi**. Zakopane, 2019

10. Oral Presentation: Golden seminar MCB: Biochemical and structural study of tRNA binding capability of Elp3. 2018

11. Oral Presentation: Lab retreat, tRNA binding activity and selectivity of Elp3, **Nour-el-Hana Abbassi,** Sandomierz 2018.

12. Poster: MCB Summer school, The noncanonical lysine acetyl transferase activity of Elp3. Zakopane 2018

Scientific broadcast

- Elected PhD representative for the MCB board in 2021.
- Participated in the 2020, 2021 and 2022 editions of the MetaSUB global City Sampling Day.

- Part of the BioS selection committee for applications for scientific conferences for students and employees and for six-months master's students projects lead by two or three students. April – November 2020.
- Participated in the French 3-minute thesis contest. The first online edition. 2020
- Organization of a two-day workshop for PhD students' rotation in MCB in Molecular Biology November 2019.
- Organization of a protein workshop for the Science night October 2019
- Co-organization of a three-days PhD school for SMM (School of Molecular Medicine) with two days of conferences and a Molecular replacement workshop. November 2018
- Co-organization of a protein workshop for the science night October 2018

Master students
- Two-years internship of a second master's student. I involved this second student in the production of tRNA binding mutants in the human Elongator sub-complex 123, its expression and biochemical activity. (October 2019- June 2021)
- A two-months internship of a master's student, I taught him the bases of Molecular Biology and his project in extracting the genes of Elongator proteins 456 from the cDNA of HEK cells. I was also involved in the correction of his Masters' thesis (January – March 2019)

Acknowledgements